AN EXPERIMENTAL STUDY OF ELECTRON FLUXES FROM 50 KEV TO 4 MEV IN THE INNER RADIATION BELT*

by

Karl A. Pfitzer

COSMIC RAY GROUP

School of Physics and Astronomy

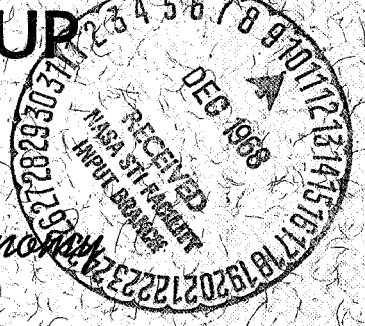

UNIVERSITY OF MINNESOTA

TABLE OF CONTENTS

LIST OF TABLES

LIST OF FIGURES

ABSTRACT

A five channel magnetic electron spectrometer which is capable of accurately measuring the electron spectrum from 50 Kev to 4 Mev is described in this thesis. The five energy channels of the spectrometer are: 50-120 Kev, 120-290 Kev, 290-690 Kev, 690-1700 Kev and 1700-4000 Kev. The spectrometer consists of two separate detectors operating together to provide double energy selection. The first of these is an electromagnet with a collimating slit having a geometry factor of 8.64×10^{-3} sterad-cm^2. The second detector consists of a heavily shielded scintillation crystal and photomultiplier tube. Since a magnetic field is necessary to bend the electrons into the scintillation detector, the background due to penetrating particles and bremsstrahlung can be measured by going through a complete analysis cycle with the magnetic field turned off. The electron spectrometers were flown on the Orbiting Geophysical Observatories (OGO) I and III.

The two spectrometers which have been cross calibrated in space and shown to agree to within 10% observe the continuing decay of the electrons injected into the inner zone by the nuclear explosion, Starfish, on July 9, 1962. The spectrometers observe a factor of ten decrease in the electron flux over a period of two years from September 1964 to August 1966 in the inner zone below L = 1.8 for electrons

of E > 290 Kev. This decrease is attributed to the decaying Starfish electrons by comparing the decrease and flux levels to experiments which have measured the Starfish decay since shortly after the detonation. The 50-120 Kev electrons, however, are observed to increase slightly during this two year period and the 120-290 Kev electrons are observed to have a two year decay rate intermediate between the 50-120 Kev electrons and the 290-690 Kev electrons.

The diffusion-like injection of electrons of energy up to 690 Kev deep into the inner zone to L = 1.3, creating a new and stable inner zone of natural origin, was observed following the magnetic storm associated with the September 2, 1966 solar flare. No increase in this region below L = 2.0 was observed for electrons of energy greater than 690 Kev. Within one day of the onset of the event a wave of electrons was observed to penetrate to L = 2.0; following this initial wave there is a slow diffusion inward, such that the maximum increase at L = 1.4 (e.g. a factor of 3 increase for 290-690 Kev electrons) is reached 30 days after the onset of the event. The increase immediately after the arrival of the wave for L > 2.0 is very large (e.g. more than an order of magnitude for 290-690 Kev electrons at L = 2.2); this large increase, however, begins an immediate rapid exponential decay (τ = 13 days at L = 2.2 for 290-690 Kev electrons) such that by mid-October the fluxes decayed to prestorm levels. For L < 2.0

on the other hand, no rapid decay is observed and the "new" inner zone resumes the slow decay ($\tau \approx$ 300-400 days) observed during the two years prior to the September 2, 1966 event.

Because of the very slow decay following the injection, the electrons injected by the September 2, 1966 event will decay to the prestorm levels for $L < 2.0$ in about one year. Therefore, only one or two events of this magnitude would suffice to supply the inner zone electrons ($50 < E < 690$ Kev) below $L = 2.0$.

The equatorial pitch angle distributions for all L values in the inner zone during the entire two year period including the injection event were found to be flat near $\alpha_o = 90°$ and drop off rapidly near the loss cone.

I. Introduction

A. History of the Radiation Belts

This thesis is an experimental study of the origin of the trapped electrons in the earth's radiation belts. Prior to the advent of earth satellites, no measurement of the electron flux was possible above several hundred kilometers. The rocket measurements which had been made did not indicate the existence of trapped energetic electrons. However, the ability of the earth's magnetic field to trap electrons in a mirroring geometry had been discussed by Cristofilos in a classified paper in 1957 which was first published in 1959 (Cristofilos, 1959). Cristofilos had suggested the exploding of a nuclear device in space to create a trapped belt of electrons. The basis for this suggestion was the description of the motion of particles in the earth's dipole field by Alfven and Stoermer.

Van Allen's measurements (Van Allen, 1958) on Explorers I and III gave the first indications of a large flux of geomagnetically trapped particles. After the initial discovery of the radiation belts numerous other satellites were launched to explore the radiation trapped in the earth's magnetic field. The early instruments contained detectors which were not capable of determining the type of particles or the energies of the particles trapped in the magnetic field.

Data from Explorer IV (Van Allen, McIlwain and Ludwig, 1959) showed that there existed two distinct maximums in the counting rates of the trapped particle fluxes. This led to the division of the radiation belts into the inner belt and the outer belt. The first particles to be identified and measured were the protons. Emulsions flown into the inner belt on an Atlas rocket in 1959 (Freden and White, 1959) detected these protons and measured their energies. The proton fluxes in the inner zone as well as in the outer zone were soon measured accurately. The proton fluxes were found to be relatively stable in time.

A sounding rocket carrying a permanent magnet spectrometer first positively identified the particles in the outer zone as electrons (Cladis et al., 1961). Detectors on Explorer VI showed that the fluxes in the outer zone were very variable and changed by several orders of magnitude especially during periods of solar activity (Arnoldy, Hoffman and Winckler, 1960). Most of these early measurements of electrons were made by shielded scintillation crystals, shielded geiger counters and ion chambers whose primary response to the electrons in the outer zone was thought to be via the intermediate bremsstrahlung process. This gave rise to the interpretation that the flux of electrons above 50 Kev is 10^{10}-10^{11} electrons/cm^2 sec (Van Allen, 1959). Later measurements on Explorer XII and Injun I (O'Brien et al., 1962) using end window geiger counters and a fixed field

magnetic analyzer showed that the flux above 50 Kev was of the order of 10^7-10^8 electrons-cm^{-2}-sec^{-1} and that the earlier detectors were responding directly to penetrating electrons having energy greater than 1 Mev.

In 1961 McIlwain (1961) introduced the B and L coordinate system which reduces the number of variables necessary to describe a measurement. L defines a magnetic shell on which a particle moves in terms of earth radii where the shell crosses the magnetic equator. B is the strength of the magnetic field on the L shell at the point where the measurement is made. This coordinate system greatly simplified the organization of the data.

In the inner zone, the most difficult region for an accurate electron measurement because of the large high energy proton flux, high altitude nuclear explosions modified the electron environment before an acceptable measurement of the flux could be obtained. The nuclear explosion, "Starfish", of July 9, 1962, injected a large number of electrons into the heart of the inner zone and the electron environment was altered for many years because of the extremely long life-times in this region. In a review paper O'Brien (1962) summarizes all of the information obtained prior to Starfish and obtains

$$J(E \geq 40 \text{ Kev}) \approx 10^8 \text{ electrons-cm}^{-2}\text{-sec}^{-1}\text{-sterad}^{-1}$$

$$J(E \geq 600 \text{ Kev}) \approx 10^6 \text{ electrons-cm}^{-2}\text{-sec}^{-1}\text{-sterad}^{-1}$$

with an uncertainty of at least a factor of three in each case.

Following the nuclear explosion Starfish a large number of measurements were made of the fission decay products. The early history following Starfish was studied on satellites Injun I, Telstar, TRAAC and Ariel I. A fairly good composite picture of the artificial belt emerged from these measurements (Hess, 1963). The maximum electron flux injected by the explosion was about 10^9 electrons-cm^{-2}-sec^{-1} at a radial distance of about $L = 1.3$. The Starfish explosion provided a measure of the electron decay times as a function of position and energy. The decay times were found to be about 300-400 days being more rapid for lower energies and more rapid for lower altitudes. After the first year following the explosion, the flux of electrons in the inner zone decayed again to lower levels and the difficulty in separating proton and electron fluxes returned. The polar satellite 1963-38C continued to measure the decay of Starfish electrons up to the present time (Beall et al., 1967). 1963-38C is, however, a polar satellite and measures fluxes only at low altitudes and does not measure the flux in the heart of the inner zone. Before the present work no post-Starfish measurements of natural electrons were available in the inner zone. The measurement of the existence of a natural electron flux is quite important in determining the validity of a number of injection theories.

B. Statement of the Problem

The major work of this thesis is the design and construction of an electron spectrometer which is capable of measuring electron fluxes throughout the entire radiation belt without background contamination due to penetrating protons and bremsstrahlung. When the experiment was first proposed in 1961 the measurements of electron spectra in all parts of the radiation belts were uncertain by at least a factor of 100. Between the time when the experiment design was started and the first data was available in late 1964 a large volume of data was gathered in the outer zone; however, no new information became available for the natural electron fluxes in the inner zone because of a large artificial electron background and because of a continuing lack of detectors capable of separating the electron flux from the large proton flux. The problems that the electron spectrometer measurements will attempt to answer in this thesis are:

1. The accurate measurement of electron spectra from 50 Kev to 4 Mev throughout the inner zone.
2. The pitch angle and L dependence of the electron fluxes.
3. The time dependence of the electron fluxes during magnetically quiet and magnetically disturbed times.

These measurements of the equilibrium conditions are necessary in order to formulate a possible injection and loss theory.

4. The measurement of the residual flux of artificially injected electrons.

The knowledge of the residual Starfish background is of prime importance in determining the natural equilibrium electron flux.

5. Evidence of injection of natural electrons into the inner zone following magnetic disturbances which are known to alter the flux of electrons in the outer zone.

The only observed source of electrons in the inner zone to date has been the nuclear explosion Starfish.

6. The importance of various suggested injection processes as they apply to the inner zone using these more complete inner zone measurements.

The suggested sources of the electrons in the inner zone are:

a. Direct injection of solar electrons.

b. Neutron albedo decay.

c. Photoelectric processes which liberate electrons from the atmosphere.

d. Diffusion inward of outer zone electrons.

e. Local acceleration of electrons from the ambient plasma.

The remainder of this thesis will concern itself with the development of an electron spectrometer which is able to provide a complete and accurate measurement of the electron fluxes in the inner zone.

C. Instrumentation

The accurate measurement of electron spectra throughout the trapping region and, in particular, in the inner zone is

indeed a very difficult task. The main problems as discussed in the previous section are large variable fluxes, large changes in spectra and difficulties in separating the electrons from the penetrating particle and bremsstrahlung background. The primary difficulties with each of the three types of electron detectors that have been used in the past will be listed below:

Type 1. Geiger tubes using various thicknesses of shielding measure the integral spectrum only and can only obtain information on electron fluxes where the flux of penetrating protons is small compared to the electron flux. The efficiency can be very dependent on the spectra. If the spectra are very steep some of the counts may be due to bremsstrahlung by non-penetrating electrons. These detectors cannot measure the contamination due to the various backgrounds.

Type 2. Scintillation crystal spectrometers using various thicknesses of shielding also depend on the absence of a penetrating proton flux from obscuring the electron measurement. They may also be sensitive to bremsstrahlung background and are not capable of measuring their background contamination.

Type 3. Permanent magnet analyzers have a limited energy range (factor of 2 to 5) and have in the past suffered from bremsstrahlung and penetrating proton background due to small entrance apertures and inadequate shielding. They are, however, capable of measuring their own background contamination.

The swept field magnetic electron spectrometer with which this thesis concerns itself is an instrument which can measure accurately the electron flux throughout the radiation belt without the danger of background contamination. By using an electromagnet instead of a permanent magnet, we can select electrons from a few Kev to many Mev. The lower limit is determined by the detectors available for counting the selected electrons. This lower limit is about 50 Kev for the detectors that were available and useable at the time the instrument was designed. The upper limit was determined by the power and weight restriction of satellite operation. This limit is about 4 Mev for a magnet having a peak field of 4000 gauss and a 3 cm turning radius. A larger turning radius is impossible because of the weight constraint and a larger field is impossible both because of weight and power constraints. Two such electron spectrometers were successfully orbited on the Orbiting Geophysical Observatories (OGO) I and III. The primary limitation of the electron spectrometers flown on OGO-I and III is a relatively high flux threshold due to a low duty cycle of the analyzing magnet. The high flux threshold caused some difficulties in measuring low fluxes in some regions of the radiation belt. The following is a brief description of the two instruments flown on OGO-I and III.

The electron spectrometer is designed to measure electrons in five energy channels. These channels are:

Channel # I	50-120 Kev
Channel # II	120-290 Kev
Channel #III	290-690 Kev
Channel # IV	690-1700 Kev
Channel # V	1700-4000 Kev

The spectrometer consists of two separate detectors operating together to provide a double selection on the electron energies. (See Figure I-1). The first of these is an electromagnet with a collimating slit. The collimating slit has a geometry factor of 8.64×10^{-3} sterad-cm^2 which defines a beam of particles entering the magnet. The magnet then bends the electrons through 65 degrees and selects a certain narrow range of electron energies which pass through the exit aperture of the magnet into the second detector. The second detector consists of a heavily shielded plastic scintillation crystal and a photomultiplier tube. This detector gives an output proportional to the total energy of an electron which is bent through the magnet.

The field in the electromagnet sweeps continuously from a residual of 20 gauss to a maximum of 4000 gauss. The edges of the discriminator for the scintillator pulse height analyzer are stepped along such that when the magnet selects particles of energy E_i which fall into channel i, the pulse height analyzer accepts only pulses corresponding

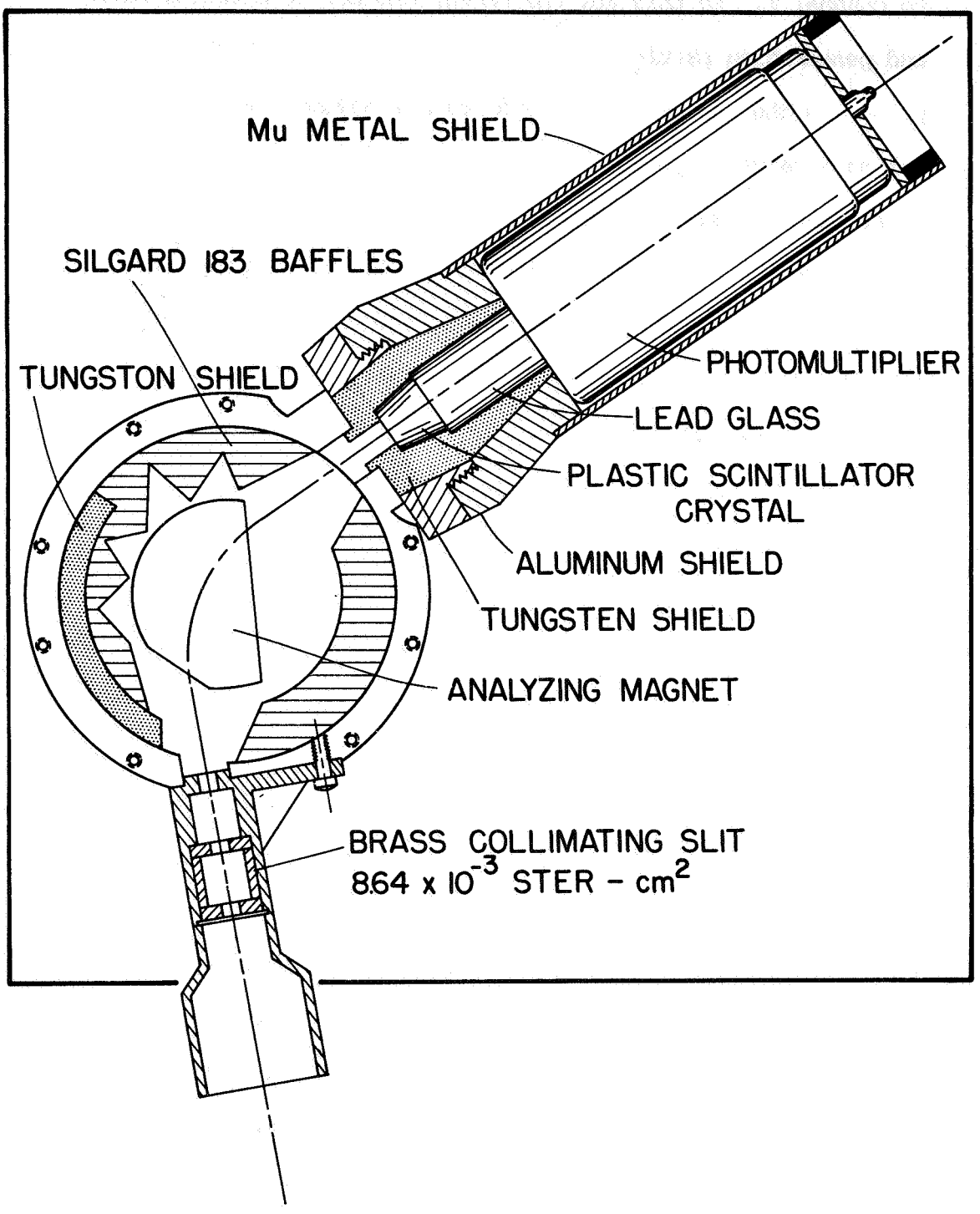
Mu METAL SHIELD
SILGARD 183 BAFFLES
TUNGSTON SHIELD
PHOTOMULTIPLIER
LEAD GLASS
PLASTIC SCINTILLATOR CRYSTAL
ALUMINUM SHIELD
TUNGSTEN SHIELD
ANALYZING MAGNET
BRASS COLLIMATING SLIT
8.64 x 10^-3 STER - cm^2

Figure I-1

to channel i. In this way the background due to bremsstrahlung and penetrating particles is reduced because only background pulses in the narrow energy band being analyzed are counted. During alternate cycles the magnet is turned off, but the pulse height analyzer steps through the same sequence as with magnet on and measures the background. The system thus samples 5 spectral intervals and 5 background values every 2.7 seconds. The rate in each energy channel is corrected by subtracting the background rate measured in that channel. Because of the limited power available the duty cycle of the magnet is very low, so the magnet is operated for less than 0.1 seconds every 2.7 seconds.

The first model of the spectrometer was designed for flight on an Argo D-8 rocket launched from the Pacific Missile Range in order to measure the electron flux in the Starfish radiation belt. One of the primary missions of the flight was to test the design of the satellite spectrometer. The rocket spectrometer had a much higher duty cycle because of the larger amount of power available. It had an entrance slit of 8×10^{-4} sterad-cm^2, about 8 gm of lead shielding and a plastic crystal almost twice the size of the satellite version. The rocket was successfully launched on February 12, 1963. The results were discouraging since all channels suffered from a large background. The flight into the Starfish belt provided a severe test because the spectrum was very hard and therefore the bremsstrahlung

background was especially large and, furthermore, the proton background is also largest in this region. Had the spectrometer given good results in this region, it would have given good results in any region of space. To improve the design, the entrance aperture was opened a factor of 10, the plastic crystal decreased in size by a factor of 2 and the shielding of the detector doubled. This new design proved extremely succesful in its rejection of the penetrating proton and bremsstrahlung background, even under the hardest spectra encountered.

A third model of the spectrometer was built to provide a follow-up on the satellite measurement and also to provide a backup in case of a failure of the satellite experiments. This model contained a detector identical to the satellite model; however, it had a 100% duty cycle. Instead of charging a capacitor as in the first two models and then discharging it through the magnet, the magnet was stepped using DC currents. Furthermore, information from all five energy channels was telemetered to the ground at all times. It was launched from Wallops Island to measure the radiation in the "slot" between the two belts where the count rates of the satellite spectrometers are often below detectable levels. The instrument functioned perfectly; however, the shroud failed to separate from the payload and the entrance aperture was blocked by almost one inch of oblative material and therefore no useful information was obtained.

The remainder of this thesis will concern itself with two identical spectrometers launched on the OGO-I and OGO-III satellites. Many months of useful data have been obtained from both of the satellites and both instruments are currently functioning and still providing useful data. The description of the construction and calibration procedures in the next two chapters are of the OGO-I spectrometer; any differences between the two spectrometers are described in the affected sections.

II. The OGO Spacecraft

A. Description of the Spacecraft

The Orbiting Geophysical Observatories (OGO) were built by Space Technology Laboratory, a division of Thompson Ramo Wooldridge at Redondo Beach California. Figure II-1 shows an artist's conception of the OGO spacecraft. The figure indicates the position of the electron spectrometer and the integrating ion chamber, the two University of Minnesota experiments flown on OGO-I and OGO-III. The mission of the OGO spacecrafts was to be a universal flexible stabilized platform in space. The spacecrafts were designed to perform numerous tasks. They contained long booms for mounting experiments sensitive to the disturbing influence of the spacecraft (magnetometers) or experiments which needed a 4π steradian look direction. The integrating ion chamber is mounted on a four foot boom. The electron spectrometer has a very narrow acceptance cone and hence it is mounted inside the main body of the spacecraft with only the entrance slit protruding through the skin of the spacecraft. OGO-I and OGO-III were launched into similar orbits about two years apart. Table II-1 lists the vital parameters for OGO-I and OGO-III on their respective launch dates. The local time of apogee for each of the satellites changed by 1 degree per day in the direction of decreasing angle due to the motion of the earth around the sun. Furthermore, due to

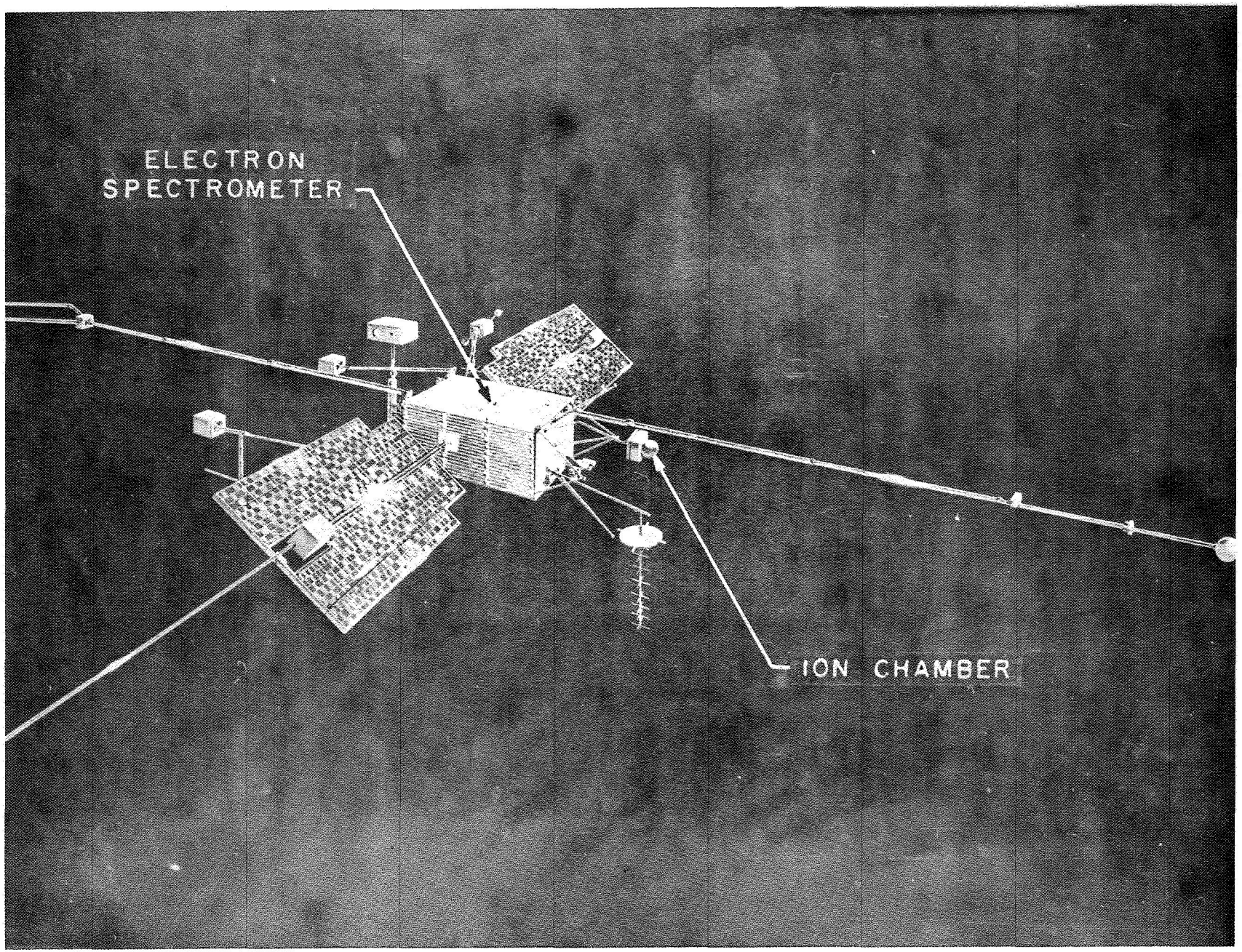

Figure II-1

TABLE II-1

	OGO-I	OGO-III
Launch date	September 5, 1964	June 7, 1966
Height of perigee	280.5 km	295.3 km
Height of apogee	149,408.5 km	122,219.7 km
Inclination of equator	31.11°	30.97°
Local time of apogee	2100 hrs	2300 hrs
Orbital period	63.98 hrs	48.63 hrs
Spin period	11.85	96 sec (variable)

the large apogee of the satellites, the interaction of the sun and moon with the orbits is rather large and therefore perigee increases rather rapidly for OGO-I; it increases somewhat slower for OGO-III. After two years of operation perigee for OGO-I is about 15,000 km altitude and after one year of operation perigee for OGO-III is about 1,000 km altitude. The inclination of the orbit also increases with time. The various drifts and changes in the orbit will be discussed in detail in the sections which correspond to the discussions affected by these changes.

The next section will now discuss the mechanical and electrical configuration of the spacecraft which directly affect the operation of the electron spectrometer.

B. Properties of the Spacecraft

A system of coordinates is introduced along the axis of the OGO spacecraft which has the shape of a large rectangular box. This system is referred to as the body coordinate system and is useful in describing the location of the instrument and the look direction of the spectrometer. For definition of the x, y and z axis see Figure II-2. The spectrometer is mounted on the -z face of the spacecraft such that the look direction of the experiment is contained in the y-z plane and makes an angle of 10° with the -z axis in the direction of the -y axis, that is the look vector $\vec{L}$ is

$$\vec{L} = -.174\ \hat{j}_B - .985\ \hat{k}_B \qquad \text{(II-1)}$$

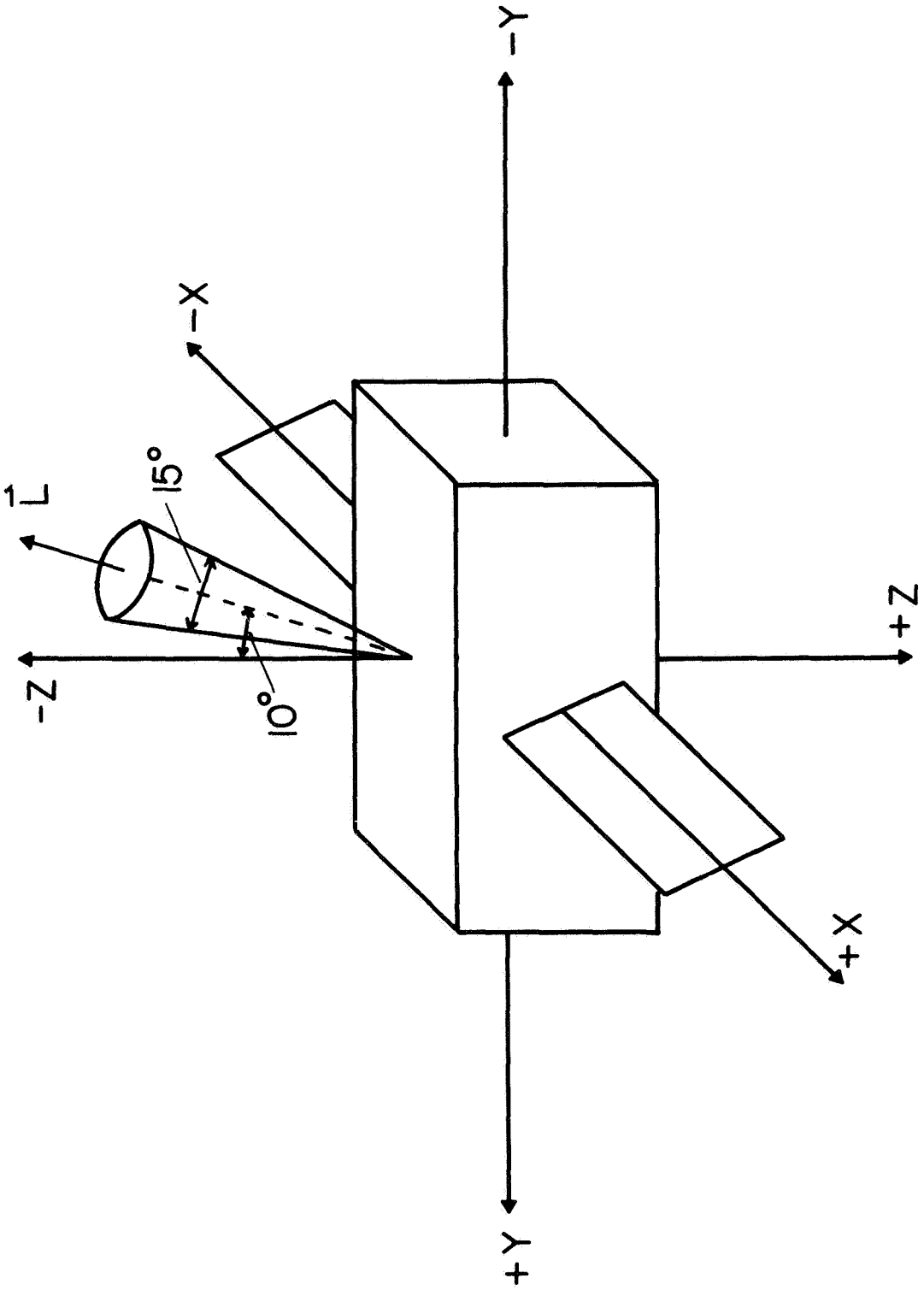

Figure II-2

where $\hat{j}_B$ is a unit vector along the y body axis and $\hat{k}_B$ is a unit vector along the z body axis.

The OGO spacecrafts were designed to be stabilized platforms. The z axis of the spacecraft was to point at the earth and the solar paddles which can rotate about the x axis of the spacecraft were to have their surface perpendicular to the spacecraft sun line. This determined that the x axis of the spacecraft must be perpendicular to the sun spacecraft line and hence a unique orientation was determined for the spacecraft body. Due to attitude control system difficulties, OGO-I did not achieve this stabilized configuration. OGO-III, however, did achieve proper stabilization during the first month and one half of operation. The knowledge of the spacecraft's orientation will be important in determining the experiment's look direction in later sections.

The spacecraft has a rather sophisticated data handling system. Only features which relate to the understanding of how the spectrometer operates will be discussed here. The data system has 128 nine bit words allotted to various experimenters. Of these 128 words, five were assigned to the spectrometer; these words are word numbers 116, 121, 122, 123 and 124. There are nine words inclusive between the beginning and end of a spectrometer readout. The spacecraft has three basic readout frequencies: 1000 bits/sec, 8000 bits/sec and 64000 bits/sec. The spacecraft has two completely independent data systems, each of them capable of operating at

any of the three frequencies. The data could be transmitted to ground stations directly or it could be stored on an onboard tape recorder. In the data storage mode only 1000 bits/sec could be used. Both data systems could be operated simultaneously, one transmitting directly to the ground station at any of the three frequencies and the other storing data on the onboard tape recorders.

III. The Magnetic Electron Spectrometer

A. Design and Construction of the Magnetic Analyzer

The primary constraints in the design of the electromagnet were weight, power and stray field limitations. Since ten pounds was the maximum total weight allotted to the experiment, only about three pounds could be used for the magnet. This indicated that the dimensions of the magnet be on the order of 5-6 cm. The power allotted to the experiment was 3.5 watts and since a high flux is needed in the gap and since only a limited amount of copper wire could be used because of the weight constraint, the magnet was designed with a short duty cycle. A further requirement stating that the stray magnetic field of the experiment must be less than 10 γ at three feet required that the magnet be completely enclosed in soft iron so as to contain the flux. This low leakage flux requirement dictated the use of a cup-core design.

The scientific requirements were that it be capable of bending electrons of up to 4 Mev into the detector and that it have a large cone of acceptance. The focusing properties of the magnet should be such that given a large entrance aperture, all the electrons entering the magnet at the selected energy should strike the detector. The following paragraphs describe a magnet which satisfied these design criteria reasonably well.

A cross-section of the magnet which has cylindrical symmetry is shown in Figure III-1. One can see that the pole faces of the magnet are located inside the magnet and hence the magnet itself serves as the shield to prevent a leakage of flux. The magnet is made of Armco iron which has a permeability of 10^5, the walls of the magnet are just thick enough at any given point to prevent the iron from saturating, the coils consist of 625 turns of #22 copper wire each and the gap between the pole faces is .5 cm. The other dimensions may be obtained from Figure III-1. The weight of the magnet is about 3-1/4 lbs. The location of exit and entrance apertures as well as the cutting of the pole faces to make the magnet double focusing will be described below.

A completely circular pole face has, of course, no special focusing properties; it is in fact quite defocusing The magnet must be designed to allow the largest possible number of electrons of a given energy to reach the exit slit. The horizontal focusing was predicted by geometrical ray tracing through the magnet. Figure III-2 shows the geometrical rays traversing the magnet used on OGO. The vertical focusing was predicted using the calculations of Gross (1951).

At best, the ray tracings and calculations are only rough guesses, since they depend on the fact that the gap between the pole faces must be small in comparison to the size of the pole face. For our magnet this ratio is

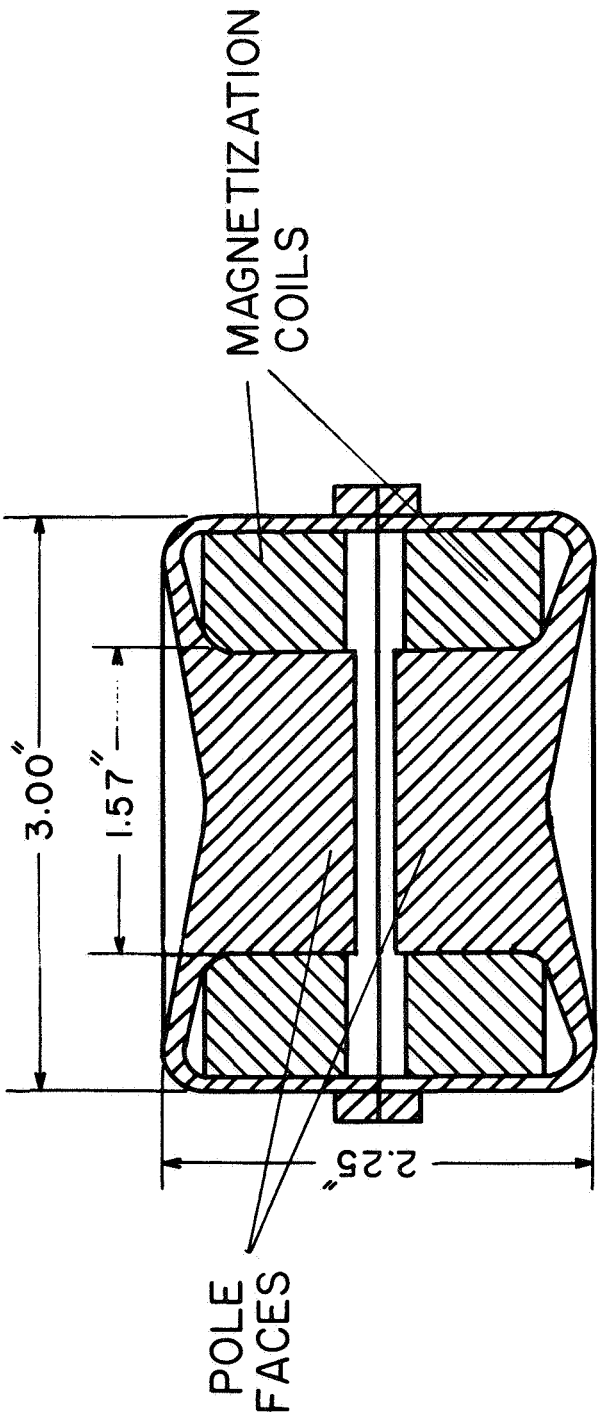

Figure III-1

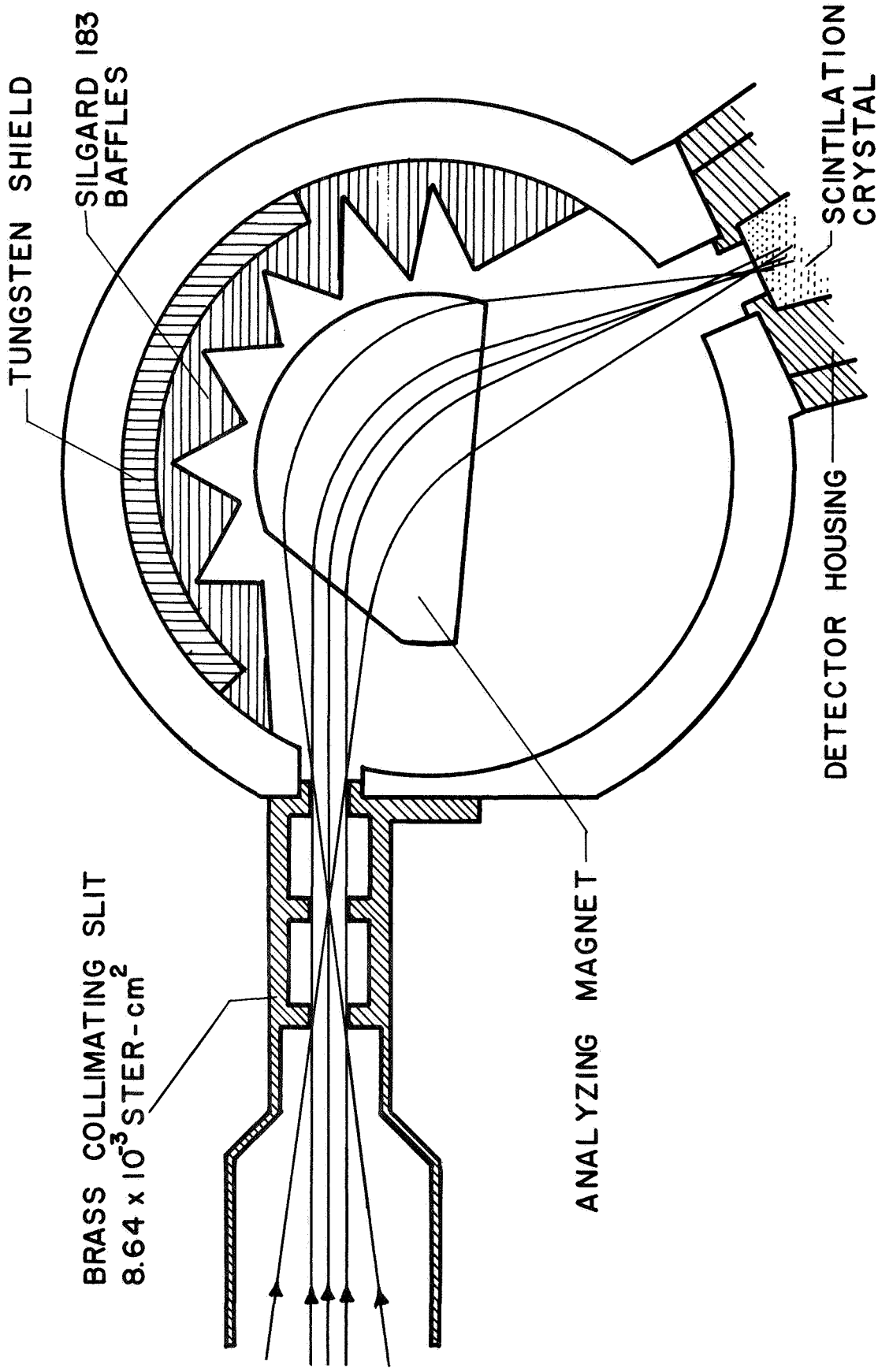
TUNGSTEN SHIELD
SILGARD 183 BAFFLES
SCINTILATION CRYSTAL
DETECTOR HOUSING
ANALYZING MAGNET
BRASS COLLIMATING SLIT
8.64 x 10^-3 STER-cm^2

Figure III-2

about .2, an extremely large ratio. The focusing properties of a prototype magnet were tested using a beam from an electron accelerator capable of producing a 1 cm diameter beam with a current of 10^{-7} amperes. This large current enables one to observe the beam on an aluminum target painted with Willamite (a substance which fluoresces when struck by electrons). Figure III-3 shows how the focusing properties were determined. A monoenergetic beam which covers the entrance aperture is allowed to enter the magnet and is observed at positions 1 and 2 with the aid of Willamite targets. A solid object (a piece of metal) is placed in the beam at the entrance aperture at several places and the location of the shadow is noted. From this, a simple geometrical consideration locates the focal point of the magnet about .5 cm inside the exit aperture. The magnet is somewhat astigmatic with the focus being slightly nearer the target in the horizontal direction by about .3 cm.

B. Magnet Calibration

The first calibration of the magnet must measure the magnetic field B as a function of current I. This is done using an accurate milliameter and a Radio Frequencies Laboratories (R.F.L.) gauss meter. The gauss meter is accurate to $\pm$ 3% and the milliameter to about $\pm$ 2%. Figure III-4 gives the B vs. I curve. This calibration shows that the magnetic field is a linear function of current and that the hysteresis of the magnet is very small (zero intercept).

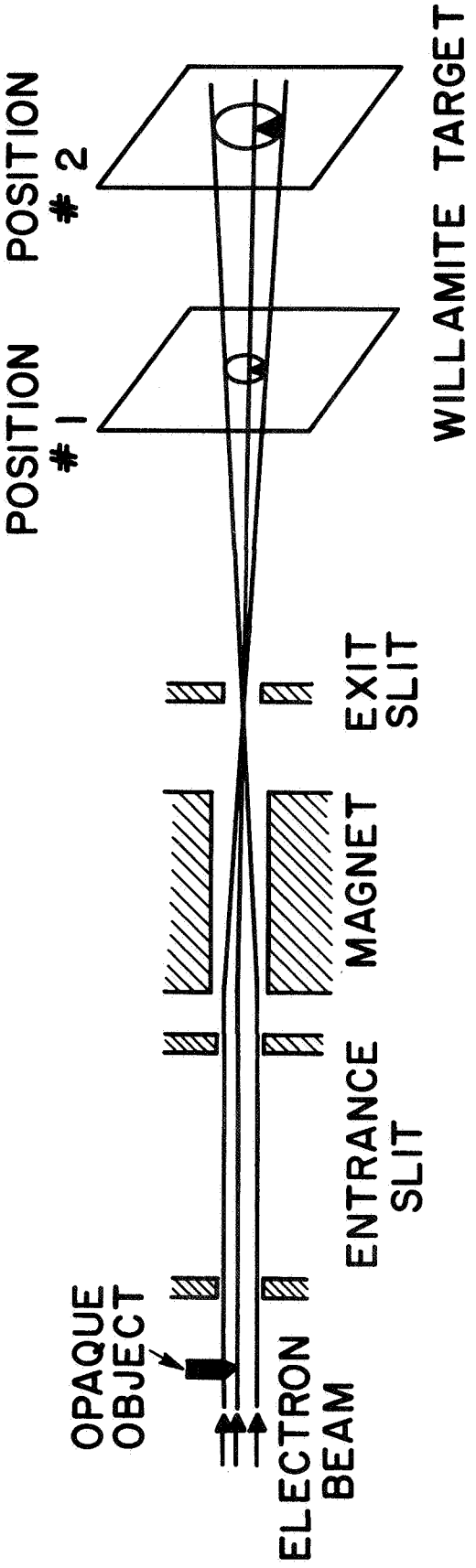
POSITION #2
POSITION #1
WILLAMITE TARGET
EXIT SLIT
MAGNET
ENTRANCE SLIT
OPAQUE OBJECT
ELECTRON BEAM

Figure III-3

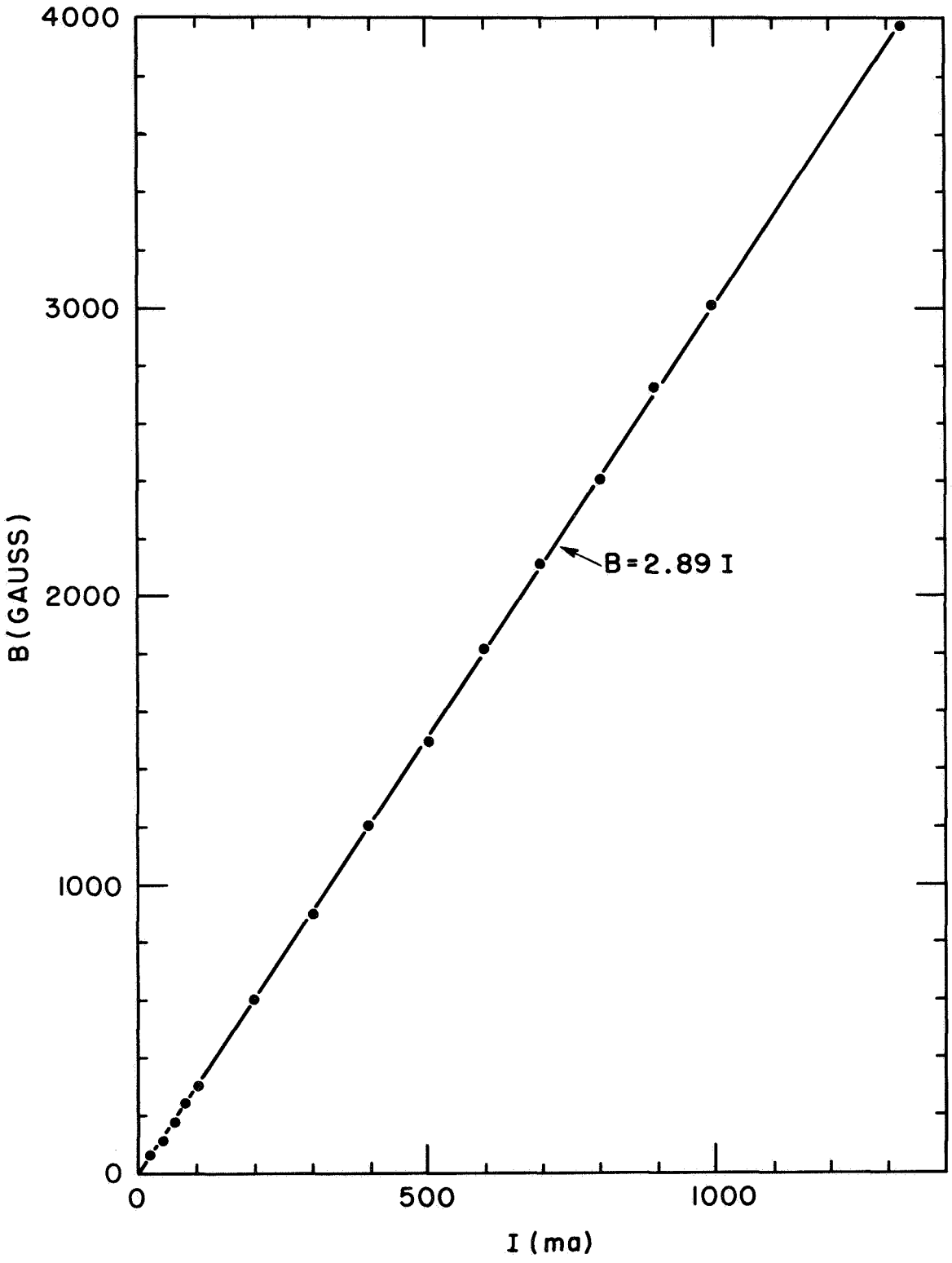

Figure III-4

We have that

$$B = 2.89\ I \qquad \text{(III-1)}$$

where I is the current in milliamperes and B is the magnetic field in gauss. The second calibration obtains the energy response of the magnet. The 10-100 Kev accelerator provides a parallel beam of monoenergetic electrons which are allowed to enter the magnet along the axis of the collimating slit and are detected at the exit slit with a fluorescent target. Figure III-5 gives the experimental points of E vs. I for the OGO-I magnet. We know that the momentum of particles, pc, passing through a magnet, is proportional to B so we have

$$pc = c_1 B = c_2 I \qquad \text{(III-2)}$$

We also know that the kinetic energy E

$$E = [(pc)^2 + (m_o c^2)^2]^{1/2} - m_o c^2 \qquad \text{(III-3)}$$

where $m_o c^2$ is the rest energy. So we have

$$E = [(c_2 I)^2 + (m_o c^2)^2]^{1/2} - m_o c^2 \qquad \text{(III-4)}$$

A best fit solution to the experimental points on Figure III-5 gives $c_2 = 3.14$.

Hence

$$E = [(3.14\ I)^2 + (m_o c^2)^2]^{1/2} - m_o c^2 \qquad \text{(III-5)}$$

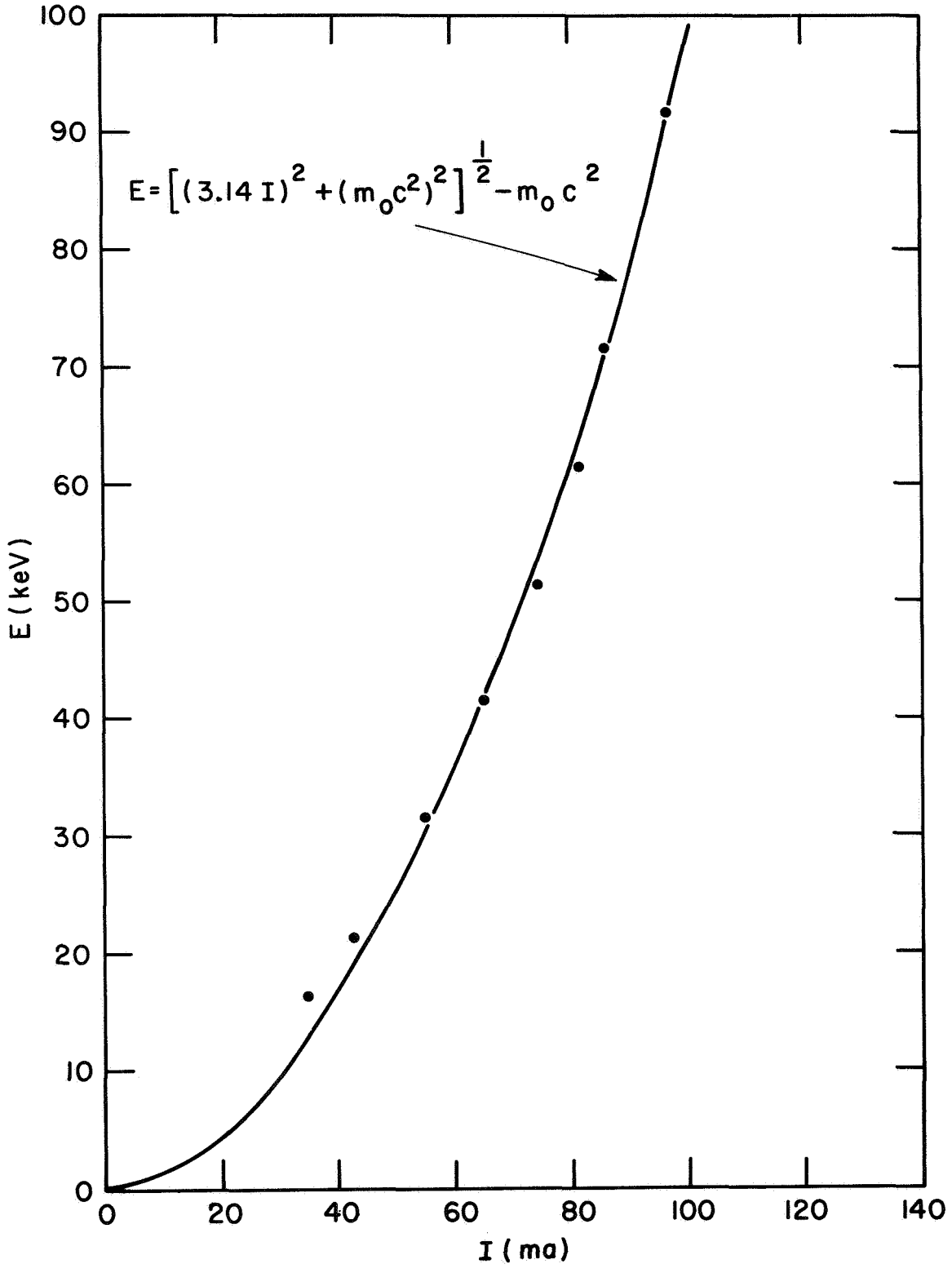
100
90
80
70
60
50
40
30
20
10
0
E (keV)
0
20
40
60
80
100
120
140
I (ma)
$E=\left[(3.14\,I)^2+(m_0c^2)^2\right]^{\frac{1}{2}}-m_0c^2$

Figure III-5

This curve gives an excellent fit above 30 Kev. The points below 30 Kev are suspect because of the troublesome behavior of the electron accelerator for low energies. The beam below 30 Kev is extremely unstable and furthermore the meter measuring the energy of the electrons is calibrated near the upper end of the scale.

Figure III-6 is an extension of equation III-5 to high energies. Several points at energies above 100 Kev were obtained by using a cliabrated solid state detector. A Sr-90 source was placed at the entrance slit of the magnet and the energy at the exit slit was monitored by the solid state detector. The data points on the figure indicate the close agreement with the curve derived from the accelerator measurements. This gives us a well calibrated magnet which can later be used to calibrate the pulse height analyzer and detector system. About 31 watts of power are necessary to bend 4 Mev electrons. This large amount of power could not be obtained directly from the spacecraft. The energy necessary to drive the magnet is stored in a 5400 μf capacitor charged to 30 volts. The capacitor is then discharged through the magnet; the circuit behaves like a simple L R C circuit. The equation for this circuit is

$$I = \frac{V_o}{L\sqrt{\frac{1}{LC} - \frac{R^2}{4L^2}}} \cdot \exp\left(-\frac{Rt}{2L}\right) \cdot \sin \sqrt{\frac{1}{LC} - \frac{R^2}{4L^2}} \cdot t \qquad \text{(III-6)}$$

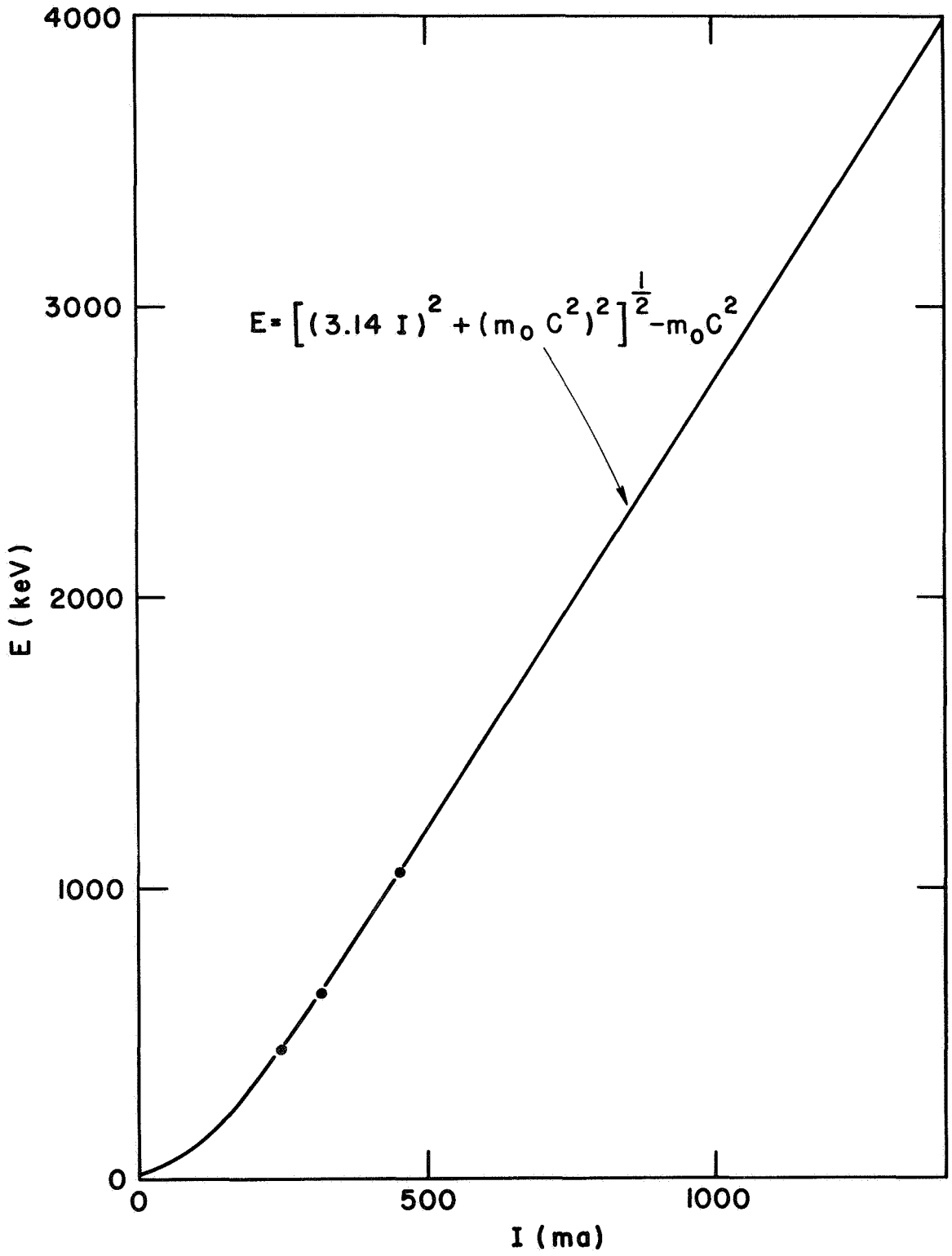
4000
3000
2000
1000
0
E (keV)
$E = \left[(3.14\ I)^2 + (m_0 C^2)^2 \right]^{\frac{1}{2}} - m_0 C^2$
0
500
1000
I (ma)

Figure III-6

where V_o is the initial voltage, L the inductance, R the resistance, C the capacitance, I the current and t the time after turn on. Substituting the circuit constants, R = 12 ohms, L = .5 henry, C = 5400 μf and V_o = 30 volts into the equation, one gets

$$I = 4\, e^{-12t} \sin 15t \text{ amperes} \qquad \text{(III-7)}$$

This gives an oscillating circuit which is rapidly damped to I = 0. For analyzing electrons only the rising portion of the curve is used and the capacitor is disconnected shortly after the magnetic field reaches its maximum. Taking the first derivative, setting it to zero

$$\frac{dI}{dt} = -\, 48\, e^{-12t} \sin 15t + 60\, e^{-12t} \cos 15t = 0$$

$$\tan 15t = 1.25$$

$$t = .06$$

one finds that the maximum is reached about 60 milliseconds after turn on. When the capacitor is disconnected, there are $B^2/8\pi$ ergs of energy E_B stored in the field

$$E_B = B^2/8\pi = (4000)^2/8\pi$$

$$= .64 \times 10^6 \text{ ergs}$$

$$= .064 \text{ joules} \qquad \text{(III-8)}$$

The resistive energy loss E_r in the coils of magnet is

$$E_r = \int_0^{.06} R(I(t))^2 \, dt$$

$$= \int_0^{.06} 12 \cdot 16 \, e^{-24t} \sin^2 15t \, dt = 1.22 \text{ joules} \qquad \text{(III-9)}$$

From this, one sees that the energy lost as heat is much greater than the energy stored in the field and hence no attempt is made to recover the small amount of energy stored in the field. The energy in the capacitors before discharge is E_c

$$E_c = 1/2 \; C \; V_o^2 = 1/2 \times 5.4 \times 10^{-3} \times (30)^2$$

$$= 2.43 \text{ joules} \qquad \text{(III-10)}$$

The energy after discharge is E_c'

$$E_c' = E_c - E_r - E_B$$

$$= 2.43 - 1.22 - .06 = 1.15 \text{ joules}$$

$$\therefore \quad V' = [2 E'_c/c]^{1/2}$$

$$= [\, 2.3/5.4 \times 10^{-3}]^{1/2}$$

$$= 21.3 \text{ volts}$$

That is, after the magnet disconnects, the voltage on the capacitor will be 21 volts and only 1.28 watt-sec of energy

must be added to recharge the capacitors. This recharging takes about 2.5 seconds. Since the circuit is so simple the actual magnet must be very close in performance to the above calculations. This is indeed so. Combining equation (III-1) and equation (III-7) we have

$$B = 11560\, e^{-12t} \sin 15t \qquad \text{(III-11)}$$

The experimental and theoretical curves which agree very well are plotted in Figure III-7. The experimental curve was measured using the R.F.L. Gauss meter, which has a frequency response of one kilocycle.

The magnet described above has two compensating devices in series. One is a thermistor resistor network for temperature compensation and the other is 50 turns of #22 wire to oppose the stray magnetic field. The temperature compensation network consists of a thermistor, having a resistance of 2.5 ohms at 20°C and a resistance of 5.3 ohms at 0°C, in parallel with a 5.6 ohms resistor. This network gave the magnet a resistance of 14 $\pm$ .3 ohms from -20°C to +45°C. (See Figure III-8).

A measurement at the magnetic test site at Goddard Space Flight Center showed that the magnetic field outside the magnet exceeded the specifications given by NASA. Therefore, it was necessary to attempt to cancel the field by adding a field in the opposite direction. Two coils of wire 7 cm in diameter and 25 turns each were added in series to the magnet and positioned outside the iron core coaxially with the

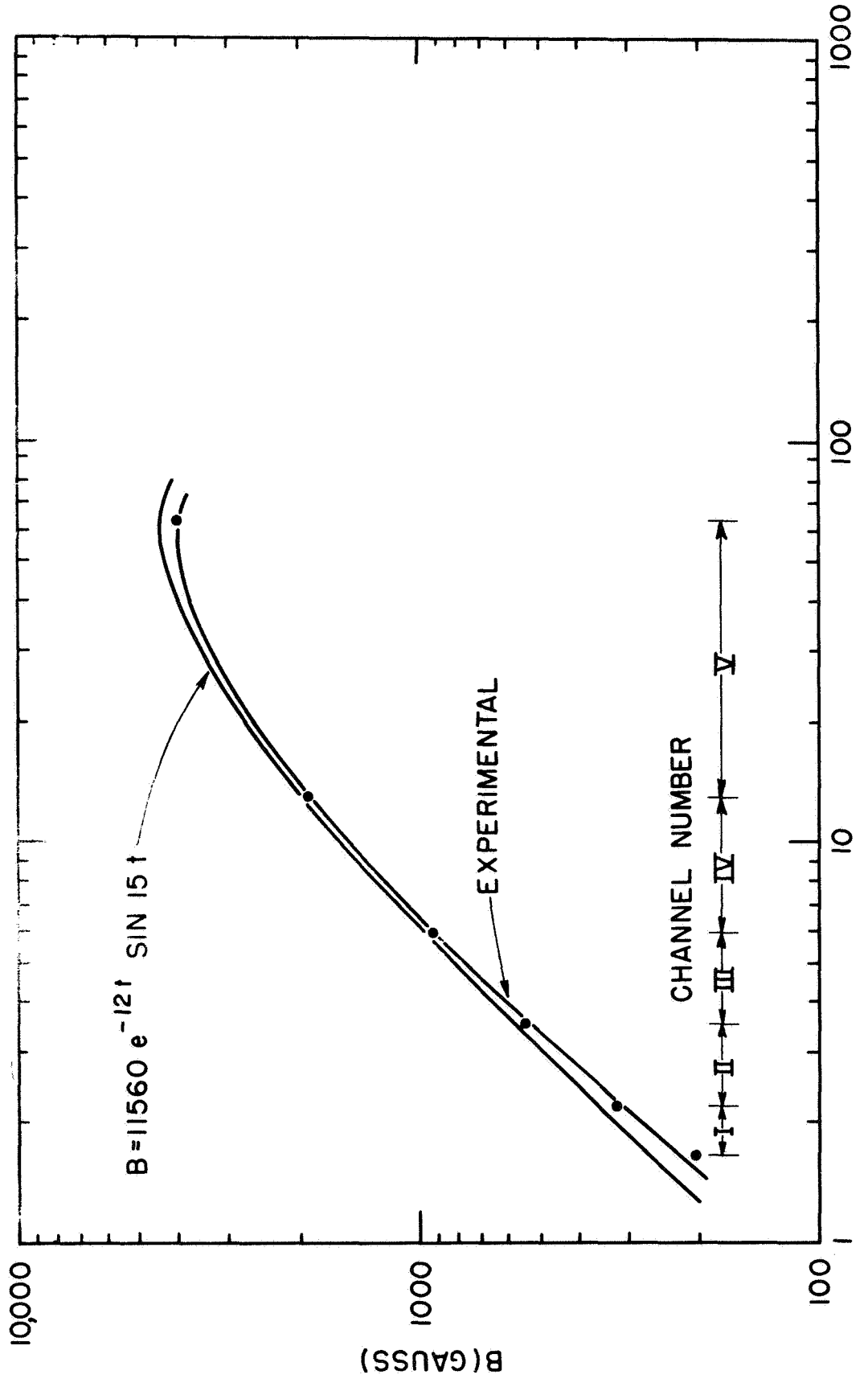
B=11560 e^-12t SIN 15 t
EXPERIMENTAL
CHANNEL NUMBER
I
II
III
IV
V
B(GAUSS)
10,000
1000
100
1
10
100
1000
t(m sec)

Figure III-7

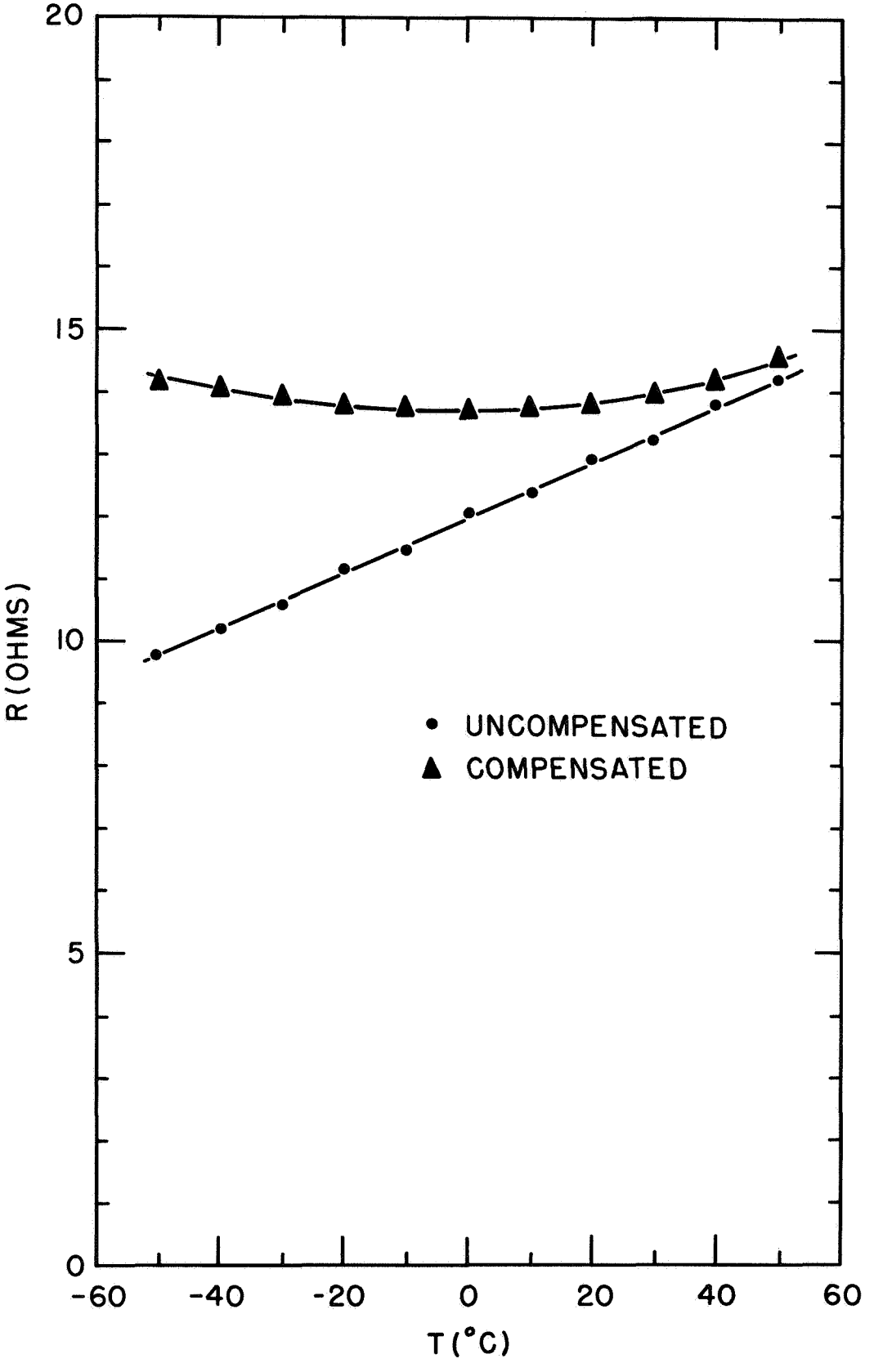
20
15
10
5
0
R(OHMS)
-60
-40
-20
0
20
40
60
T(°C)
UNCOMPENSATED
COMPENSATED

Figure III-8

magnet such that their dipoles were oppositely directed to the magnet. With this technique, it was possible to reduce the stray field by a factor of 5. The maximum stray field was found to be about 30γ at 3 feet, an acceptable value. Figure III-9 gives the stray field as a function of time before and after the addition of compensating coils.

C. Design and Construction of the Detector

The primary constraints on the design of the detector were:

1. It must measure electrons from 50 Kev to 4 Mev efficiently.
2. It must have a low efficiency for detecting bremsstrahlung.
3. It must be capable of handling up to 10^6 counts/sec, up to 10^5 counts without significant dead time loss.

Condition 3 almost rules out any type of end window geiger counter or proportional counter since these are generally not useful beyond 10^4 counts/sec. We expect, for example, during peak rates 100 c/sample in channel I, this corresponds to a rate of 1.6×10^5 counts/sec. No geiger counter arrangements are available to handle such large rates.

Sodium Iodide or Cesium Iodide crystals are ruled out because of their large efficiency for detecting x-rays near 50-100 Kev. These detectors are also quite slow and are not capable of giving μ sec resolution.

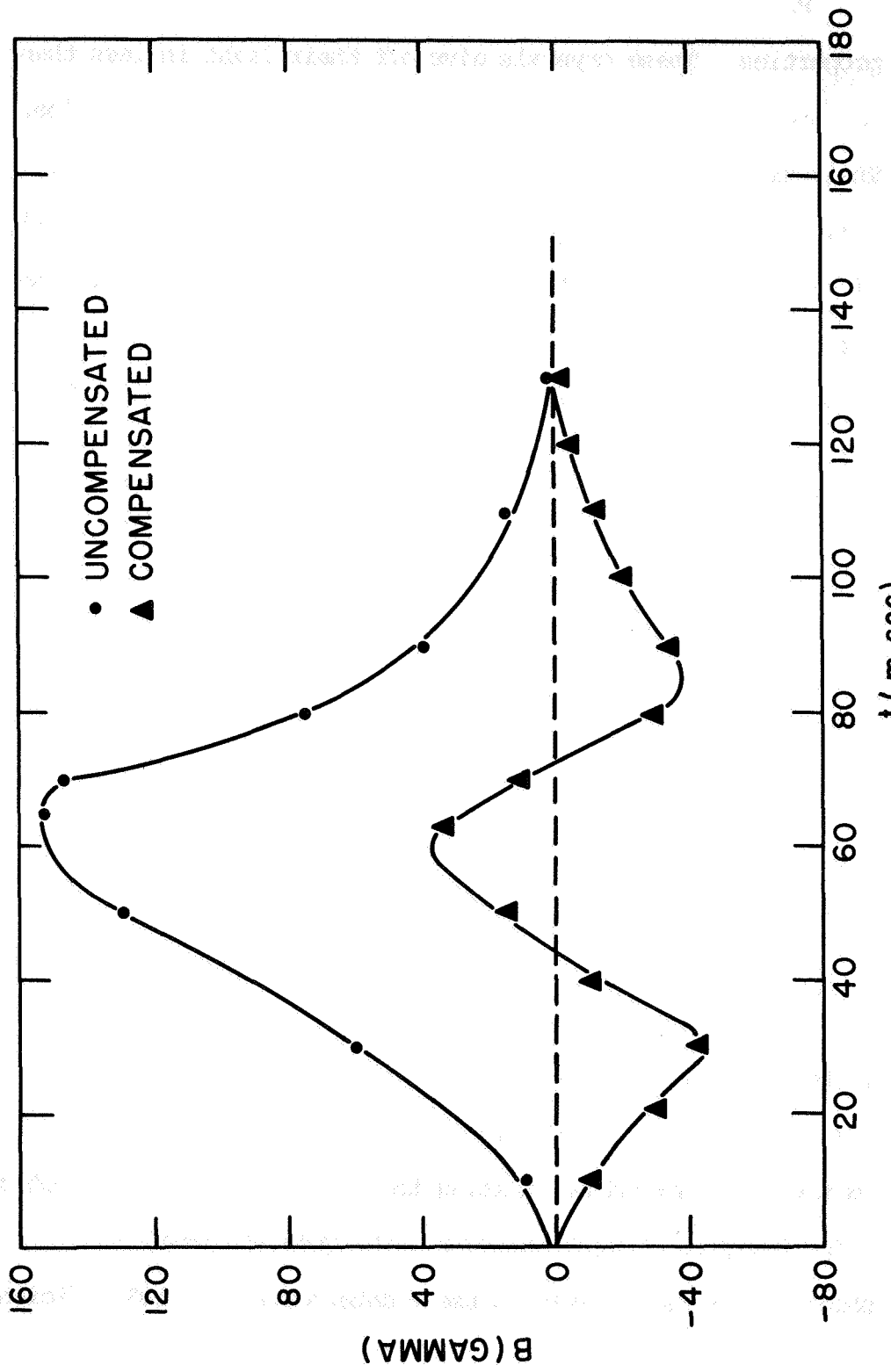
UNCOMPENSATED
COMPENSATED
B (GAMMA)
160
120
80
40
0
-40
-80
20
40
60
80
100
120
140
160
180
t (m sec)

Figure III-9

Plastic scintillation crystals have much more acceptable properties. These crystals give off their light in less than .05 μsec and hence easily meet the high count-rate criterion. Their efficiency for detecting x rays is much less than the efficiency of NaI or CsI crystals. A 1 cm^2 thickness crystal of plastic has a detection efficiency of about 10% for 100 Kev x-rays, NaI and CsI almost 100%, and a geiger counter about .01%. We can use a photomultiplier tube and a window discriminator and perform a pulse height analysis on the scintillator light output. Pulse height analysis turns out to be very important. Most of the bremsstrahlung background is at low energies and is produced by high energy electrons; fortunately, in the radiation belts the low energy fluxes are higher than the high energy fluxes. Therefore, if we wish to measure low fluxes of 1700-4000 Kev electrons the bremsstrahlung flux at 1700-4000 Kev is also very low providing we discriminate against pulses produced by bremsstrahlung having energies less than 1700 Kev. Using a window discriminator we count only pulses which correspond in height to the energy channel currently being analyzed. This limits the bremsstrahlung and also the penetrating particle background by limiting the band width of the detector. Using the pulse height analysis techniques and heavy shielding it is possible to use a detector having 10% efficiency for x-rays.

We used NE -102, a scintillation plastic purchased from Nuclear Enterprises in Canada. NE -102 is capable of giving a strong enough light output for 50 Kev electrons to be easily resolved from the noise with most standard phototubes. The size of the crystal is quite critical. A 2 cm thick crystal is required to stop 4 Mev electrons; however, a 4 Mev light pulse is unnecessary. The crystal need only give off light corresponding to 1.7 Mev for electrons between 1.7 Mev and 4.0 Mev in order to trigger the discriminator. A 1 cm thick crystal proves to be adequate. It stops electrons up to 2.2 Mev and gives off light corresponding to at least 2 Mev for electrons up to about 4.0 Mev. The light output vs. energy was checked up to 3.5 Mev using Ru-106 and the selector magnet. All magnet currents greater than 660 ma (which corresponds to 1.7 Mev) gave peaks greater than the one for 660 ma. Therefore, any electron having energy greater than 1.7 Mev gives a light pulse greater than a 1.7 Mev electron. The crystal was designed in the shape of a truncated cone slightly larger at the end near the phototube to aid in reflecting light into the phototube. The small end of the crystal was made slightly larger than the exit slit of the magnet.

The crystal was shielded very heavily (Figure III-10); the shielding was greater than 15 gm/cm^2 on all sides except the .1 sterad opening occupied by the light pipe. The light

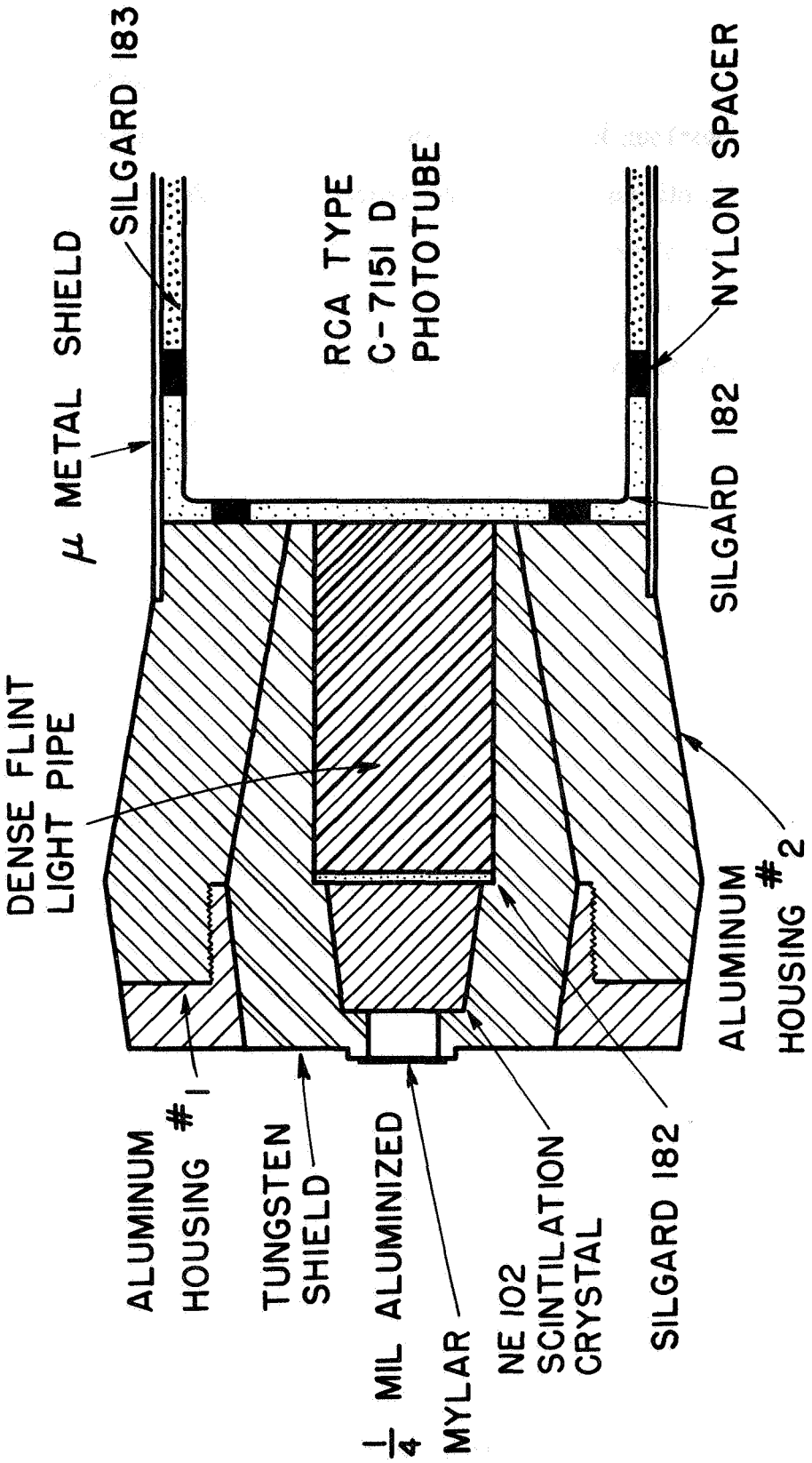

Figure III-10

pipe is a 2.8 cm long and 1 cm diameter glass cylinder. The glass light pipe was made from dense flint purchased from the Hayward Scientific Glass Company of California and had the following properties:

Hayward Scientific Type DF-3	
specific gravity	3.62
index of refraction	1.62

Glasses having specific gravities up to 5.01 were available; however, these glasses are very yellow and quite opaque to the blue light of the scintillation crystal. The light pipe of DF-3 material had a thickness of 10 gm/cm^2. This is 1/3 less than the shielding elsewhere; however, the opening in the tungsten shielding for the light pipe subtends an angle of less than 1% of the total 4π solid angle. Therefore, for all practical purposes the detector was shielded by 15 gm/cm^2 of tungsten on the sides and by more than 15 gm/cm^2 of magnet assembly on the front. Care was taken to design the shape of the tungsten shield such that any given path through the tungsten and other material is just greater than 15 gm/cm^2. This accounts for the reduced diameter of the tungsten shield at the phototube end. A 1 gm/cm^2 thickness of aluminum was added to the shield to reduce the production of x-rays in the tungsten shield.

The phototube necessary for detection of the light output must be able to distinguish 50 Kev pulses from the dark current noise of the tube. The tube must also be

ruggedized to survive the intense vibrations of a rocket launch. The RCA developmental type C-7151D met these criterion quite well and will be described in the next section.

The assembly of the detector and photomultiplier was by far the most difficult problem in the construction of the spectrometer. Several of the problems encountered were: making the crystal face opaque to light, giving the crystal sides high reflectivity, coupling the crystal to the lead glass, coupling the lead glass to the phototube and preventing arcing from photocathode to the phototube shield.

The top face of the crystal must be transparent to electrons, but opaque to light. In order to be classified as transparent, 50 Kev electrons should lose no more than 5 Kev of energy in passing through the light tight layer. Furthermore, this layer should be highly reflective such that the light will be reflected down to the phototube. We decided to use aluminum plating because Al has a low Z and hence does not scatter electrons as strongly as, for example, gold. Aluminum is also rather easily plated in a vacuum. A 20 to 25 mil tungsten filament was used to evaporate the aluminum. Tungsten is soluble in aluminum and hence only small amounts of aluminum could be plated at any given time and the tungsten filament had to be replaced frequently. One had to exercise great caution when plating to prevent the aluminum from spattering, a problem that was

avoided by keeping the evaporation heat low. One also had to use care to prevent the plastic scintillation crystal from melting, the softening temperature of plastic is ≈60°C. By keeping the crystal at least 6-10 inches from the filament softening of the crystal was prevented. The plating was done in a large bell jar which could be evacuated to 10^{-5} - 10^{-6} mm Hg. Generally, any pressure $<10^{-4}$ mm of Hg proved adequate for plating. Higher pressures caused a darkening of the plating presumably due to sputtering of the aluminum.

The thickness of the plating was experimentally determined. The geometry of the crystal was fixed with respect to the filament and a fixed amount of aluminum was put on the filament. All the aluminum was then evaporated from the filament. This evaporation process was then repeated six times and produced a coating of measurable thickness. The plating could be peeled from the crystal face and measured with a micrometer. The thickness was found to be 0.0001 inches which is about 7×10^{-4} gm/cm^2 of Al and corresponds to an energy loss of 15 Kev. Reducing the thickness to about 2×10^{-4} gm/cm^2 by doing only two plating processes corresponded to an energy loss of 7 Kev which is an acceptable loss. Some experimental work was done with the thicker platings which were much more opaque to light, but it was found that the coating would peel away from the crystal face due to the differences in thermal expansion, after cycling these crystals from -25°C to +45°C at a rate of ten degrees per hour. The thinner

coatings, $<3 \times 10^{-5}$ inches, did not separate from the crystal after numerous temperature cycles. Light tight coating of thickness less than about 3×10^{-5} inches were extremely difficult to obtain. After much care to prevent dust particles from settling on the crystal following cleaning and after many attempts an occasional light tight crystal was obtained. When this crystal was then assembled the face of the crystal had to contact a rubber gasket or some other such boundary and the light tight seal would soon be broken. If this did not happen during assembly it was sure to happen during vibration testing and hence the idea of a light tight coating was abandoned, instead the crystal was coated with about $1\text{-}2 \times 10^{-5}$ inches of aluminum. This thickness is light tight except for any small pinholes. It is also "transparent" to electrons having an energy loss of less than 5 Kev. To make the assembly light tight 1/4 mil aluminized mylar was glued across the entrance slit of the detector assembly, mylar side down. The electrons lose approximately 10 Kev in the aluminized mylar. This makes the total energy loss of the entrance window approximately 10-15 Kev. This energy loss is somewhat more than we had hoped but it was evident that this was the only reasonable solution. A test of the detector system showed that the mylar window did indeed decrease the resolution for measuring 50 Kev electrons, but it also showed that the 50 Kev peak was still discernible. Even though both the crystal and the aluminized mylar may

have pinholes, the detectors were tested to be light tight under intense direct light.

The sides of the crystal as well as the sides of the glass shield had to be made reflective such that light collection at the photocathode is a maximum. There are two types of reflective coatings, one is diffusive reflection using MgO powder with which any light not reflected by the surface of the glass is diffusively reflected back into the detector system by the powder; the other is the method of direct reflection in which the sides silvered with aluminum reflect the light back into the system. Detectors using each of the methods of reflection were built. The light output of each system was measured using a standard phototube and Co-60 source. No large differences in light output were detected and hence the direct reflection method was used because it allowed easier assembly of the crystal and the crystal could also be more completely potted to protect it against vibrations. The MgO powder, furthermore, had a tendency to move around during vibration testing which could conceivably cause gain changes.

The top and sides of the detector and the sides of the light pipe were silvered with aluminum. After silvering, the detector and light pipe were mounted in the tungsten shield. The entire assembly was potted in Silgard 182 which was thoroughly out-gassed in a vacuum chamber and then cured over night at 45°C. The aluminum housing part #2 (see Figure III-10)

was epoxied to the tungsten shield such that the detector could be screwed into part #1 of the aluminum housing which was attached to the magnet without disturbing any of the interfaces.

The RCA type C-7151D developmental type tubes used with this experiment have a gain of 10^5-10^6 at an operating voltage of approximately 800 volts. About a dozen tubes of this type were tested for gain and noise characteristics. The gain of the tubes varied by at least a factor of ten and the noise characteristics varied by a factor of 2 to 3. The two tubes with the best noise and gain characteristics were reserved for use with the flight models and the other better tubes were used for backup and prototype units. The cathode and 10 dynodes of the tube were supplied by a regulated power supply which remained stable to within .1% from -20°C to +45°C. The negative high voltage was supplied to the cathode and a divider chain of 10 Meg $\pm$ 2% Pyrofilm Resistors supplied the high voltage for the 10 dynodes. Dynodes # 8, 9 and 10 were also stabilized by their own high voltage supplies such that for large counting rates, these last 3 dynodes would be capable of supplying enough current without changing their voltage (See Figure III-11). The divider chain was fastened directly to the wires coming out from the base of the tube.

The phototube was shielded by an aluminum tube covered with μ metal. The μ metal served to insulate the phototube from the stray magnetic field of the magnet, the earth's field and fields produced by the power supply.

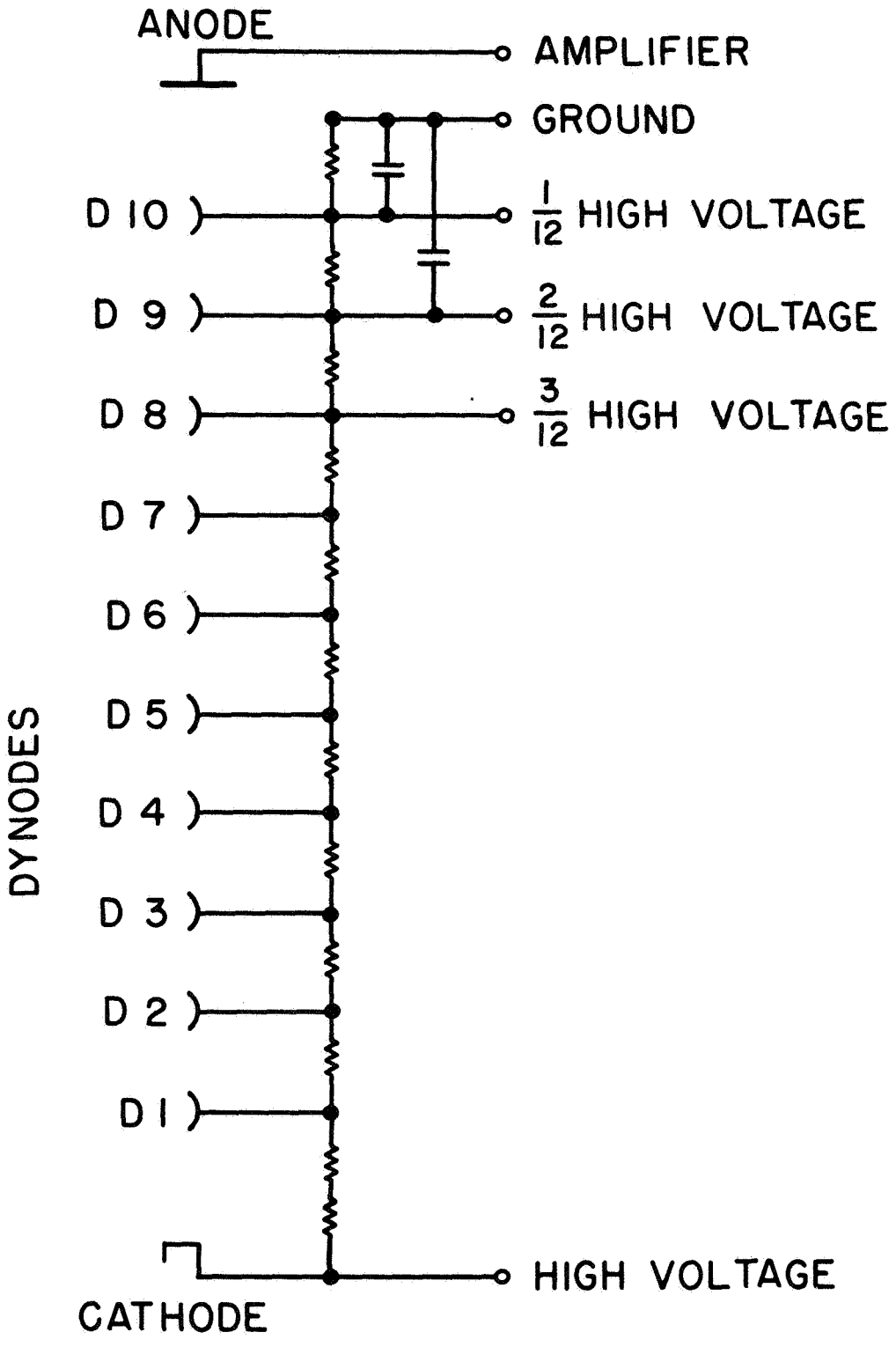

Figure III-11

Since the photocathode was operated at high voltage, there was a tendency for the photocathode to arc through the glass and potting compound to the phototube shield. The problem was solved using a sufficient thickness of the potting compound between the detector and phototube and between the phototube and the tube shield. A thickness of about 1/16 inch to 1/8 inch of Silgard proved to be thick enough. Thicknesses less than 1/16 of an inch caused considerable arcing. To ensure the proper thickness after potting Nylon spacers were placed between the tube and tube shield and between tube and the detector. The interface between tube and detector was potted with clear Silgard 182 and the space between tube and tube shield as well as the divider chain were potted in black Silgard 183. All Silgard used was completely out-gassed and all bubbles were removed in vacuum before curing in the oven.

This completed the detector assembly. After assembly the gain of the detector was checked for changes in gain as a function of pressure. Any irregularities would indicate an improper interface between the various optical components of the system. The assembly was also checked for noise characteristics. Large tube noise would indicate electrical leakage in the divider chain. The assembly was furthermore observed for arcing between tube and tube shield. Such an arc would give rise to extremely large ragged pulses at the anode. If the assembly did not meet the above require-

ments, it was disassembled, cleaned and rebuilt.

D. Detector Calibration

Once the construction and stability of the crystal photomultiplier assembly had been verified the response of the system had to be found. The most critical region was the region near 50 Kev; 50 Kev is the approximate limit of detectability using a plastic scintillation crystal. Therefore, the geometry, noise characteristics and light collection must all be favorable in order to separate the 50 Kev peak from the noise. For this work the small 100 Kev electron accelerator was used.

The detector assembly was placed into the beam and the response of the detector was obtained for low energies. Figure III-12 gives the curves for the response of the detector for energies from 50-100 Kev. One can see that at 50 Kev the peak is just discernible from the noise, whereas at 100 Kev the peak is well separated from the noise.

In order to understand the sequence of events necessary to calibrate the detector one must understand the operation of the amplifier and window discriminator. The anode signal from the phototube is split, each going to a grounded base stage "preamplifier" (see Figure III-13). The output from one of these grounded base stages goes to a test output-jack, the other is fed into a switched divider network that acts as a gain change network for the fixed gain charge sensitive amplifier and fixed window discriminator. The switching of

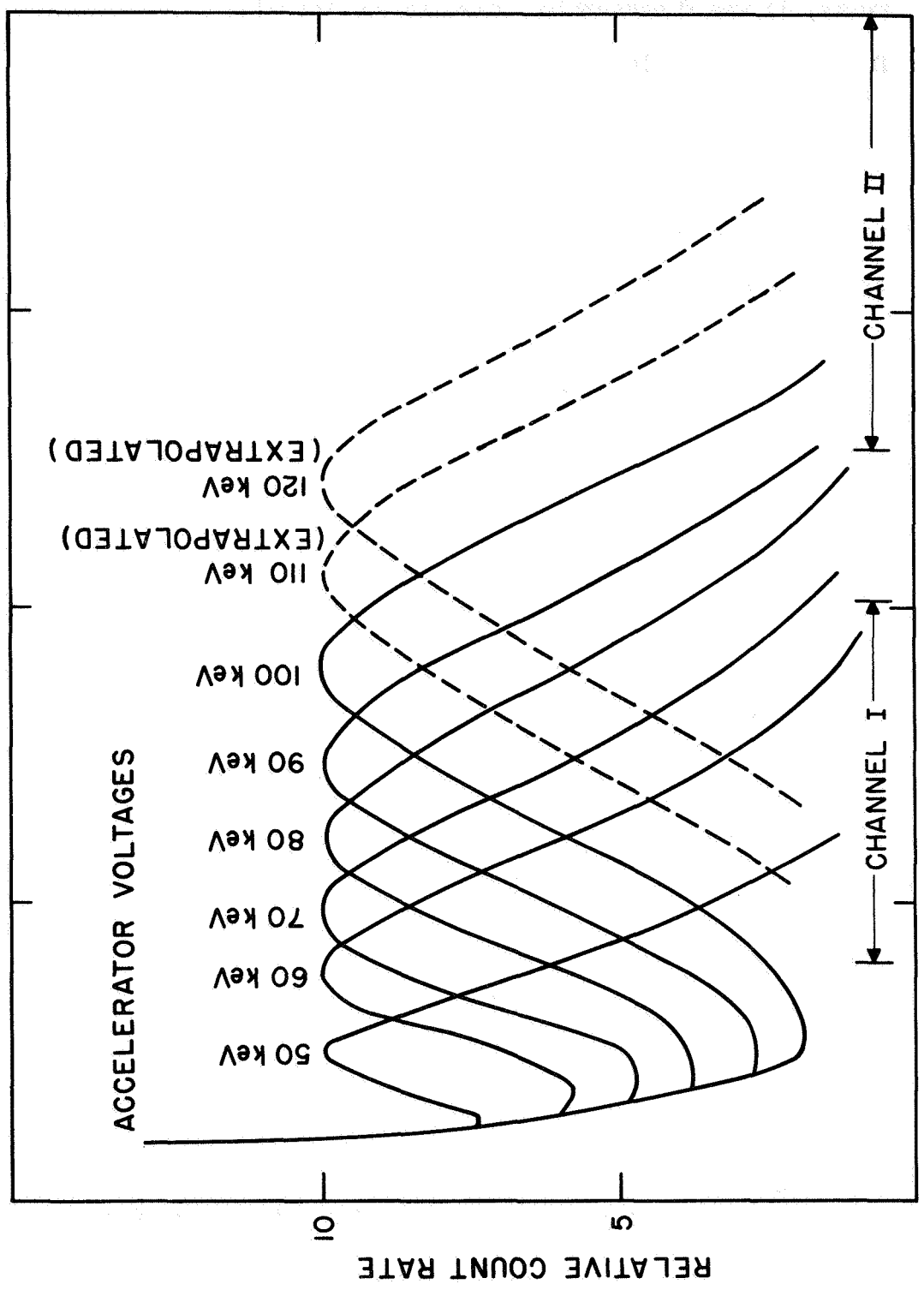

Figure III-12

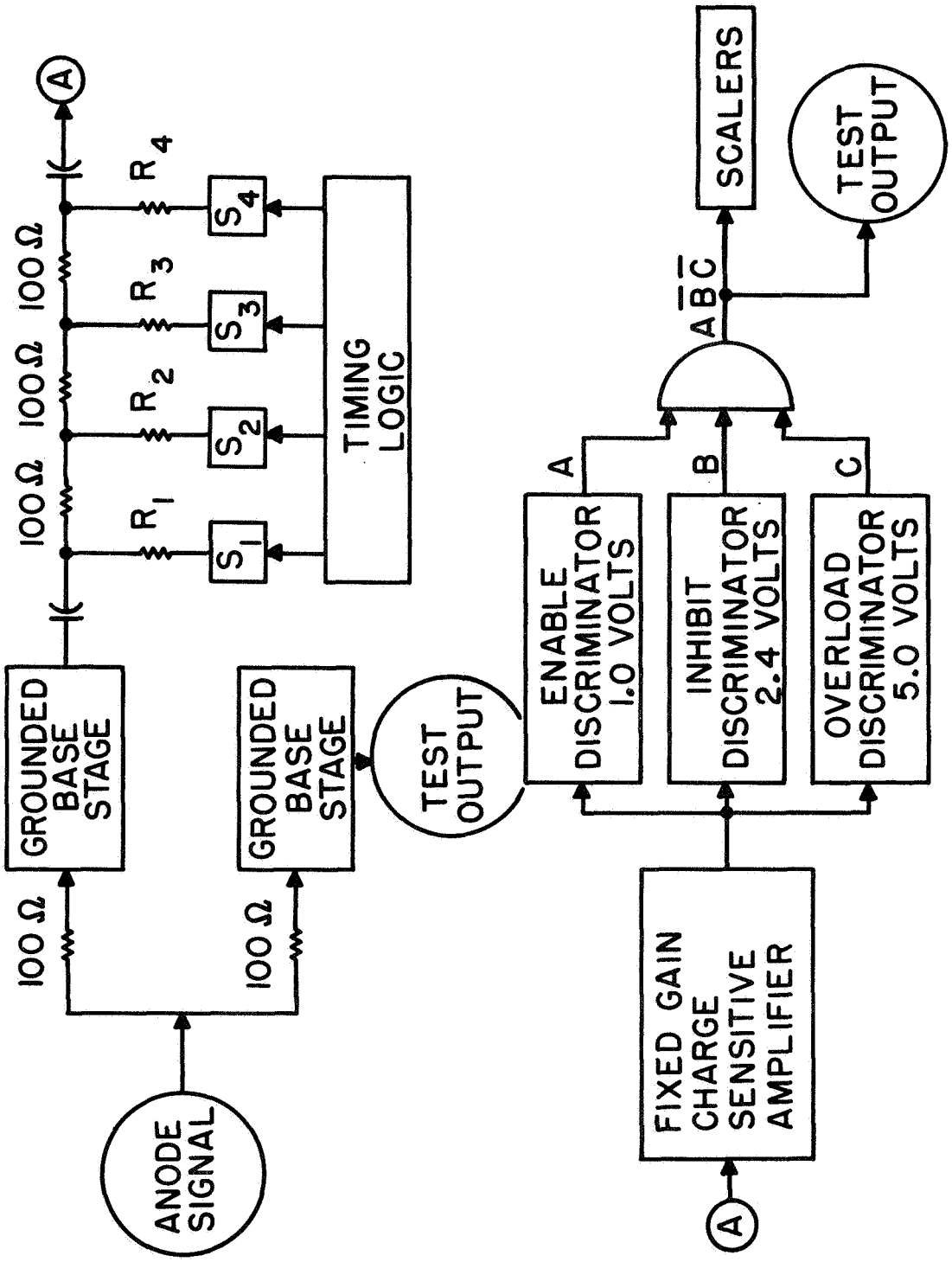

Figure III-13

the divider network is controlled by the operating logic of the experiment. For the lowest energy channel all switches are open and none of the signal is shunted to ground (see Figure III-13). For channel II switch S_1 is closed, for channel III switches S_1 and S_2 are closed, for channel IV switch S_1, S_2 and S_3 are closed and for channel V all switches are closed. The closing of each successive switch decreases the signal reaching the amplifier by approximately 2.4. The exact value is adjusted to take into account the actual energy response of the detector system.

Since the gain of the amplifier is fixed the voltage of the phototube is adjusted such that the overall gain of the system with all the switches open determines the lower edge setting of channel I. The upper discriminator setting is 2.4 times that of the lower discriminator setting. Therefore, the energy window location for channel I is determined exclusively by adjusting the phototube high voltage. The windows for channels II-V are calibrated by adjusting the shunting resistors R_1 to R_4. Channels II-V must be adjusted in order, the lowest channel first, because adjusting the smaller channels affects all of the larger channels.

One of the first figures necessary for the proper adjustment of the discriminator edges is the pulse height response of the detector for monoenergetic electrons from 50 Kev to about 2 Mev. 50 Kev to 100 Kev electrons are obtainable from the accelerator, 100 Kev to 2 Mev electrons

are available from the selector magnet using the magnet energy calibration of Figure III-6 and a Sr-90 source. All pulse heights were measured using a Nuclear Data 1024 channel pulse height analyzer (only 256 channel resolution was used for each measurement). A calibrated, charge sensitive variable gain amplifier was used to amplify the signal to 3 volts for pulse height use. Various gain settings were necessary to cover the large range in pulse heights and still remain in the pulse height analyzer's linear region of response. All pulse height measurements were transformed to a single scale using the intercalibration between the various gain settings of the amplifier. The input source for the magnetic selector magnet was the Sr-90 source which has a spectrum dependent on energy. This spectral dependence was removed and the curves normalized to a white source. Figure III-14 gives the pulse height distribution for various magnet current settings; it also contains, for comparison, the 100 Kev pulse height distribution from Figure III-12 (dotted line). Using Figures III-6, III-12 and III-14 one can get a complete pulse height vs. energy calibration for the detector system. The calibration curve is plotted in Figure III-15. Each experimental point is labeled as to its source of measurement. The figure also contains calibration points determined from the end-point energy of Sr-90 (2.2 Mev) and the end point energy of Cl-36 (.71 Mev) as measured by the detector system. All

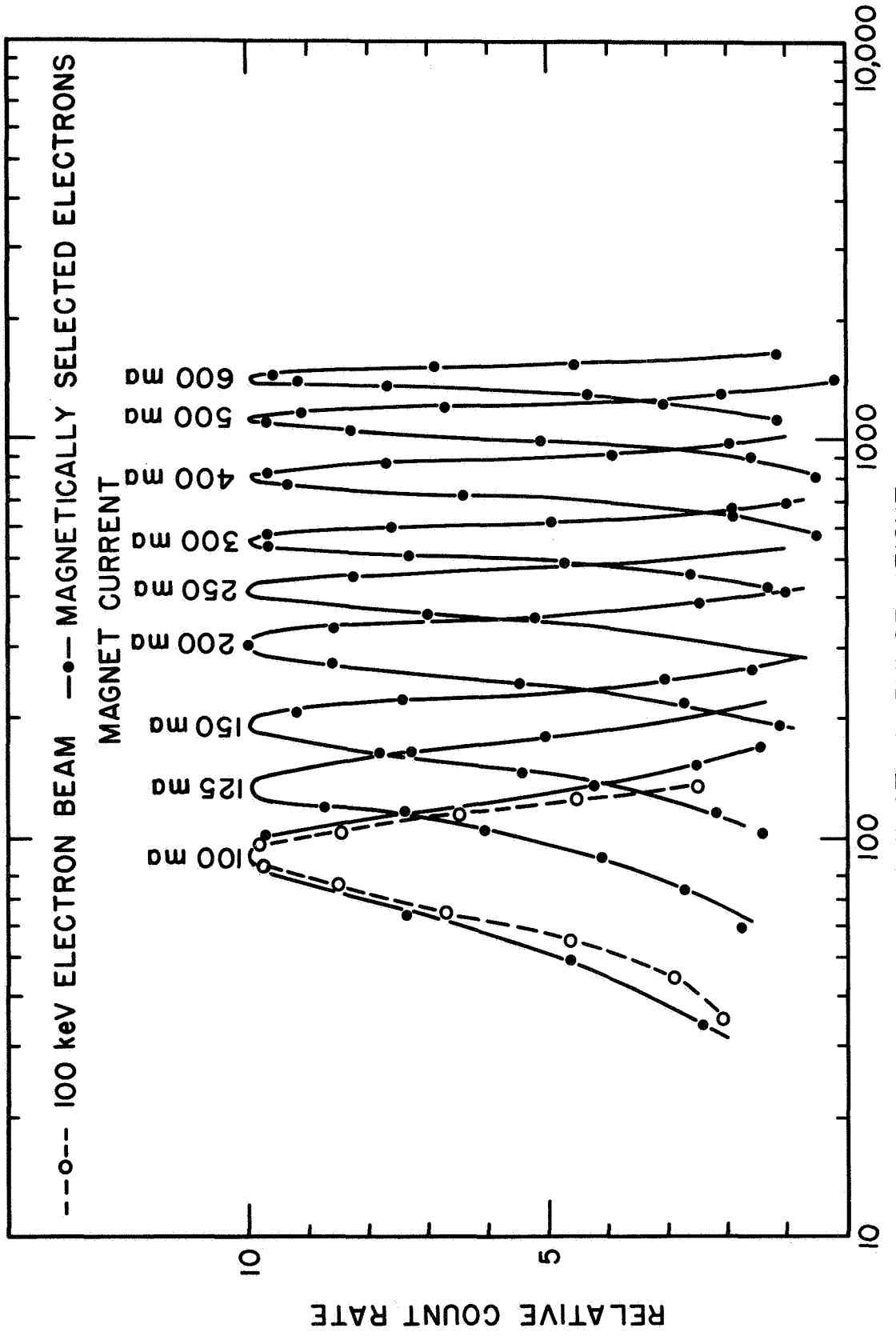

Figure III-14

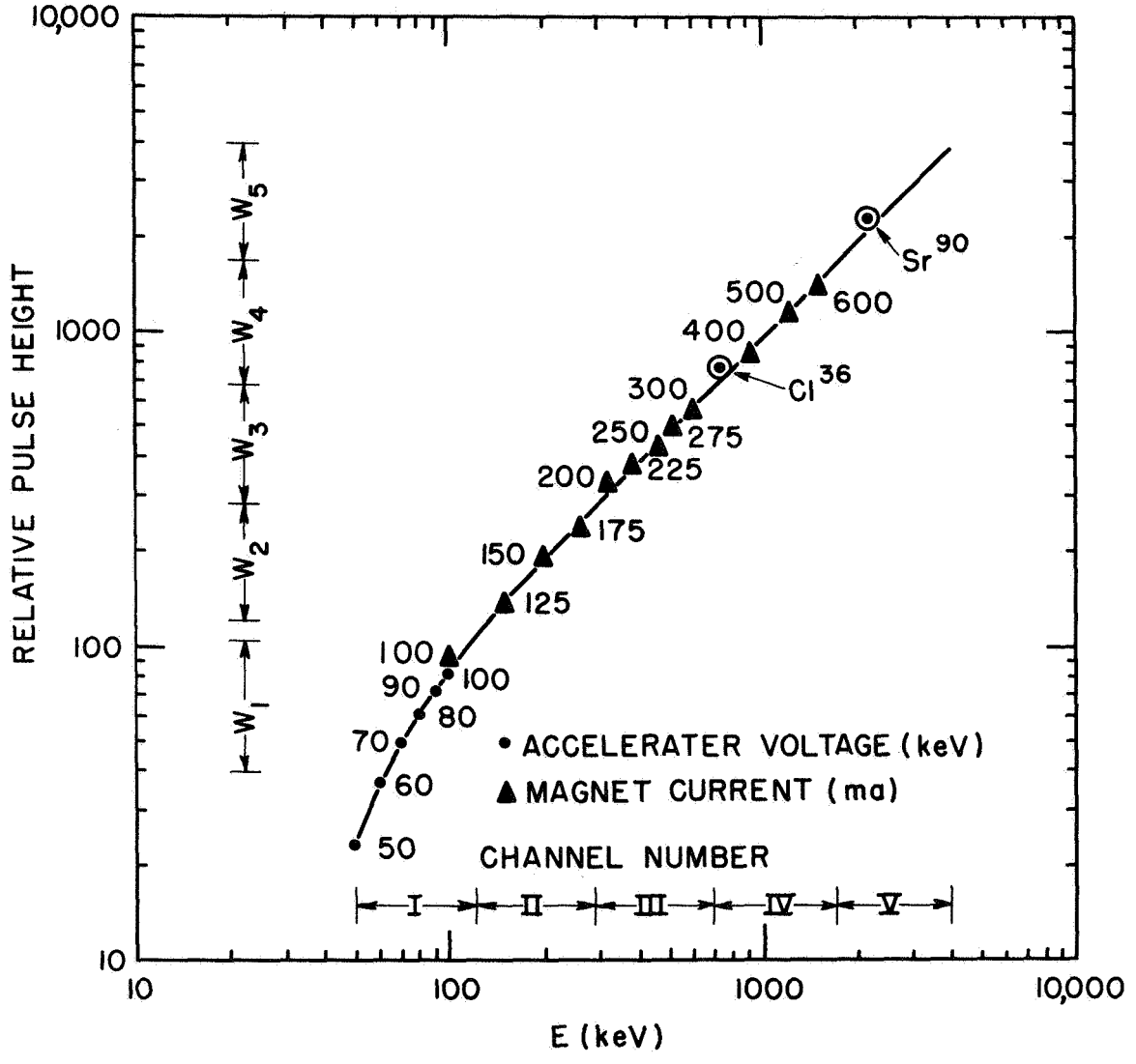

Figure III-15

points from the three different sources of electrons fall on a single curve. The curve is linear above about 130 Kev; below 100 Kev the curve becomes quite non-linear. This non-linearity is due to the losses in the light tight window which are no longer negligible and the inherent non-linearity of scintillators for very small energy losses.

The window settings for the five energy channels W_1-W_5 are also indicated on Figure III-15. W_2-W_5 are quite easily set because of the linear response of the system and because the width of the pulse height distribution from a monoenergetic electron beam is small compared to the channel width. However, for channel I the pulse height distribution for a monoenergetic beam is as wide as the window itself. The edges for this window were set such that the efficiency for detecting 50 Kev electrons and 120 Kev electrons is about the same and such that the peak efficiency is at about 85 Kev, the middle of the energy window. This reasonably symmetric response gives an efficiency calibration that is quite independent of spectrum. If the efficiency is peaked near one end then the efficiency varies strongly between flat and steep spectra. Figure III-16 is a plot of the relative efficiencies of window I through window V.

Once the window edges were set the gain switching of the amplifier must be synchronized to the magnetic field. The magnetic field is a function of time

$$B = B\ (t)$$

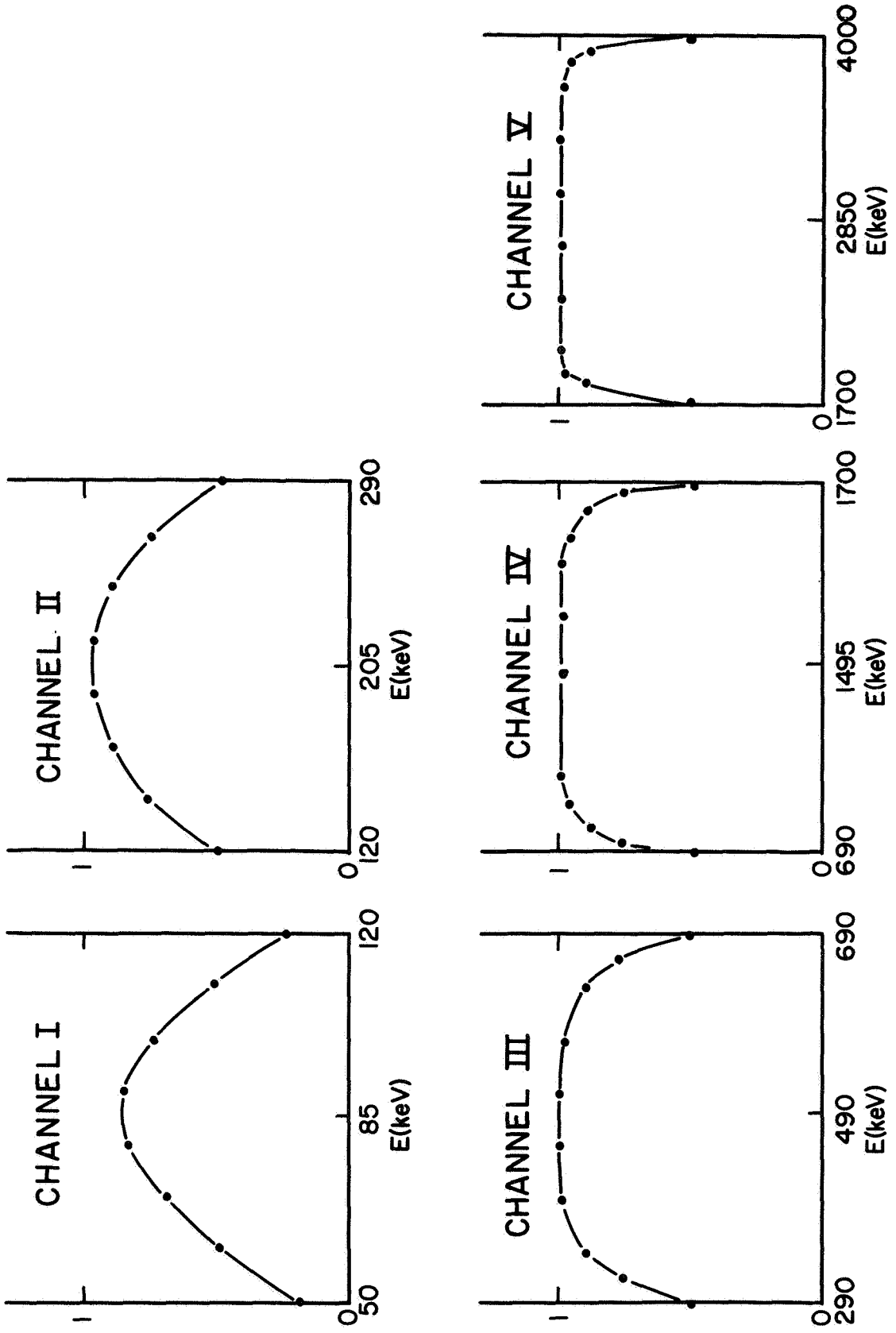

Figure III-16

Figure III-7 gives the magnetic field as a function of time and since we know at what field strengths we cross from one channel to the next, the times at which the gain must be switched are accurately known. Table III-1 summarizes the conditions when the gain of the amplifier must be switched from one window to the next. The logic contains a 64 kc clock, which remains stable to .1% from -20°C to + 50°C and controls this switching operation. Table III-2 and III-3 gives the sequence of events that are initiated when this clock is turned on. All events except B(t) in the analysis cycle are controlled by the timing of this very accurate 64 kc clock. B(t) is determined by the electrical constants in the RCL circuit and since RCL and V_o are temperature stable, the magnet curve is accurately repeated each time. A background measuring cycle is the same as the data cycle except for step 2 in Table III-2. The magnet sweep is not started and B = 0 for the entire cycle.

The repitition rate of the above analysis cycles is controlled by a clock having a period of 1.4 seconds. This clock removes the 64 kc clock lockout once every 1.4 seconds and an analysis cycle begins. It also drives a set of 3 binary scalers which determines whether a cycle is to be a data cycle, a background cycle or a sync cycle. These three scalers constitute a scale of eight. Cycles 1, 3, 5 and 7 are data cycles, cycles 2, 4 and 6 are background cycles,

TABLE III-1

Analyzing Magnet Constants at the Channel Switching Times

Channel	E(Kev)	I(ma)	B(gauss)	t(msec)	Δt(msec)
	-	0	20	0	
	50	72	208	1.63	
I					.59
	120	113	327	2.22	
II					1.31
	290	189	547	3.53	
III					2.31
	690	333	963	5.84	
IV					7.31
	1700	659	1909	13.15	
V					51.30
	4000	1400	4000	64.45	

TABLE III-2

Sequence of Events during an Analysis Cycle

Time (msec)	B (gauss)	E (Kev)	Event
-32.00	20	-	Stop magnet capacitor charging Turn on amplifiers Turn on timing logic
0.00	20	-	Initiate magnet sweep Preset all logic circuits Turn on 64 kc clock
1.63	208	50	Initiate channel 0 data transfer
2.22	327	120	Initiate channel I data transfer
3.53	547	290	Initiate channel II data transfer
5.84	963	690	Initiate channel III data transfer
13.15	1909	1700	Initiate channel IV data transfer
64.45	4000	4000	Initiate channel V data transfer Turn off magnet Remove readout lockout Turn off amplifiers and logic Resume magnet capacitor charging

NOTE: The sequence of events for the channel i data transfer cycle is listed in Table III-3.

TABLE III-3

Channel i Data Transfer Sequence

1. Inhibit data transfer to scalers
2. Transfer contents of scalers to ISR
3. Reset scalers to zero
4. Set gain of amplifier to channel i + 1
5. Remove data transfer inhibit, start accumulating data in the scalers for channel i + 1
6. Shift ISR until highest order bit is a one or until a maximum of 7 shifts has occurred
7. Transfer 6 high order bits of ISR to 6 low order bits of channel i storage
8. Place 7-number of shifts into the 3 high order bits of channel i storage

i varies from 0-5

Storage for channel 0 is a dummy storage cycle

and cycle 0 is the sync cycle. During the sync cycle the Intermediate Shift Register (ISR) (see next section) is prevented from shifting and hence the upper 3 bits of the five storage registers are set to one. This would correspond to an unreasonably large number and hence is a useful unique sync. The sync is necessary in order to separate data from background when the two might be equal and is also necessary for computer reduction of data.

Eight complete analysis cycles will be called a data frame. Each analysis cycle stores data in 5 nine bit words corresponding to the five energy channels. The first analysis cycle is suppressed and replaced by the sync cycle. The remaining 7 cycles are data gathering cycles which alternate between electron measurement and background measurement as described in the previous paragraph.

E. Data Transfer to the Spacecraft

The data gathered by the experiment is initially collected in a 13 bit scaler. This scaler transfers the data to a 13 bit shift register, the intermediate shift register (ISR), which changes the data from a 13 bit binary number to a 9 bit floating point number. The six low order bits of the 9 bit number constitute the mantissa, m, and the 3 high order bits constitute the floating point exponent n. The number N may be represented as

$$N = 2^n \cdot m$$

in floating point format. The ISR changes the 13 bit number

to a floating point by left shifting (i.e. shifting bits to higher order) a maximum of 7 times or until the highest order bit of the ISR is a one. The high order 6 bits in the ISR then become the mantissa m, and

$$n = 7 - \text{number of shifts.}$$

This number n m is then stored in the appropriate storage register for the given channel.

Data stored in these storage registers is read out by the spacecraft data system in serial form. The two data systems of the spacecraft are completely independent and both may be operating simultaneously and hence the readout logic of the experiment must either transmit data to only one data system at any given time or must contain two independently operating data output transfer systems. We chose the latter since this will give us greater redundancy and allow us to obtain the data both via the onboard tape recorder and via real time telemetry. The double data reception is useful in case the data from one mode of transmission is of poor quality. For this reason independent redundant output systems were designed for the experiment. The spacecraft supplies to the experiments "shift pulses" which command that one bit should be transferred to the spacecraft from some experiment. There are also supplied to the various experiments "inhibit pulses" which command that a specific word be transferred from experiment to spacecraft. The next nine "shift pulses" must then be used to transfer the word specified by the inhibit pulse to

the spacecraft. The spectrometer has five inhibit pulse lines coming from each of the two data systems of the spacecraft. Each of the five is identified with a given word which corresponds to a given channel.

When the inhibit pulse for a given word is received the contents of the storage register corresponding to that word is transferred into the output shift register (OSR) for that data system. Inhibit lockout is then imposed for the word of that data system such that data cannot be transferred from storage to the OSR of that data system again until lockout is removed by the accumulation of new data. Once the data has been transferred to the OSR, the "shift pulses" shift the data one bit at a time to the spacecraft data system. If data has not been transferred from storage due to inhibit lockout, zeroes are transferred from the OSR to the spacecraft, indicating an unsuccessful readout and no new data. All of the data gathered by the detector is biased by one such that a successful readout of zero data differs from an unsuccessful readout (e.g. zero data is transferred out as a one). The repetition rate of new data received is such that at least one complete readout attempt by the spacecraft is possible between data cycles. This constraint of at least one readout between successive analysis cycles determines the maximum repetition rate. We must have at least one complete readout between the end of one analysis cycle and the start of the succeeding cycle. Since there are 9 words

inclusive between the start and end of a complete readout (see section II-B) it takes

$$9 \times 9 \text{ bits} \times \frac{1}{1000 \text{ bits/sec}} = .081 \text{ sec}$$

for a complete readout. There are 128 x .009 = 1.152 seconds between successive readouts. Therefore there must be 1.152 + .081 = 1.233 seconds between the end and start of the analysis cycles. An analysis cycle requires .10 seconds and hence there must be at least 1.333 seconds between successive analysis cycles to ensure at least one readout at the lowest bit rate.

The storage registers are common to both of the data systems. Either or both OSR's may read out the storage registers since the readout is non-destructive. The OSR's are capable of transferring the data at either 1000 bits/sec, 8000 bits/sec or 64000 bits/sec. There is no cross talk or interconnection between the two OSR's and hence all possible combination of frequencies and phase shifts between the two readout systems is permissible.

The redundant readout mode has worked quite well and has provided us with full time coverage whenever either the tape recorder or the transmitter was turned on. Often the real time data was of questionable value due to transmission noise but the tape recorder data served as an effective backup.

The spacecraft also supplied the experiment with +28 volts of power. The 28 volt line can vary from 22 to 35 volts. This varying input power was regulated and transformed into the various voltages needed by the experiment.

All electronic circuits were designed and constructed at the University of Minnesota Physics Department electronics shop. The circuits were mounted on epoxy boards onto which silver stakes had been fastened for interconnections. These completed circuit boards were epoxied onto magnesium trays, one board on each side of the tray. This flat construction allowed one to easily modify and repair a circuit. Figure III-17 shows the assembled experiment and Figure III-18 shows one of the four trays containing the entrance slit, magnet, photomultiplier and high voltage power supply. The four trays onto which both the electronics and experiments were fastened were then bolted together to form the completed experiment. The magnesium trays which were cut from a block of magnesium were anodized using the "Dow 17" process to prevent the corrosion of the magnesium.

F. Environmental Tests

The completed experiment was subjected to numerous environmental tests after assembly and calibration. The first of these tests was a vibration test in which the experiment was subjected to sinusoidal accelerations and to random noise. No problems were ever encountered during this test with any of the six units. We had anticipated

Figure III-17

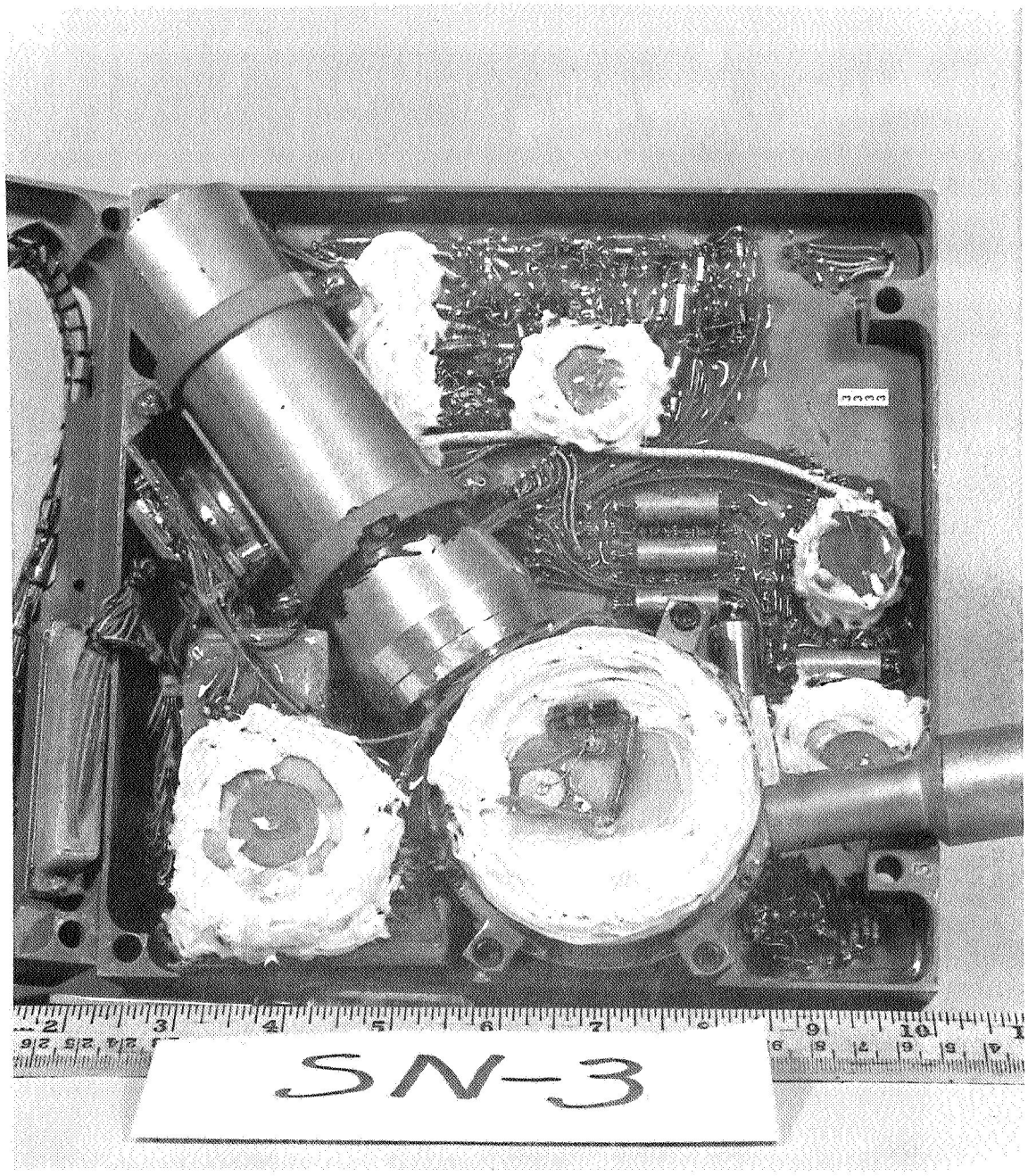

Figure III-18

some difficulty with the phototube; however, the tube was completely encapsulated in rubber and firmly fastened to the massive magnet which probably effectively dampened the vibrations. The gains and calibration of the units were the same before and after such vibration test.

The second environmental test was a thermal test. We required that the experiment function from -20°C to +50°C. The experiment was connected to a spacecraft simulator and all logical operations as well as the detector system were observed for proper operation at 10° intervals. The gain of the detector system remained stable, however, only from 0°C to 40°C. Outside of this interval the gain of the phototube began to change rapidly. The temperature limits set by GSFC for the experiment were +5°C to +35°C and hence the interval of stability was quite acceptable. During the operating life of the spacecrafts the temperature in the spacecrafts near the spectrometer remained at about 25° $\pm$ 2° C and hence the thermal calibrations are not used. The only major problem to arise during temperature testing was the repeated failure of Transitron type TMD 2017 diodes in the logic during temperature cycling. The differences in the coefficients of expansion of the diodes and the epoxy coating of the circuit boards caused the diodes to become an open circuit. All TMD 2017 diodes were replaced by Texas Instrument Corporation glass encapsulated diodes and the problem was solved.

The final environemental test was the thermal vacuum test. All electron calibrations had been made in vacuum and no difficulty was encountered during vacuum testing. During vacuum testing great care had to be exercised to prevent a high voltage corona. The experiment could not be turned on at intermediate pressures.

After all test and efficiency calibration were completed the experiment was shipped to the environmental test center at Goddard Space Flight Center where it underwent acceptance tests similar to the environmental tests performed in our laboratory. Again no difficulties arose during these tests.

G. Efficiency Calibration of the Spectrometer

The magnet-slit system and the crystal-photomultiplier system are calibrated independently and then the two results are folded together to give the overall efficiency. The magnet-slit system is calibrated using a Sr 90 source. The source is a disk source and is uniform and isotropic over the entrance slit of the magnet. The effective isotropic strength of the source, J_e, was determined by measuring the number of electrons, F, leaving a collimating slit and dividing by the geometry factor, G, of the slit

$$J_e = F/G \qquad \text{(III-12)}$$

The source was placed at the entrance slit of the magnet, and the magnet current was set to 500 milliamperes and a solid state detector was used to measure the distribution of the electrons passing through the magnet-slit system (see Figure III-19). The curve can be fitted quite well by a Gaussian, and since the Sr 90 spectrum is reasonably constant in the interval where the Gaussian is different from zero, we can say that this function is the transmissivity function for the magnet when the magnet current, I, is set to 500 milliamperes. We know that for our magnet the magnetic field $B \alpha I$ and, furthermore, that the rigidity $p \alpha B \alpha I$, and hence the spread in rigidities transmitted is $\Delta p = (c_u - c_\ell)\, I = \bar{c}\, I$. This means that the spread in rigidities is proportional to the current and hence the half width of

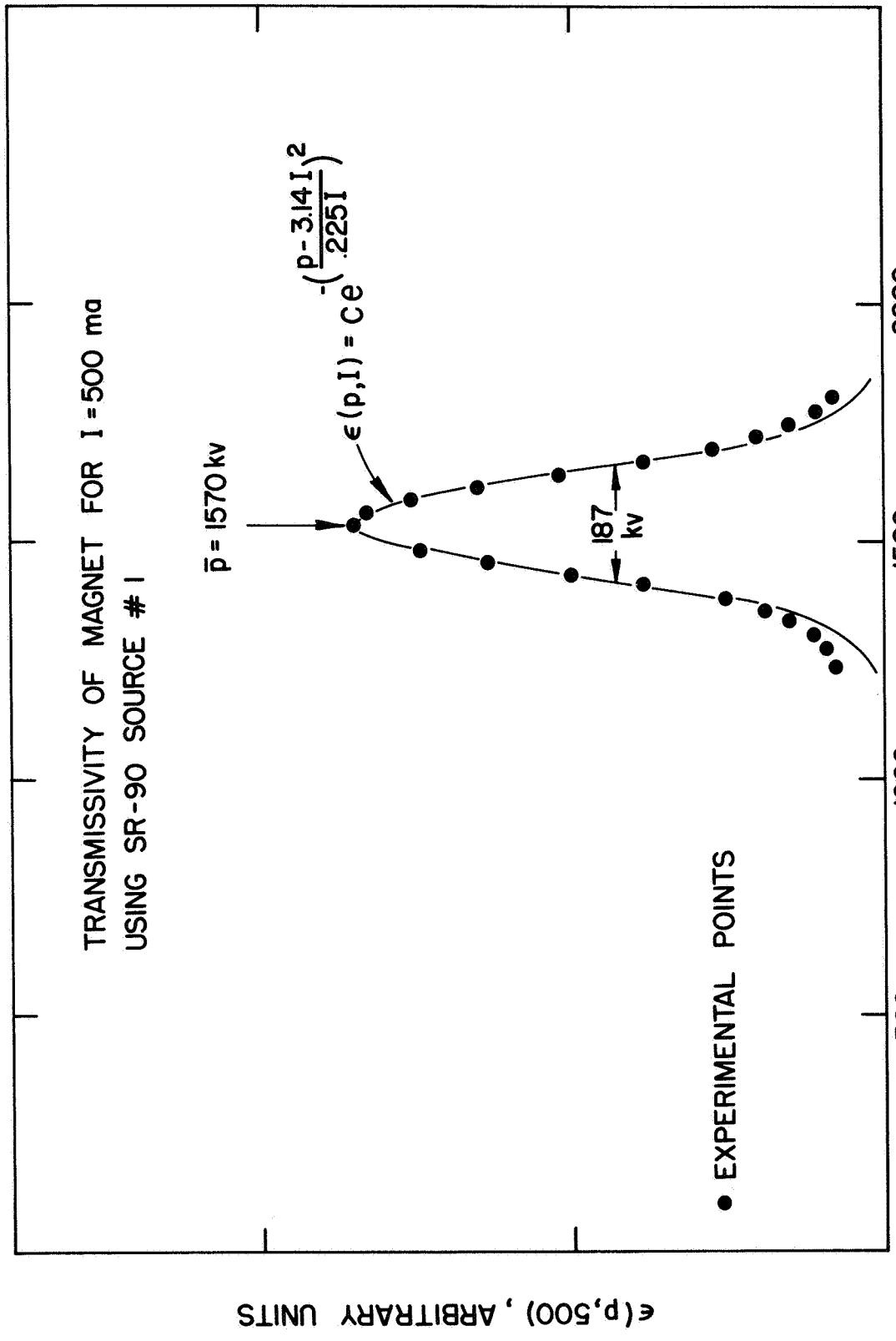

Figure III-19

the Gaussian distribution is a linear function of the current. Furthermore, the mean rigidity of particles transmitted $\bar{p} \alpha I$. Hence, we write for the efficiency for transmitting particles of momentum p at the magnet current I

$$\varepsilon\ (p,I) = A \exp\ (-(\frac{p-\bar{p}}{\sigma\ I})^2) = A \exp\ (-\ (\frac{p - 3.14\ I}{\sigma\ I})^2) \qquad \text{(III-13)}$$

Since the full width at half maximum for the Gaussian is 187 kv when I = 500 ma, σI = 112 kv when I = 500 ma and therefore we have

$$\sigma\ = .225 \text{ kv/ma} \qquad \text{(III-14)}$$

Therefore

$$\varepsilon\ (p,I) = A \exp\ (-(\frac{p - \bar{p}}{.225I})^2) = A \exp\ (-(\frac{p - 3.14\ I}{.225\ I})^2) \qquad \text{(III-15)}$$

The count rate, R(I), at the exit slit at a given magnet current I is

$$R(I) = \int_0^\infty \varepsilon\,(p,I)\ f\ (p)\ dp \qquad \text{(III-16)}$$

We may find the value of the constant A by performing the following integration

$$\int_0^\infty \frac{R(I)}{I}\ dI = \int_0^\infty \int_0^\infty \frac{\varepsilon\,(p,I)\,f\,(p)}{I}\ dp\ dI \qquad \text{(III-17)}$$

Since $\varepsilon(p,I)$ is a function which is strongly peaked and is different from zero only in the vicinity $p = \bar{p}$, we can move $f(p)$ outside the inner integral because $f(p)$, the spectrum of the calibration source, is a slowly varying function in the region where $\varepsilon(p,I)$ is different from zero. We let $f(p) = f(\bar{p})$ the value at the peak of the Gaussian. That is

$$\int_0^\infty \frac{R(I)}{I}\, dI = \int_0^\infty \frac{f(\bar{p})}{I} \int_0^\infty \varepsilon(p,I)\, dp\, dI \qquad \text{(III-18)}$$

$$= A \int_0^\infty \frac{f(\bar{p})}{I} \int_0^\infty \exp\left(-\left(\frac{p - 3.14I}{.225I}\right)^2\right) dp\, dI$$

If we let $x = p - 3.14\, I$ we have

$$\int_0^\infty \frac{R(I)}{I}\, dI = A \int_0^\infty \frac{f(\bar{p})}{I} \int_{-3.14\, I}^\infty \exp\left(-\left(\frac{x}{.225I}\right)^2\right) dx\, dI$$

$$\simeq A \int_0^\infty \frac{f(\bar{p})}{I} \int_{-\infty}^\infty \exp\left(-\left(\frac{x}{.225I}\right)^2\right) dx\, dI$$

$$= A \cdot (.225) \cdot \sqrt{\pi} \int_0^\infty f(\bar{p})\, dI$$

but since $\bar{p} = 3.14I$

$$\int_0^\infty \frac{R(I)}{I}\, dI = \frac{A \cdot (.225) \cdot \sqrt{\pi}}{3.14} \int_0^\infty f(\bar{p})\, d\bar{p} \qquad \text{(III-19)}$$

$\frac{R(I)}{I}$ is the count rate at the exit slit divided by the value of the magnet current and is easily measured by using the standard scintillation detector at the exit slit as a simple counter (counting everything above the noise level). $\frac{R(I)}{I}$ is plotted against I in Figure III-20 and a numerical integration of the function over all I gives the value 897.2 electrons/sec-ma. That is

$$\int_0^\infty \frac{R(I)}{I}\, dI = 897.2 \qquad \text{(III-20)}$$

The integral over f(p) is the total strength of the source at the entrance slit. In the above calibration one millicurie Sr 90 disk source was used (University of Minnesota source #1). Using a collimating slit having a geometrical factor $G = 8.64 \times 10^{-4}$ sterad-cm^2 and using equation III-12 we found that since F = 2012.0 counts/sec

$$J_e = \int_0^\infty f(\bar{p})\, d\bar{p} = 2.33 \times 10^6 \frac{\text{electrons}}{\text{cm}^2\text{-sterad-sec}} \qquad \text{(III-21)}$$

Substituting the values from equations III-20 and III-21 into equation III-19 we find that A = .000295 sterad-cm^2 and

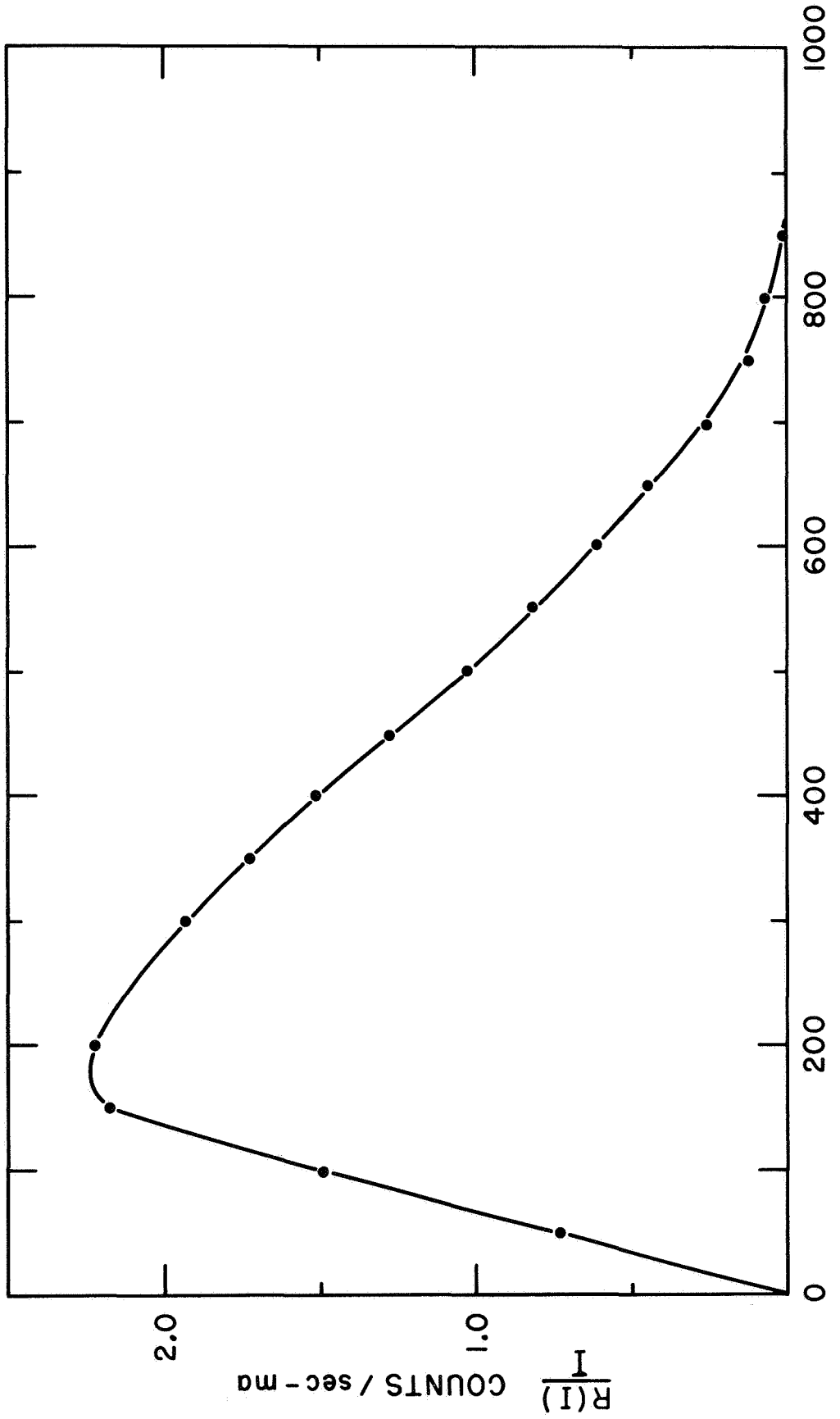

Figure III-20

therefore

$$\varepsilon(p,I) = .00295 \exp\left(-\left(\frac{p - 3.14I}{.225I}\right)^2\right) \qquad \text{(III-22)}$$

where p is in kv and I in milliamperes.

The response of the scintillation crystal photomultiplier system was measured using the electron accelerator between 50-100 Kev and monoenergetic electron sources at higher energies. The detector response is approximately Gaussian with a full width at half maximum that varies only slightly as a function of incident electron energy. At 100 Kev the width is 68 Kev (Figure III-12) whereas at 974 Kev (Bi-207 line) the full width is 110 Kev.

We let e(E,h) dh be the probability that an electron having an incident energy E will give a voltage pulse out of the detector assembly having an amplitude between h and h + dh. The function e(E,h) is written as

$$e(E,h) = \sqrt{\pi}\ \delta \exp\left(-\left(\frac{E - h}{\delta}\right)^2\right) \qquad \text{(III-23)}$$

where δ is determined from the full width and h is expressed in Kev such that the pulse amplitude corresponding to the center of the Gaussian equals the energy of the incident electron. We can then write

$$n(I) = \int_{h_1}^{h_2} \int_{o}^{\infty} f(E) \cdot \varepsilon(p,I) \cdot e(E,h)\, dp\, dh \qquad \text{(III-24)}$$

where $p = [(E + m_o c^2)^2 - m_o^2 c^4]^{1/2}$, $f(E)$

is the differential electron spectrum and $n(I)$ is the number of particles counted by the discriminator scalers when the magnet current is I and the discriminator edges are set at h_1 and h_2. The magnet current in the instrument, $I = I(t)$, is a function of time. The above integral (equation III-24) is then integrated over the time spent going through the analysis cycle for that channel and normalized for the spectrum of the source.

$$\bar{\varepsilon}_i = \frac{\int_{t_1}^{t_2} n(I(t))\, dt}{\int_{E_1}^{E_2} f(E)\, dE} \quad \frac{\text{counts}}{\text{data cycle}} \Big/ \frac{\text{electrons}}{\text{sterad-cm}^2\text{-sec}} \qquad \text{(III-25)}$$

$\bar{\varepsilon}_i$ is the effective efficiency for channel i for the complete detector system, t_1 and t_2 are the begin and end times of the analysis for channel i, and E_1 and E_2 are the lower and upper energy limits for channel i. The triple integral for $\bar{\varepsilon}_i$ is solved on a computer for various assumed spectra of incident electrons. Figure III-21 shows the results using power spectra $f(E) = E^{\gamma}$. This result is plotted against γ for the five energy channels.

The efficiencies of all channels except channel V are more or less independent of γ. Channel V is quite strongly dependent

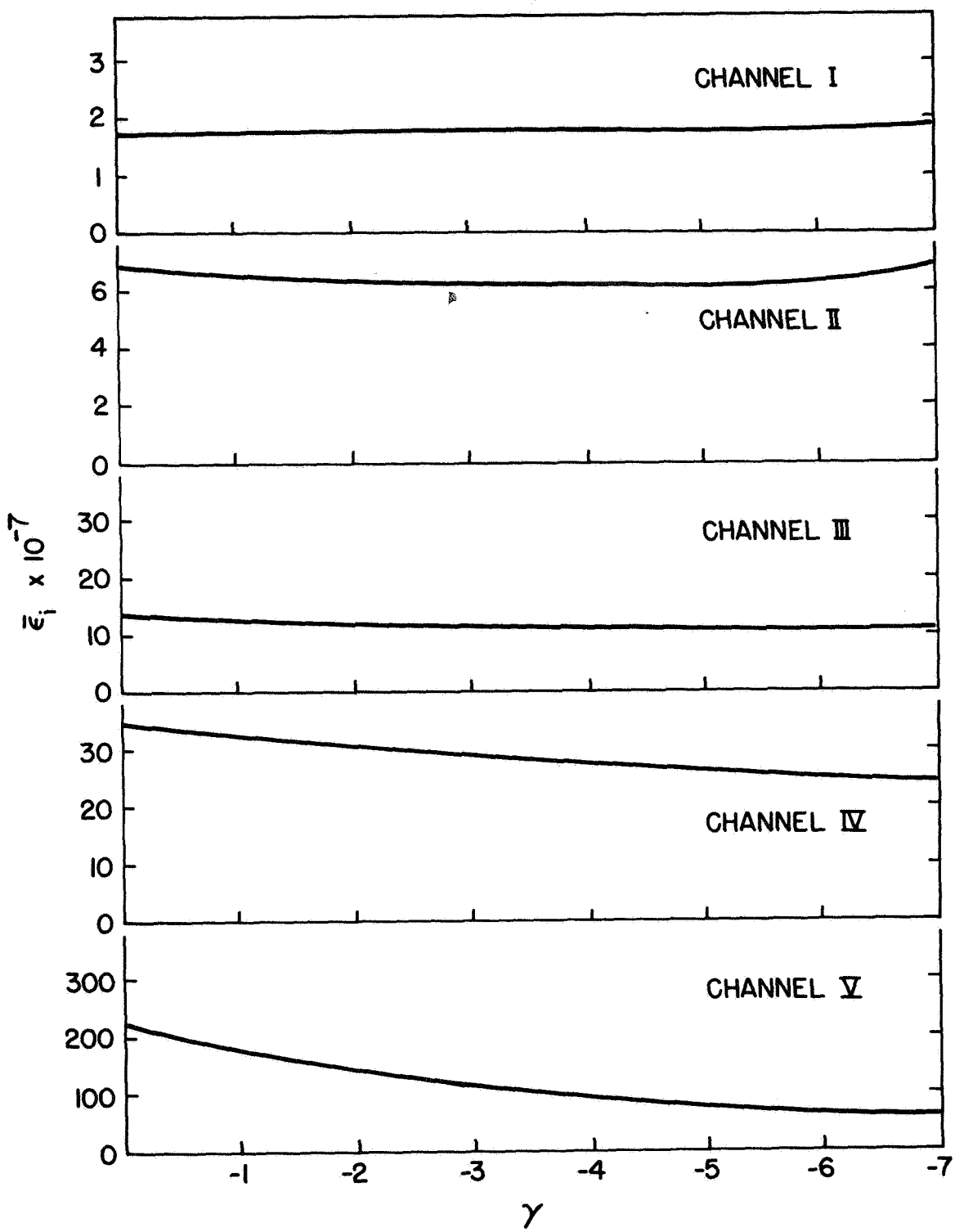

Figure III-21

on the spectrum because I(t) is very non-linear in Channel V since most of the time is spent at large values of I corresponding to the higher energies. Because of this spectral dependence an iteration process must be used to arrive at a satisfactory final spectrum. The differential directional flux for each channel is

$$\frac{dJ_i}{dE} = \frac{N_i}{\bar{\epsilon}_i \, \Delta E_i} \quad \frac{\text{electrons}}{\text{sterad-cm}^2\text{-sec-Kev}} \tag{III-26}$$

where N_i is the number of counts accumulated per second in channel i and ΔE_i is the energy interval covered by the channel.

The overall calibration of the spectrometer was checked using a 10 mc Sr 90 source. The Sr 90 source was placed over the entrance slit of the spectrometer and N_i the number of electrons per data cycle, was obtained. Using equation III-26, dJ/dE was found for each channel. These results are plotted in Figure III-22. On the same figure is the spectrum of the Sr 90 source as measured directly by a scintillation detector and pulse height analyzer. Only the lowest two spectrometer channels do not agree well, and these lie within the uncertainty in the spectrum of the calibrated source.

H. Intercalibration of the OGO-I and OGO-III Detectors

A derivation similar to the derivation described in the last section for OGO-I was used to obtain the calibration of the OGO-III detector. It was found that the two detectors are

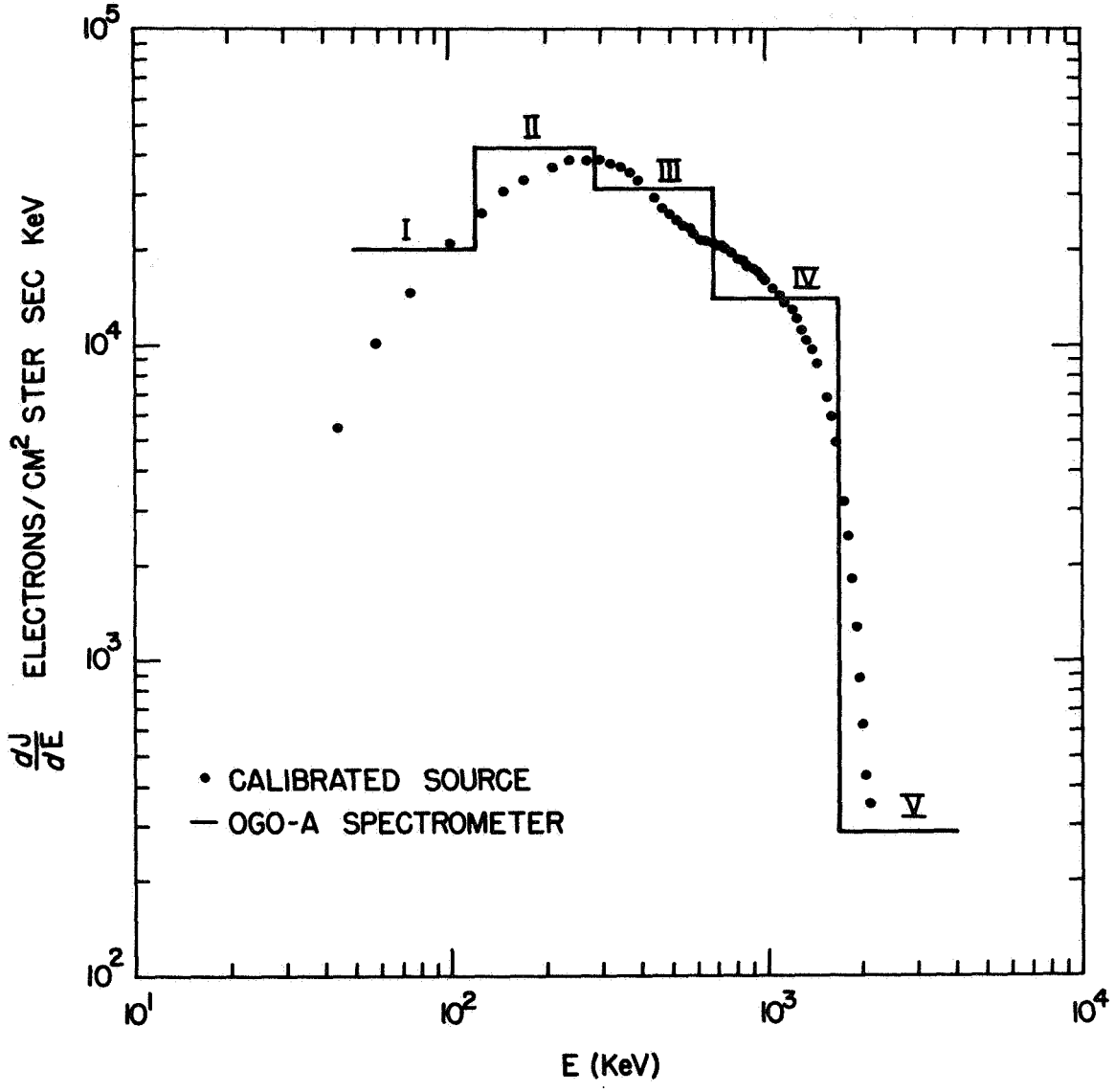

Figure III-22

almost identical and differ significantly only in the rate of change in the magnetic field of the analyzing magnet. The OGO-III magnet system has a magnetic field with a slower rise time due to a larger capacitance of the energy storage capacitor. Since the effective efficiency curves of the OGO-III detector differ from the OGO-I detector by only a multiplicative constant we can write the differential flux of the OGO spectrometer as

$$\frac{dJ_i}{dE} = \frac{N_i}{\delta_i \, \bar{\varepsilon}_i \, \Delta E_i} \qquad \text{(III-27)}$$

where δ_i, the intercalibration factor, is equal to one for OGO-I and has the values given in Table III-4 for OGO-III and where $\bar{\varepsilon}_i$ is the effective efficiency computed for OGO-I. That is, $\delta_i \, \bar{\varepsilon}_i$ is the effective efficiency of the OGO spectrometers. Using these effective efficiencies, the Sr 90 calibration check of Figure III-22 gives an agreement of better than 5% between the OGO-I and OGO-III detectors.

A further and more meaningful intercalibration could be made beginning in September 1966 when both instruments were operating simultaneously in space. If they do not agree in space then either one of the instruments had changed its calibration or the laboratory intercalibration with a Sr 90 source was not valid for the very steep energy spectra in space.

TABLE III-4

Spectrometer Calibration Constants

	δ_i	g_i	ΔE_i	$\bar{\epsilon}_i$	A_i
Channel #	OGO-III		(Kev)	($\gamma = -3$)	($\gamma = -3$)
I	1.56	10000	70	1.8×10^{-7}	7.9
II	1.65	1300	150	6.2×10^{-7}	8.4
III	1.35	290	400	1.2×10^{-6}	7.2
IV	1.18	36	1010	2.9×10^{-6}	9.5
V	1.12	2.4	2300	1.2×10^{-5}	15.4

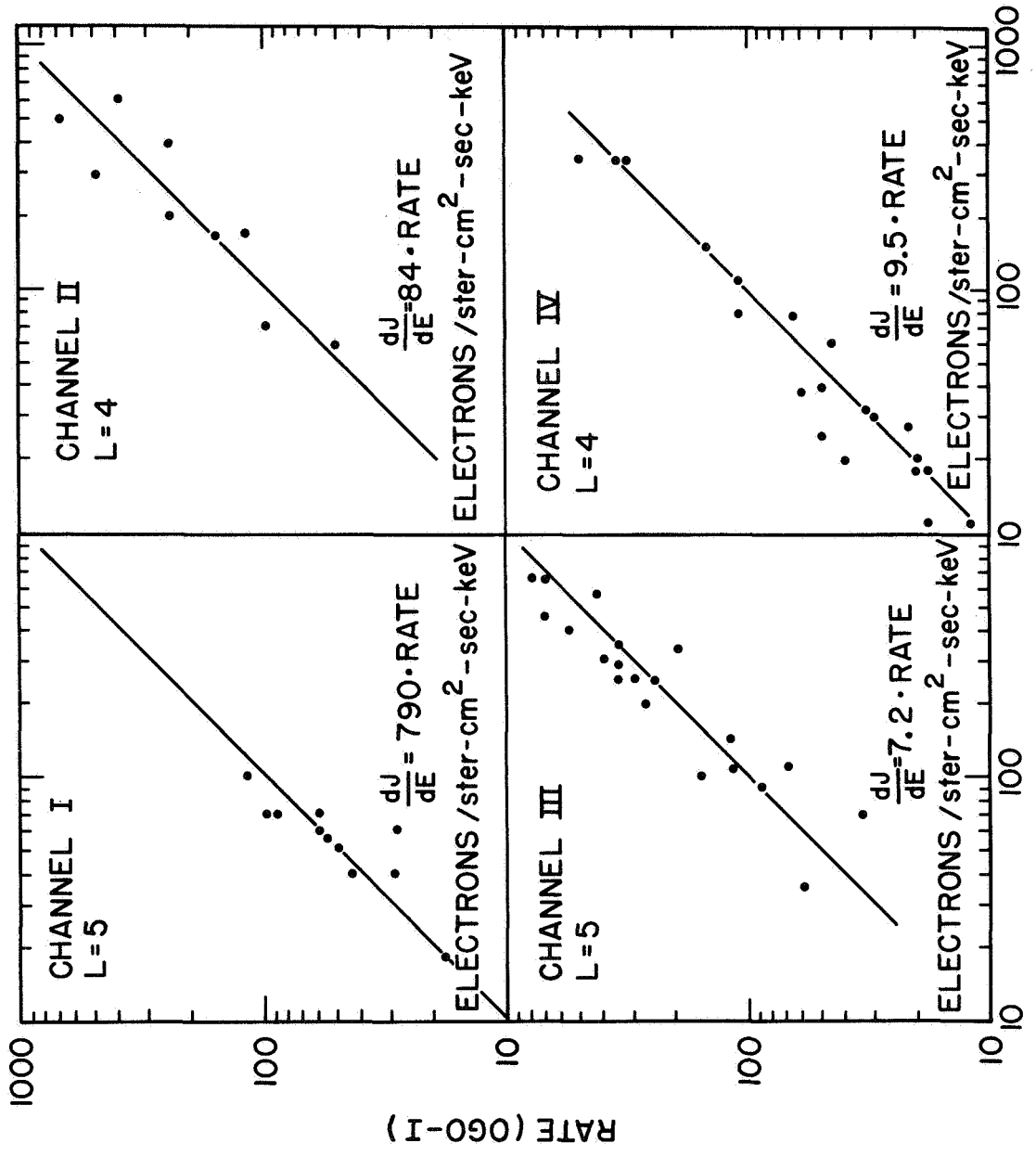

Figure III-23

A cross calibration check was performed using outer zone data from September 1966 to December 1966. Inner zone data was no longer available on OGO-I because of its very high perigee. Since the two instruments were never in identical positions at the same time and since the time changes are large and rapid in the outer zone, only the average correlation of the two instruments can be studied.

OGO-III data were plotted against time in the outer zone for L = 4 and L = 5 with each successive point connected to the previous point by a straight line. The OGO-III fluxes corresponding to the times when OGO-I data were available were then read from this straight line curve. The OGO-I fluxes are plotted versus the OGO-III fluxes in Figure III-23 for channels I, II, III and IV. Channel V, not shown, gives a similar result. Also shown on the figure are 45° lines representing perfect intercalibration. The scatter observed in Figure III-23 is a real scatter and not instrumental; it is due to the time variations and due to differences in pitch angle and local time. However, we note that the scatter of points is equally distributed on both sides of the curves. If the efficiency for detecting electrons in a given energy channel were to differ between the two instruments, then the points would fall to one side of the 45° line. Since there is, however, a large scatter in the points, an error in the intercalibration of less than 10% would not be observable. From Figure III-23 we conclude that the errors

in the intercalibration of the OGO-I and OGO-III spectrometers is no gerater than about 10%.

I. Data Reduction

The data transmissions from the spacecrafts are recorded on magnetic tapes at the various telemetry stations throughout the world. These tapes are shipped to the Digital Data Processing Center at Goddard Space Flight Center where the data from all of the experiments on the spacecraft is separated and a computer format tape is generated for each experimenter. The computer format tapes received by the University of Minnesota are processed at the University Computer Center on a Contral Data 1604 computer.

The number of counts accumulated in each of the five energy channels for every analysis cycle is contained on the computer tape. From these data tapes delivered to our center the total data counts and background counts are each averaged over some time interval Δt, during which there are C_D data cycles and C_B background cycles. C_D and C_B are not equal because every fourth background cycle is replaced by a synchronization cycle and because some cycles may not be used because of noise. If we let D_i and B_i be the total number of counts accumulated in channel i during C_D data and C_B background cycles, respectively, then

$$N_i = \frac{D_i}{C_D} - \frac{B_i}{C_B} \qquad \text{(III-28)}$$

where N_i now is the number of electrons counted per data cycle. The statistical error in N_i is

$$\Delta N_i = \sqrt{\left(\frac{\sqrt{D_i}}{C_D}\right)^2 + \left(\frac{\sqrt{B_i}}{C_B}\right)^2} \qquad \text{(III-29)}$$

The differential directional flux for each channel is then

$$\frac{dJ_i}{dE} = \frac{(N_i \pm \Delta N_i)}{\bar{\varepsilon}_i \delta_i \Delta E_i} \quad \text{electrons/cm}^2\text{-sterad-sec-Kev} \qquad \text{(III-30)}$$

All spectrometer data in the laboratory are represented in terms of an arbitrary scale which must be multiplied by a conversion factor A_i to obtain dJ_i/dE. The factor A_i which is a constant for each energy is chosen to be the same for OGO-I and OGO-III. If we let F_i be the arbitrary rate for channel i, then

$$F_i = \frac{g_i}{\delta_i} \quad N_i \qquad \text{(III-31)}$$

where g_i is the arbitrary normalization factor and δ_i is the intercalibration factor. From equation III-27 we have

$$\frac{dJ_i}{dE} = \frac{N_i}{\delta_i \, \bar{\varepsilon}_i \, \Delta E_i}$$

therefore we get

$$\frac{dJ_i}{dE} = F_i \cdot \frac{\delta_i}{g_i} \cdot \frac{1}{\delta_i \, \bar{\varepsilon}_i \, \Delta E_i}$$

$$= F_i \cdot \frac{1}{g_i \, \bar{\varepsilon}_i \, \Delta E_i}$$

$$= F_i \cdot A_i \qquad \text{(III-32)}$$

where

$$A_i = \frac{1}{g_i \, \bar{\varepsilon}_i \, \Delta E_i} \qquad \text{(III-33)}$$

The conversion factor A_i is spectrum dependent because $\bar{\varepsilon}_i$ is spectrum dependent. g_i is a constant for each channel. Table III-4 lists g_i, ΔE_i and A_i for a power spectrum having $\gamma = -3$. A_i may easily be calculated for other γ by obtaining $\bar{\varepsilon}_i$ from Figure III-21 and evaluating equation III-31.

A sample computer printout of 5 minute averages is shown in Table III-5. The printout specifies the time interval as well as the number of data and background samples in a given five minute average. The rows labeled TOTAL DATA and TOTAL BKGND correspond to $D_i \pm \sqrt{D_i}$ and $B_i \pm \sqrt{B_i}$ (the * in Table III-5 represents $\pm$). The rows labeled AVERAGE DATA and AVERAGE BKGND present the rate for the electron and background measurements respectively in terms of the arbitrary flux units. The row labeled NET COUNTS presents the arbitrary rate F. The data for the five energy channels is presented from left to right, the lowest energy channel in the left-most column.

TABLE III-5

01APR67 OGO-B PLAYBACK DECM 098 REEL 01 ID NO. BB-9268 FILE NO. 0 RECORD NO. 579 EG 2 1KB TAPE PAGE NO. 691

AVERAGES FOR SEP 8, 1966		FROM 6 10 0 TO 6 15 0		108 DATA PULSES		81 BACKGROUND PULSES			
TOTAL DATA	1140*	33.764	755*	27.477	849*	29.138	1475*	38.406	363*	19.053
TOTAL BKGND	564*	23.749	196*	14.000	158*	12.570	84*	9.165	6*	2.449
AVERAGE DATA	67555.556*	2000.823	5522.685*	200.991	1690.139*	58.005	417.917*	10.882	7.159*	.376
AVERAGE BKGND	44562.963*	1876.439	1911.605*	136.543	419.383*	33.364	31.733*	3.462	.158*	.064
NET COUNTS	22992.593*	2743.049	3611.080*	242.985	1270.756*	66.916	386.183*	11.419	7.001*	.381

AVERAGES FOR SEP 8, 1966		FROM 6 15 0 TO 6 20 0		112 DATA PULSES		84 BACKGROUND PULSES			
TOTAL DATA	1472*	38.367	680*	26.077	936*	30.594	1604*	40.050	476*	21.817
TOTAL BKGND	881*	29.682	285*	16.882	237*	15.395	111*	10.536	9*	3.000
AVERAGE DATA	84114.286*	2192.380	4796.429*	183.935	1796.786*	58.730	438.236*	10.942	9.053*	.415
AVERAGE BKGND	67123.810*	2261.459	2680.357*	158.771	606.607*	39.403	40.436*	3.838	.228*	.076
NET COUNTS	16990.476*	3149.718	2116.071*	242.982	1190.179*	70.723	397.800*	11.596	8.824*	.422

AVERAGES FOR SEP 8, 1966		FROM 6 20 0 TO 6 25 0		108 DATA PULSES		81 BACKGROUND PULSES			
TOTAL DATA	903*	30.050	550*	23.452	734*	27.092	1240*	35.214	317*	17.804
TOTAL BKGND	522*	22.847	178*	13.342	143*	11.958	70*	8.367	11*	3.317
AVERAGE DATA	53511.111*	1780.738	4023.148*	171.548	1461.204*	53.934	351.333*	9.977	6.252*	.351
AVERAGE BKGND	41244.444*	1805.220	1736.049*	130.122	379.568*	31.741	26.444*	3.161	.289*	.087
NET COUNTS	12266.667*	2535.715	2287.099*	215.315	1881.636*	42.581	324.889*	10.466	5.963*	.362

AVERAGES FOR SEP 8, 1966		FROM 6 25 0 TO 6 30 0		112 DATA PULSES		84 BACKGROUND PULSES			
TOTAL DATA	584*	24.166	418*	20.445	584*	24.166	948*	30.790	195*	13.964
TOTAL BKGND	327*	18.083	117*	10.817	114*	10.677	38*	6.164	5*	2.236
AVERAGE DATA	33371.429*	1380.920	2948.393*	144.211	1121.071*	46.390	259.007*	8.412	3.708*	.266
AVERAGE BKGND	24914.286*	1377.763	1100.357*	101.728	991.786*	27.328	13.843*	2.246	.127*	.057
NET COUNTS	8457.143*	1950.685	1848.036*	176.480	829.286*	53.841	245.164*	8.707	3.582*	.272

AVERAGES FOR SEP 8, 1966		FROM 6 30 0 TO 6 35 0		108 DATA PULSES		81 BACKGROUND PULSES			
TOTAL DATA	373*	19.313	344*	18.547	489*	22.113	696*	26.382	125*	11.180
TOTAL BKGND	181*	13.454	128*	11.314	85*	9.220	21*	4.583	7*	2.646
AVERAGE DATA	22103.704*	1144.486	2516.296*	135.670	973.472*	44.022	197.200*	7.475	2.465*	.221
AVERAGE BKGND	14301.235*	1063.002	1248.395*	110.344	225.617*	24.472	7.933*	1.731	.184*	.070
NET COUNTS	7802.469*	1561.993	1267.901*	174.877	747.855*	90.367	189.267*	7.673	2.281*	.231

AVERAGES FOR SEP 8, 1966		FROM 6 35 0 TO 6 40 0		108 DATA PULSES		81 BACKGROUND PULSES			
TOTAL DATA	276*	16.613	255*	15.969	425*	20.616	613*	24.759	85*	9.220
TOTAL BKGND	144*	12.000	94*	9.695	61*	7.810	12*	3.464	4*	2.000
AVERAGE DATA	16355.556*	984.489	1865.278*	116.808	846.065*	41.040	173.683*	7.015	1.676*	.182
AVERAGE BKGND	11377.778*	948.148	916.790*	94.560	161.914*	20.731	4.533*	1.309	.105*	.053
NET COUNTS	4977.778*	1366.822	948.488*	150.285	684.151*	45.979	169.150*	7.136	1.571*	.189

AVERAGES FOR SEP 8, 1966		FROM 6 40 0 TO 6 45 0		112 DATA PULSES		84 BACKGROUND PULSES			
TOTAL DATA	223*	14.933	252*	15.875	495*	20.125	507*	22.517	67*	8.185
TOTAL BKGND	102*	10.100	60*	7.746	52*	7.211	16*	4.000	10*	3.162
AVERAGE DATA	12742.857*	853.325	1777.500*	111.972	777.455*	38.632	138.520*	6.152	1.274*	.156
AVERAGE BKGND	7771.429*	769.486	564.286*	72.849	133.095*	18.457	5.829*	1.457	.254*	.080
NET COUNTS	4971.429*	1149.031	1213.214*	133.584	644.360*	42.815	132.691*	6.322	1.021*	.175

AVERAGES FOR SEP 8, 1966		FROM 6 45 0 TO 6 50 0		108 DATA PULSES		81 BACKGROUND PULSES			
TOTAL DATA	212*	14.560	214*	14.629	341*	18.466	371*	19.261	43*	6.557
TOTAL BKGND	56*	7.483	29*	5.385	35*	5.916	15*	3.873	5*	2.236
AVERAGE DATA	12562.963*	862.828	1565.370*	107.007	678.843*	36.761	105.117*	5.457	.848*	.129
AVERAGE BKGND	4424.691*	591.274	282.840*	52.522	92.901*	15.703	5.667*	1.463	.131*	.059
NET COUNTS	8138.272*	1045.981	1282.531*	119.201	585.941*	39.975	99.450*	5.650	.717*	.142

All of the data was also machine plotted by a Calcomp 165 plotter against time, range and L (magnetic parameter). The L plots are the most frequently used plots for study of radiation belt phenomena. Figure III-24 is a sample of two computer generated L plots showing the five energy channels plotted with their statistical error bars. Virtually all of the analyses described in the next chapter use these plots as the starting point of the analysis.

The differential directional flux of electrons for the five energy channels may be obtained directly from Figure III-24 by substituting the value of the arbitrary rate F into equation III-32. For example, at L = 3.4 on September 8, 1966 for channel IV we find $F = 4 \times 10^2$. Using equation III-32 with $A_i = A_4 = 9.5$ from Table III-4 we find $\frac{dJ}{dE} = 38.0 \times 10^2$ electrons-cm^{-2}-sec^{-1}-ster^{-1}-Kev^{-1}. The lower of the two L plots (September 8, 1966) shows the flux of electrons in the radiation belts following a large magnetic storm which injected electrons deep into the radiation belts. The upper plot (June 25, 1966) was obtained during a somewhat less disturbed time and indicates the quiet-time configuration of the radiation belts. During quiet times a "slot" at L = 3.0 can be observed at all electron energies; this "slot" is obliterated following the large magnetic storm. One can see the very large increases due to the magnetic storm in all of the energy ranges; the increases are especially pronounced for electrons with energy greater than 690 Kev. Whenever the

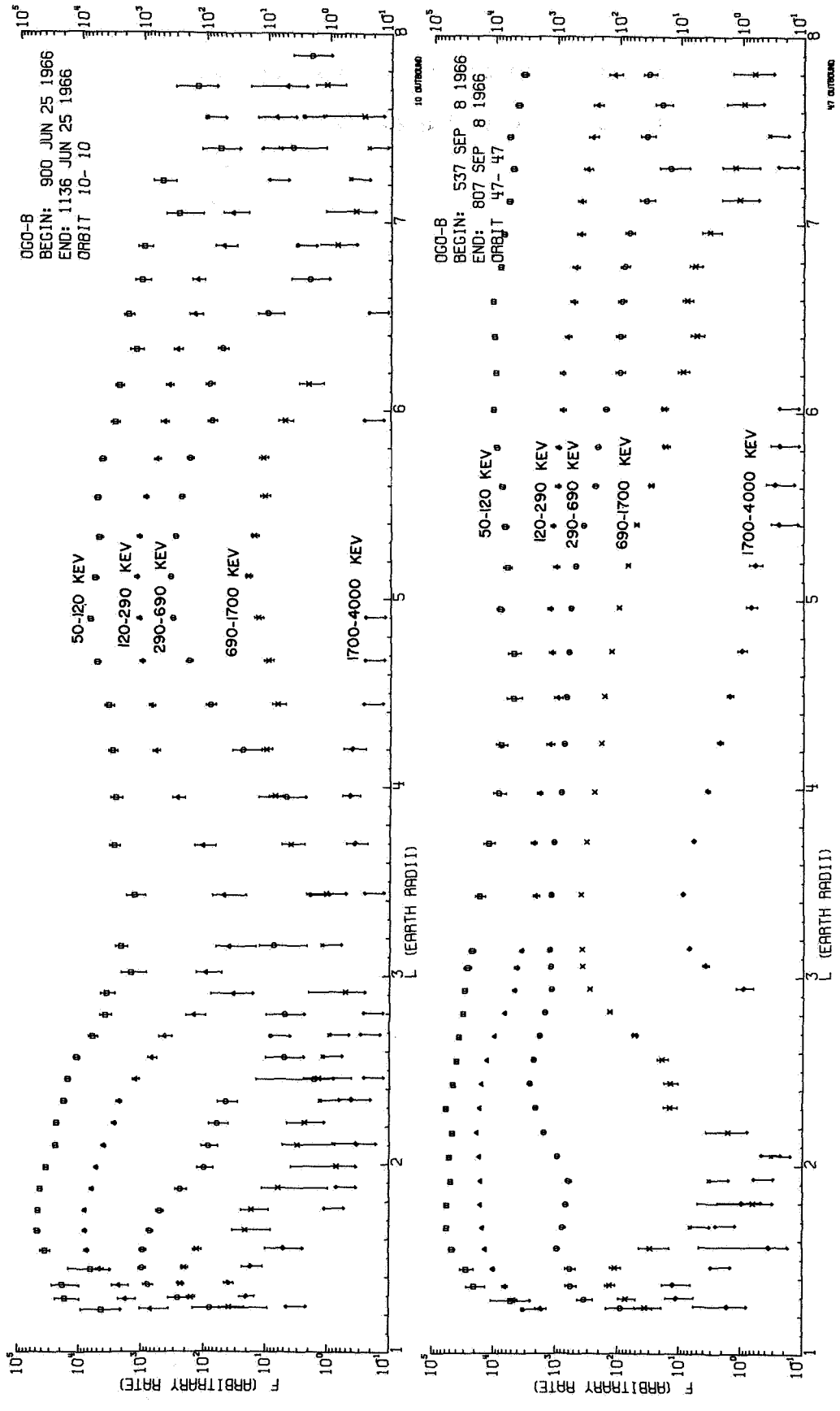

Figure III-24

fluxes drop below threshold as in the slot during quiet times, the computer plot indicates the upper limit.

IV. Presentation of the Data

A. Coordinate System

All data obtained by the satellite are a function of position, orientation and time. Six variables are necessary to describe these parameters; however, symmetries and special properties of the earth's dipole field reduce to three the number of variables necessary to describe a measurement. McIlwain (1961) introduced the B, L coordinate system where L is a parameter which defines a magnetic shell on which a particle is trapped and B is the magnetic field value defining the mirror point field of the particle. We will let B_T stand for the turning point field. B_T, L and t (time) completely describe a given measurement in the inner zone.

The spectrometer measures the flux of particles on some L shell where the entrance slit makes an angle α with the magnetic field which has a value B at that point. From the first adiabatic invarient we have that a particle making an angle α at field value B makes an angle α_o where the field value is B_o, where B_o is the equatorial value of the magnetic field and α_o will be referred to as the equatorial pitch angle. From the first adiabatic invarient we have

$$\frac{\sin^2\alpha_o}{\sin^2\alpha} = \frac{B_o}{B} \qquad \text{(IV-1)}$$

$$\alpha_o = \sin^{-1}\left\{\left[\frac{\sin^2\alpha}{B/B_o}\right]^{1/2}\right\}$$

Since the angle at the turning point is 90°

$$\alpha_o = \sin^{-1} \left\{ \left[\frac{B_o}{B_T} \right]^{1/2} \right\} \qquad \text{(IV-2)}$$

B_o is defined by the McIlwain program as

$$B_o = \frac{L^3}{31165.3} \quad \text{gauss}$$

and is a constant for a given shell. α_o and B_T are related by equation IV-2 and can be used interchangibly. We will prefer to use α_o, the equatorial pitch angle.

Using Louiville's theorem that the particle density in phase space is constant we have that

$$J(\alpha, B, L, t) = J(\alpha_o, B_o, L, t) = J(\alpha_o, L, t)$$

That is, the directional flux, J, at a time t on the magnetic shell L measured on the shell at position B with a look angle of α is the same as a measurement at B_o with a look angle of α_o. Therefore, any measurement made at some place on the shell can be reduced to a measurement at the equator. All data presented in this section will be expressed in terms of L, α_o and t.

An ephemeris tape supplied by Goddard Space Flight Center supplies us with the parameters necessary to calculate L and α_o. L is directly supplied on the tape and has been calculated using the 1960 Jensen and Cain 48 term expansion of the magnetic field. Other parameters supplied on the ephemeris tape which are necessary to calculate α_o are:

1. B/B_o the ratio of the field at the observation point

to the field at the equator.

2. $\vec{B}$ a unit vector describing the direction of the field in celestial coordinates.
3. $\vec{B}_B$ a unit vector describing the field in the coordinate system of the spacecraft (only valid for the stabilized spacecraft).

In order to calculate α we need only know the direction of the acceptance cone of the spectrometer. There are two distinct operating modes of the OGO spacecrafts, the stabilized mode and the spinning mode. These two cases must be treated independently.

Case 1. The stabilized spacecraft.

The OGO-III spacecraft was stabilized from launch until July 23, 1966. At that time a failure in the attitude control system caused the spacecraft to enter the spinning mode. From equation II-1 we have that $\vec{L}_B = -.174\ \hat{j}_B - .985\ \hat{k}_B$ where $\vec{L}_B$ is the look direction in terms of the spacecraft oriented coordinate system. Since we know $\vec{B}_B$ from the orbital ephemeris tapes we have that

$$\cos \alpha = \vec{L}_B \cdot \vec{B}_B$$

$$\alpha_o = \sin^{-1} \sqrt{\frac{1 - (\vec{L}_B \cdot \vec{B}_B)^2}{B/B_o}}$$

Case 2. The spinning spacecraft.

Except for the first 1-1/2 months of OGO-III's operating period, the OGO-I and OGO-III spacecraft have operated in a spinning mode. Both satellites spin about their Z body axis. The maximum angle between the spin and the Z axis is on the order of a degree or two. The spin axis $\vec{S}(t)$ is known at any given time. $\vec{S}(t)$ is a slowly varying function of time except during periods of re-orientation when the spin axis changes discontinuously. By slowly varying we mean that the direction of the spin axis in celestial coordinates changes on the order of a degree or so per week. See Table IV-1 for a time history of the spin axis of OGO's I and III. Since the spin axis changes so slowly we assume that it is not a function of time when we calculate the α of a given point.

The look direction of the spectrometer makes a 10° angle with the spin axis (see Figure II-2), and therefore the acceptance cone nutates about the spin axis. Some attitude information is available for OGO-I which would allow us to find the exact look direction as a function of time. This attitude information is, however, quite limited in accuracy and in availability. It is, furthermore, not yet available for OGO-III. Therefore, no attempt has yet been made to use this attitude information; instead we have taken the spin axis as the average look axis. We have taken averaging intervals long enough such that several

TABLE IV-1

Spin Axis Orientation of OGO-I and OGO-III

OGO-I

Right Ascension 44° Declination -9°

OGO-III

Reorientation Date	Right Ascension	Declination
July 27, 1966	47°	-25°
December 18, 1966*	47°	-18°
December 18, 1966	86°	8°
February 25, 1967*	86°	8°
February 25, 1967	202°	-3°
March 25, 1967*	202°	-3°
March 25, 1967	194°	0°
April 25, 1967*	194°	0°
April 25, 1967	186°	4°
May 23, 1967*	178°	7°
May 23, 1967	280°	-75°
June 30, 1967*	257°	-63°
June 30, 1967	312°	-37°
September 9, 1967*	312°	-30°
September 9, 1967	52°	-21°
December 5, 1967*	50°	-19°
December 5, 1967	83°	-13°

* Represents the right ascension and declination prior to reorientation. The other values are taken after completion of the reorientation procedure. There is a slight gravity gradient drift which modifies the look direction between successive reorientations.

spin periods are included in the average. The effect of averaging over the nutating acceptance cone is to essentially change the acceptance cone from a 15° cone to a 35° cone. The average look direction α is

$$\cos \alpha = \vec{S} \cdot \vec{B}$$

$$\therefore \quad \alpha_o = \sin^{-1} \sqrt{\frac{1 - (\vec{S} \cdot \vec{B})^2}{B/B_o}}$$

B. Long Term Time Variations of the Inner Zone

OGO-I was launched at a rather unique time near solar minimum and therefore a large volume of data is available in the inner zone which is quite free from external disturbances. During late 1964 and early 1965 we found no sudden changes in the inner zone below $L = 2.6$. Only slow monotonic changes were observed. Inside $L = 2.0$ no sudden externally caused changes were seen by OGO-I or OGO-III before September 2, 1966.

In studying the time dependence of the inner zone we must remember that all of the data in the inner zone is not only a function of time but also a function of L and α_o. We can, for example, fix L and accept all points whose α_o is between $\alpha_o + \Delta\alpha_o$ and $\alpha_o - \Delta\alpha_o$. The dependence on α_o in the inner zone is quite strong and hence $\Delta\alpha_o$ must be made small which reduces the number of data points available. Since OGO-I completes three orbits in eight days and since a given L shell is crossed twice on a given orbit, only six L crossings are

available in the inner zone at a given L every eight days, and because of the fixed look direction only one data value is obtained per L crossing. By further limiting the number of data points to the interval $\alpha_o \pm \Delta\alpha_o$, the number of data points becomes too small to provide a useful time study.

Therefore, we must first study the α_o dependence by fixing t. Since the time changes during 1964 and 1965 are relatively slow we may choose a relatively large time interval. We chose a time interval of two to three months which allowed us to obtain a rather comprehensive analysis of the pitch angle distributions. Three such analyses were performed, one during September-December, 1964, one during January-April, 1965 and one during June-August, 1966. In each case rather distinctive dJ/dE vs. α_o curves were obtained for all energy channels. Figure IV-1 through IV-5 is a set of such dJ/dE vs. α_o curves for the five energy channels for various L's. On these graphs is also marked the theoretical loss cone as determined from calculations using the 64 term expansion of the earth's field and assuming a 200 km mirror altitude. A program obtained from Dr. Carl McIlwain was used to calculate the L's and B/B_o for the various mirror points. Since the pitch angle at the mirror point is 90°, the α_o of the loss cone is

$$\alpha_o = \sin^{-1} \sqrt{B_o/B}$$

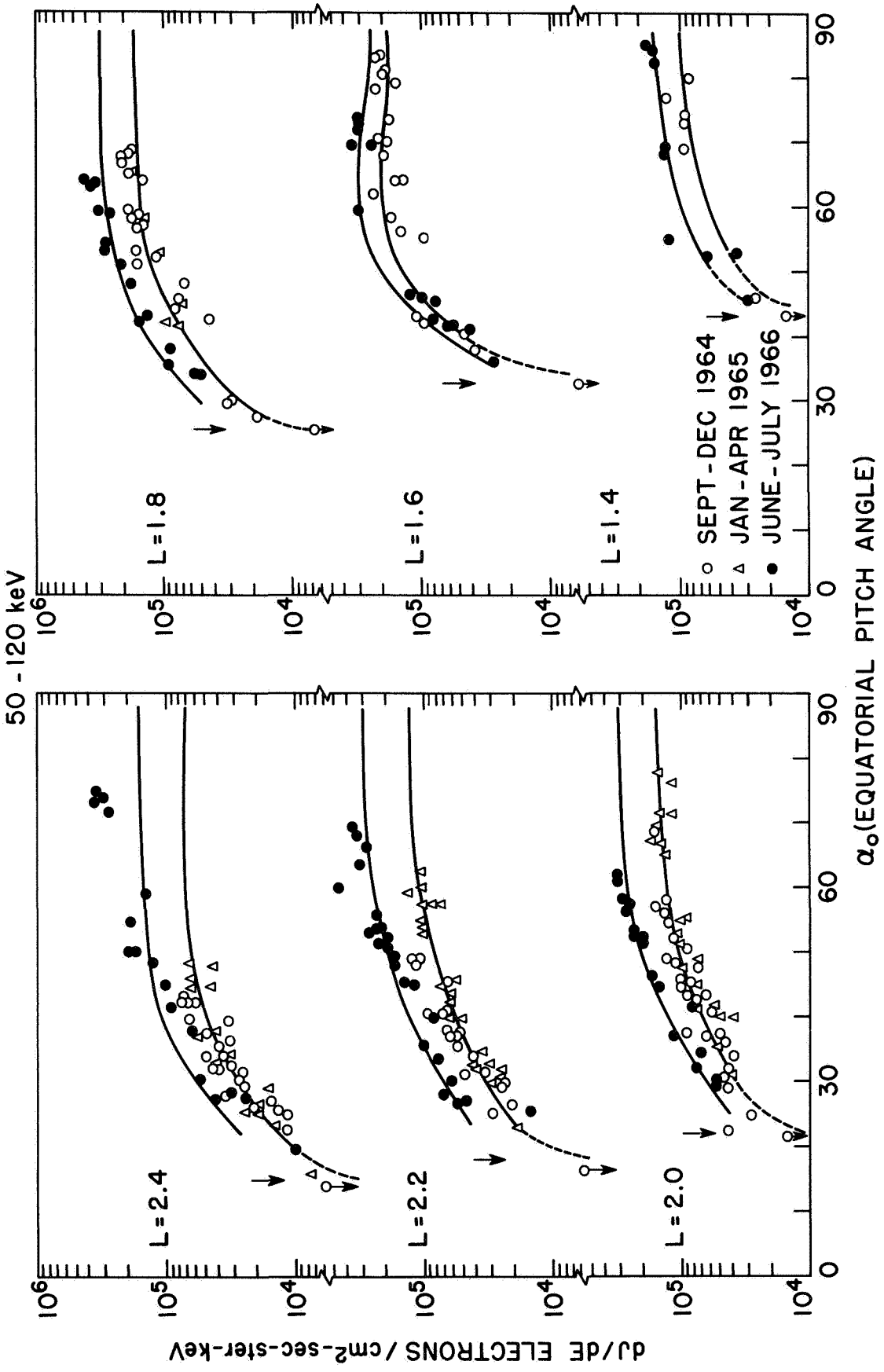
50 - 120 keV
dJ/dE ELECTRONS / cm2-sec-ster-kev
α_o(EQUATORIAL PITCH ANGLE)
L = 1.8
L = 1.6
L = 1.4
L = 2.4
L = 2.2
L = 2.0
SEPT-DEC 1964
JAN-APR 1965
JUNE-JULY 1966

Figure IV-1

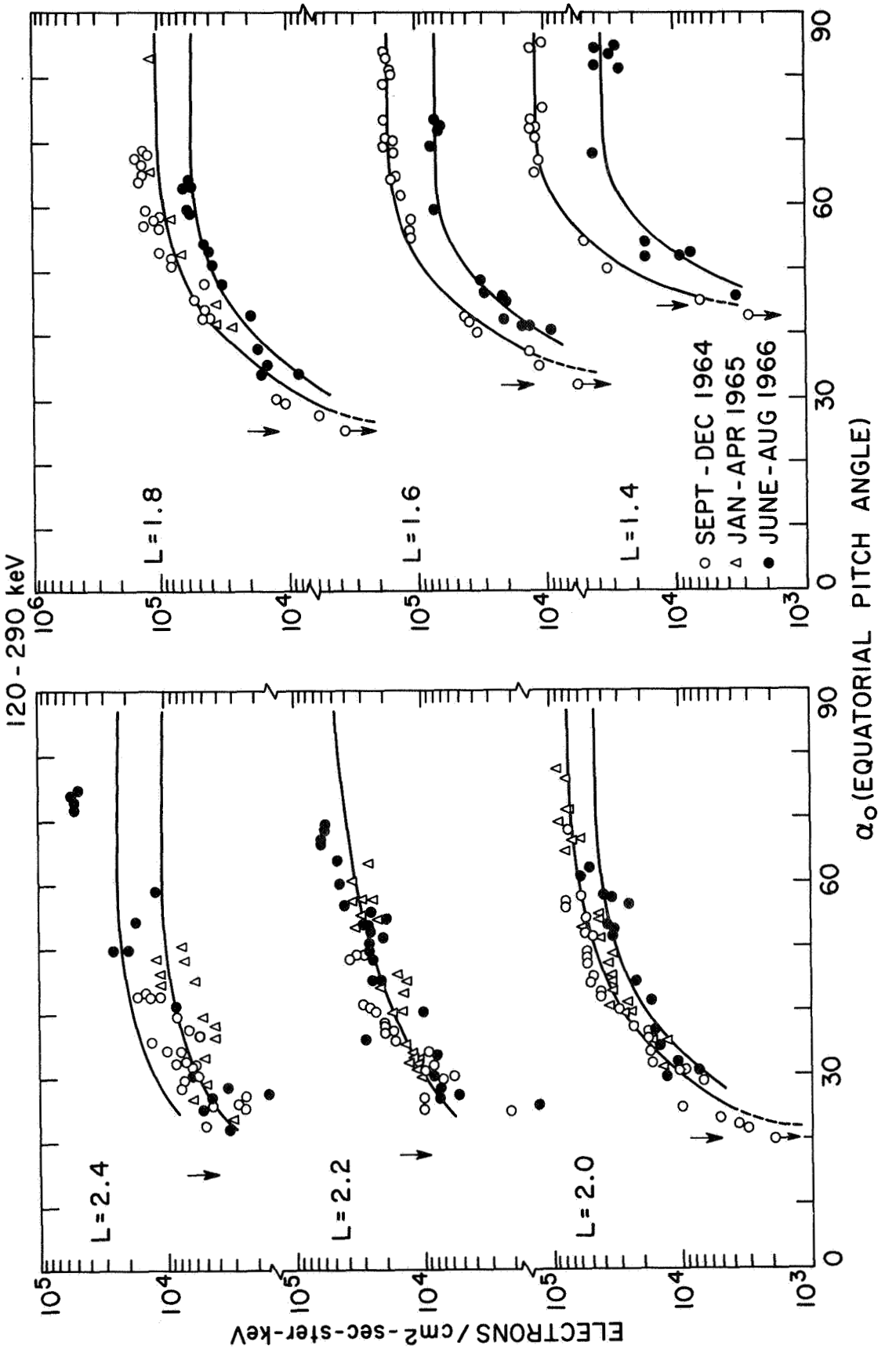
120 - 290 keV
ELECTRONS / cm2 - sec - ster - keV
α_o (EQUATORIAL PITCH ANGLE)
L = 2.4
L = 2.2
L = 2.0
L = 1.8
L = 1.6
L = 1.4
○ SEPT - DEC 1964
△ JAN - APR 1965
● JUNE - AUG 1966

Figure IV-2

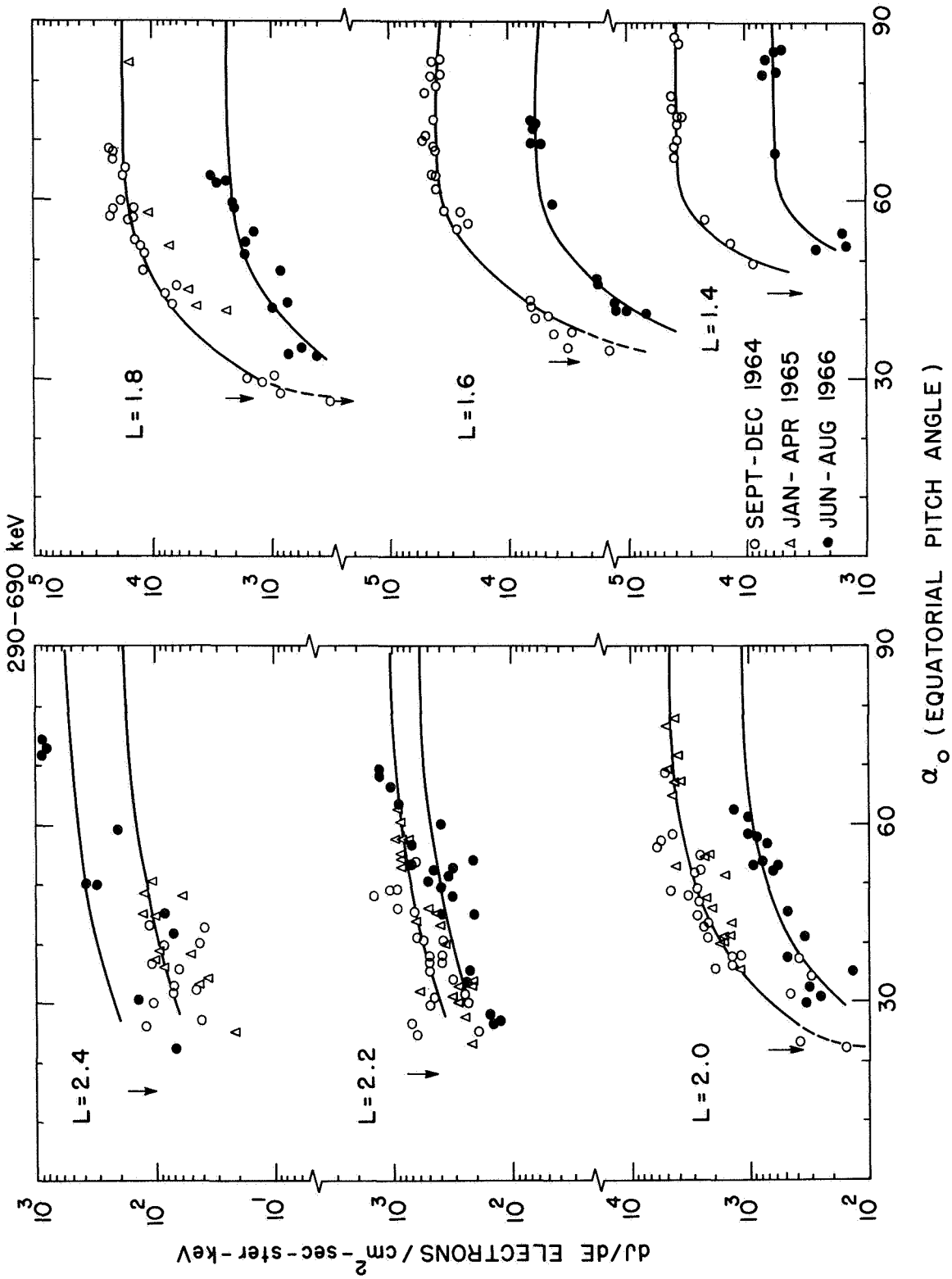
290-690 keV
dJ/dE ELECTRONS / cm²-sec-ster-keV
α₀ (EQUATORIAL PITCH ANGLE)
L=1.8
L=1.6
L=1.4
L=2.4
L=2.2
L=2.0
SEPT-DEC 1964
JAN-APR 1965
JUN-AUG 1966

Figure IV-3

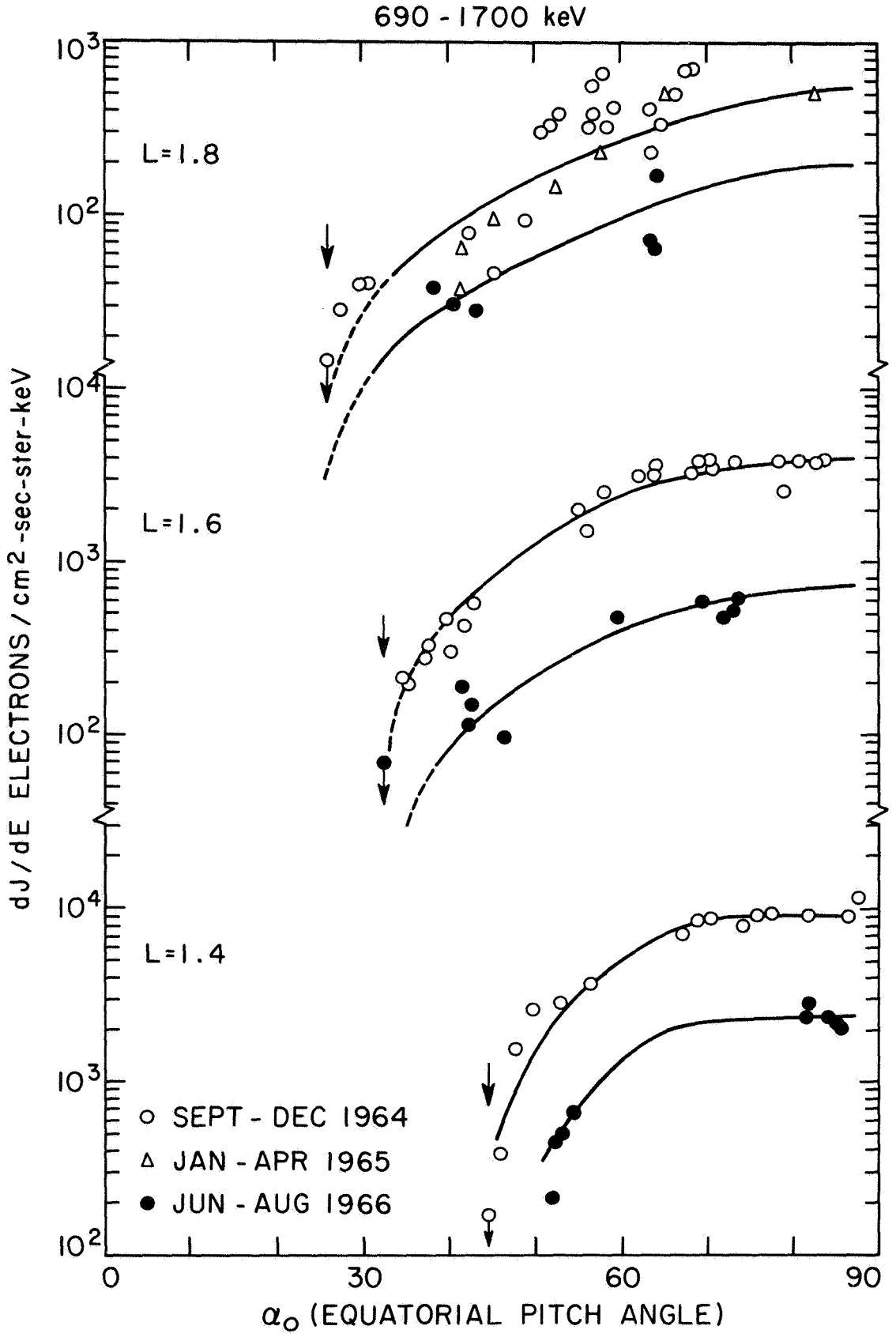
690 - 1700 keV
L=1.8
L=1.6
L=1.4
SEPT - DEC 1964
JAN - APR 1965
JUN - AUG 1966
dJ/dE ELECTRONS/cm2-sec-ster-keV
α_o (EQUATORIAL PITCH ANGLE)
0
30
60
90

Figure IV-4

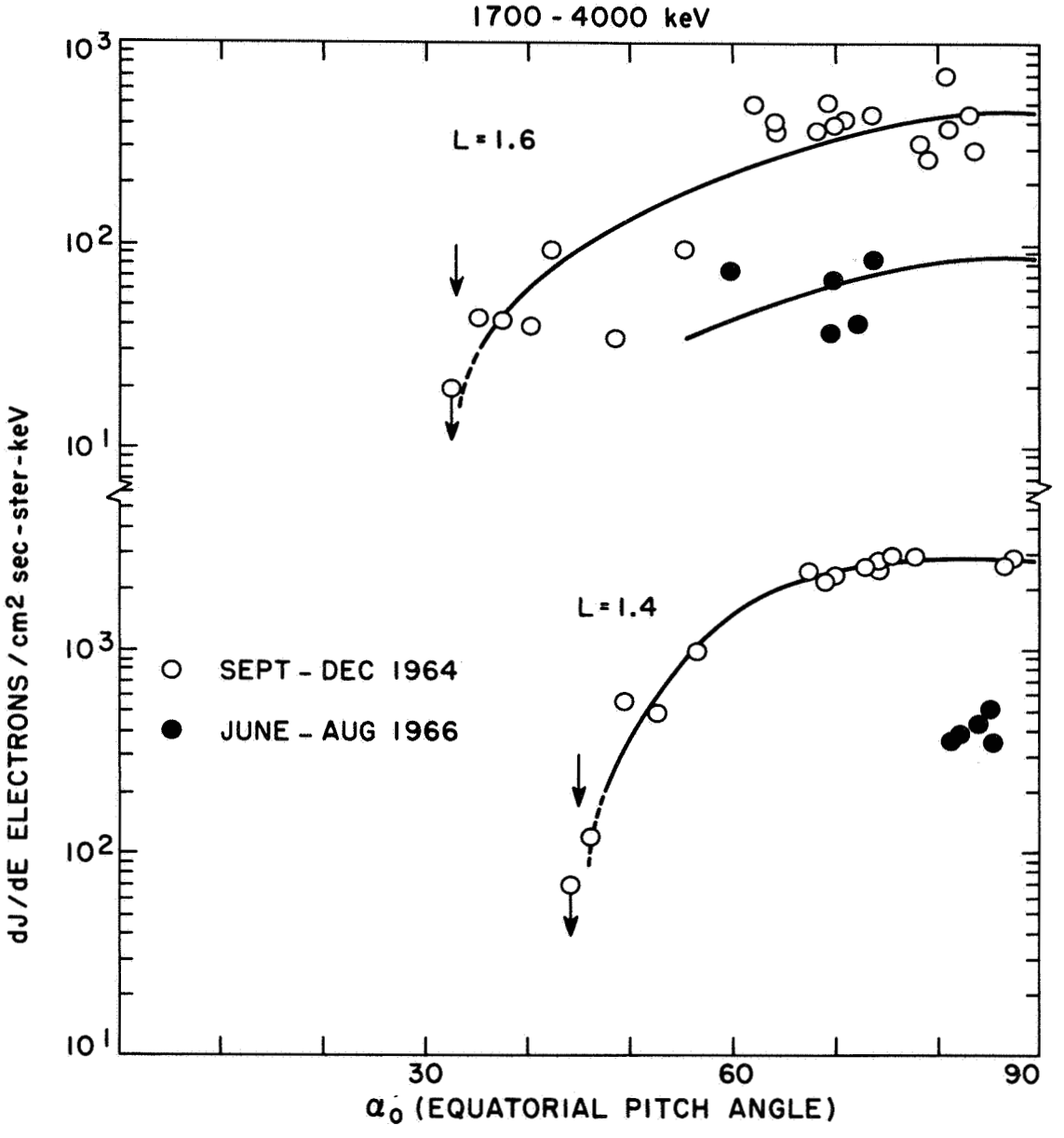
1700 - 4000 keV
L = 1.6
L = 1.4
SEPT - DEC 1964
JUNE - AUG 1966
dJ/dE ELECTRONS / cm2 sec - ster - keV
α_0 (EQUATORIAL PITCH ANGLE)
10^3
10^2
10^1
30
60
90

Figure IV-5

One of the first interesting things to note on Figures IV-1 to IV-5 is the smoothness of the curves, especially for the smaller L's. For larger L's there are larger statistical uncertainties plus perhaps some small short-term time variations. Since all the data points during a given 3 month time period fall on a reasonably well defined curve the time changes during the two month interval are small. All of the curves exhibit a rather similar form. The curves are flat near $\alpha_o = 90°$ dropping off as one proceeds toward the loss cone and then cutting off very sharply near the theoretical loss cone. It should also be noted that at a given L for a given energy channel the three sets of curves covering three different periods of time all have approximately the same shape even though the amplitudes may be different. The constant shape of the curves may be utilized in separating the t and α_o dependence of the fluxes. If we let $R_i(\alpha_o,t)$ be the rate of channel i at α_o at time t we may write it as

$$R_i(\alpha_c,t) = R_i(\alpha_o) \cdot \eta_i(t)$$

To enable us to do a complete time study least square functions were fitted to the September-December, 1964 dJ/dE vs. α_o curves. These curves are symmetric about $\alpha_o = 90°$ and have a roughly parabolic shape on log paper and hence the following functions were used to approximate the data. If we let $g(\alpha_o)$ be the least square functions then we have

$$R_i(\alpha_o) \simeq g_i(\alpha_o) = 10^{\sum_{j=o}^{N} a_j (90 - \alpha_o)^{2j}}$$

where N, the degree of the polynomial, is determined by the closeness of the fit desired, which depended on the scatter of the data points describing the curve as well as on the number of data points available. The solid lines drawn through the 1964 points in Figures IV-1 to IV-5 are the least square fit curves. These same curves are multiplied by a constant and are also fitted through the 1966 data. One can see that the fit is excellent during both time periods. Usually either 2, 4 or 6th degree polynomials were used to obtain the curves. So we may write

$$R_i(\alpha_o,t) \simeq g_i(\alpha_o) \cdot \eta_i(t)$$

$$R_i(90,t) \simeq g_i(90) \cdot \eta_i(t)$$

but

$$R_i(\alpha_o,t) = R_i(\alpha_o) \cdot \eta_i(t)$$

$$\eta_i(t) = \frac{R_i(\alpha_o,t)}{R_i(\alpha_o)}$$

$$\simeq \frac{R_i(\alpha_o,t)}{g_i(\alpha_o)}$$

$$\therefore R_i(90,t) \simeq \frac{g_i(90)}{g_i(\alpha_o)} \cdot R_i(\alpha_o,t)$$

That is, we may remove the pitch angle dependence of the data and reduce all of the data to $\alpha_o = 90°$ or to any other angle. We chose to normalize the data to $\alpha_o = 90°$. The measured data $R_i(\alpha_o,t)$ is multiplied by the ratio $\frac{g_i(90)}{g_i(\alpha_o)}$ and one obtains the rate at $\alpha_o = 90°$. The advantage of the above analysis is very great since all of the data may be reduced to one pitch angle and a complete time history may be obtained.

This technique has been extremely useful in studying the time history of the inner zone because the assumption of a constant shape for the pitch angle distribution is valid even during disturbed times. The only constraint seems to be that it must not be used near the loss cone where the rates drop off rapidly as a function of α_o. The region near the loss cone is a region of poor statistics and the limited number of data points in this region makes the curve fitting program subject to error. Furthermore, the region near the loss cone may also be more susceptible to short-term time variations. Keeping this restriction in mind a complete time history is plotted for various L's for all energy channels in Figures IV-6 through IV-10. The least square functions used to normalize the data were obtained from the September, 1964 - March, 1965 data. Table IV-2 lists the coefficients used for the function $g(\alpha_o)$ for the various L's.

TABLE IV-2

Least Square Polynomial Coefficients

L	Channel	a_0	$a_1 \times 10^4$	$a_2 \times 10^7$	$a_3 \times 10^{10}$
	1	5.025	-2.694	0	0
	2	5.045	2.173	-4.286	0
1.4	3	4.595	-0.7551	2.311	-2.816
	4	3.953	1.965	-5.971	1.116
	5	3.469	0.1406	-3.432	0
	1	5.222	2.323	-1.884	0
	2	5.177	1.676	-1.944	0
1.6	3	4.580	1.751	-2.243	0
	4	3.576	-2.071	-0.6244	0
	5	2.674	-3.754	0.1489	0
	1	5.208	-0.0301	-0.5865	0
	2	4.989	0.6984	-1.060	0
1.8	3	4.185	-1.129	0	0
	4	2.761	-3.579	0.0801	0
	5	1.454	-1.020	0	0
	1	5.208	-0.8404	-0.2664	0
	2	4.835	0.2504	-0.7189	0
2.0	3	3.699	-0.3270	-0.5417	0
	4	1.839	-1.699	-0.1262	0
	1	5.139	-0.9009	-0.2295	0
2.2	2	4.666	-2.027	0.2291	-0.0549
	3	3.034	-1.171	0	0
	1	4.876	0.2618	-0.4126	0
2.4	2	3.990	0.6169	-0.3599	0
	3	2.262	-1.232	-0.0182	0

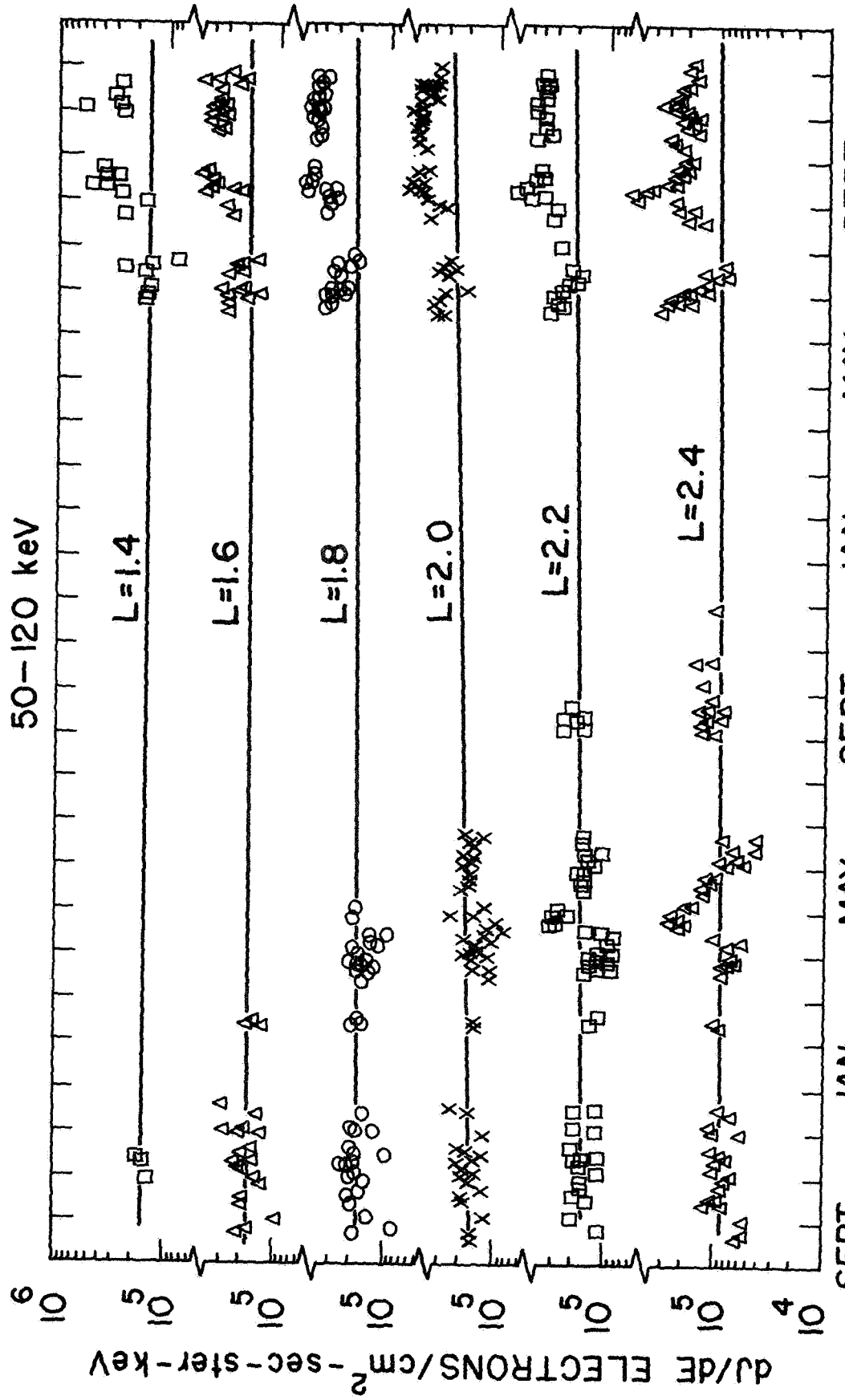
50-120 keV
L=1.4
L=1.6
L=1.8
L=2.0
L=2.2
L=2.4
SEPT 1964
JAN
MAY
SEPT 1965
JAN
MAY
SEPT 1966
dJ/dE ELECTRONS/cm²-sec-ster-keV
10⁶
10⁵
10⁵
10⁵
10⁵
10⁵
10⁴

Figure IV-6

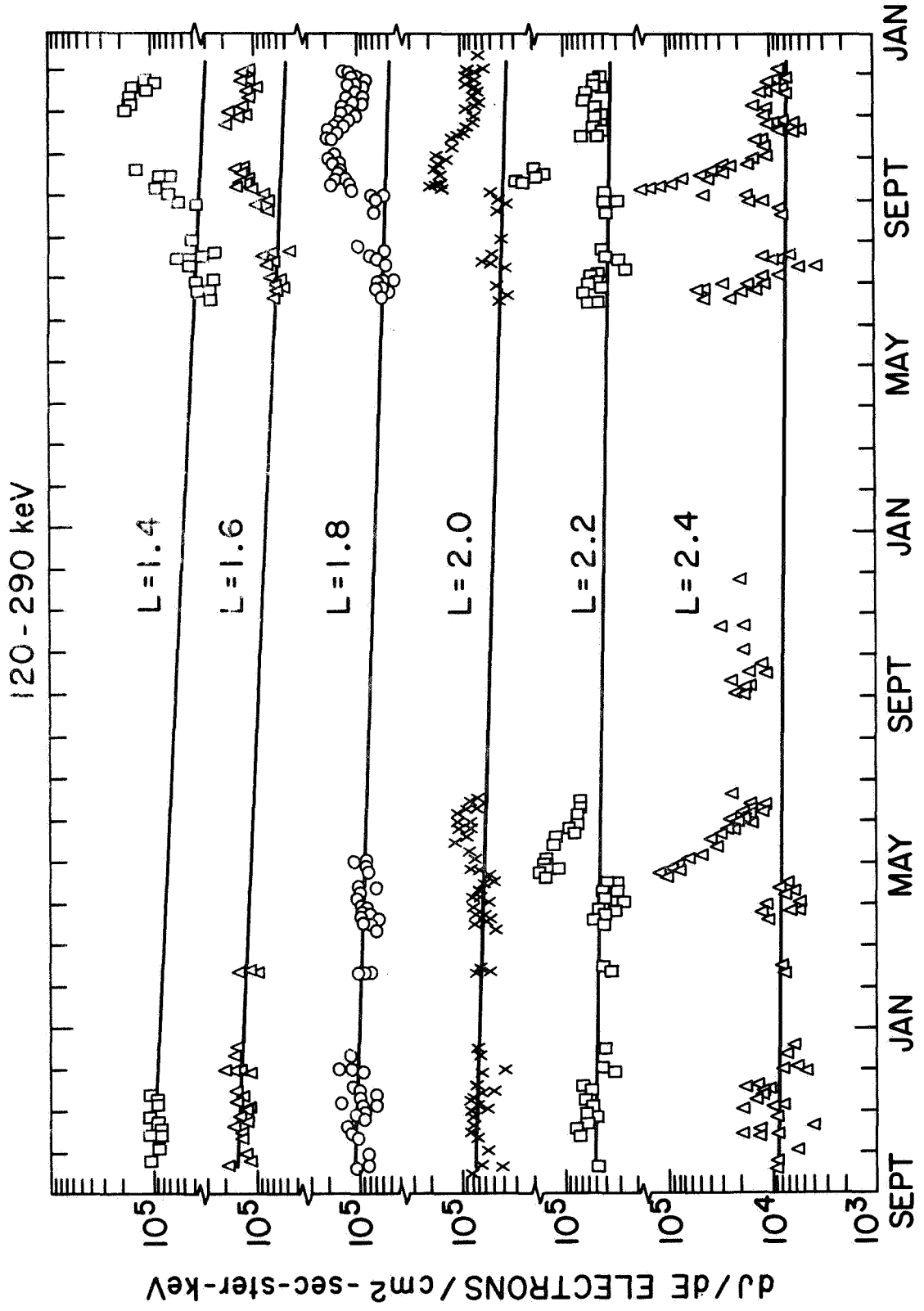
120-290 keV
L=1.4
L=1.6
L=1.8
L=2.0
L=2.2
L=2.4
SEPT
JAN
MAY
SEPT
JAN
MAY
SEPT
JAN
1964
1965
1966
10^5
10^5
10^5
10^5
10^5
10^5
10^4
10^3
dJ/dE ELECTRONS/cm2-sec-ster-keV

Figure IV-7

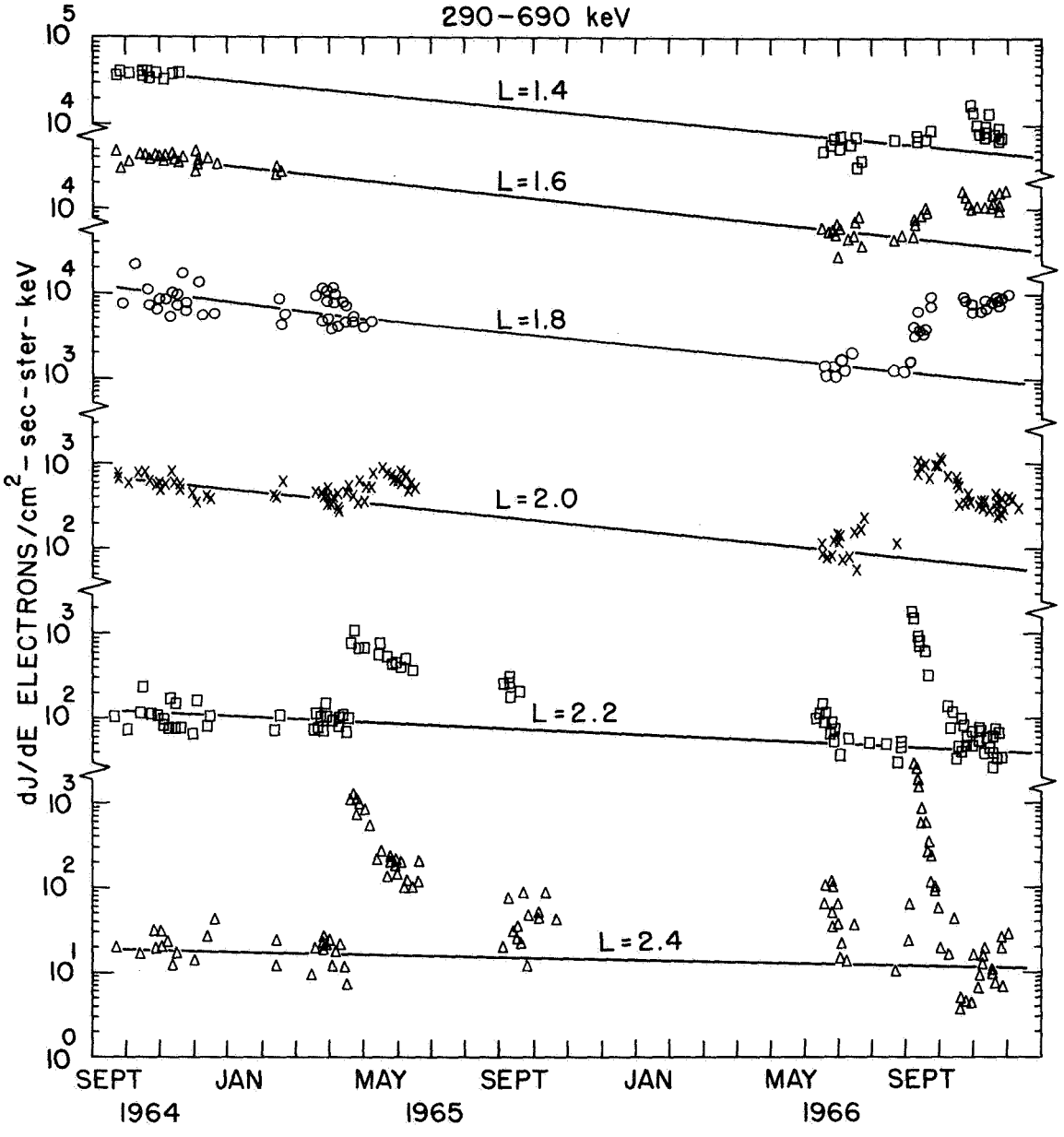
290-690 keV
L=1.4
L=1.6
L=1.8
L=2.0
L=2.2
L=2.4
dJ/dE ELECTRONS/cm²-sec-ster-keV
SEPT
1964
JAN
MAY
1965
SEPT
JAN
MAY
1966
SEPT

Figure IV-8

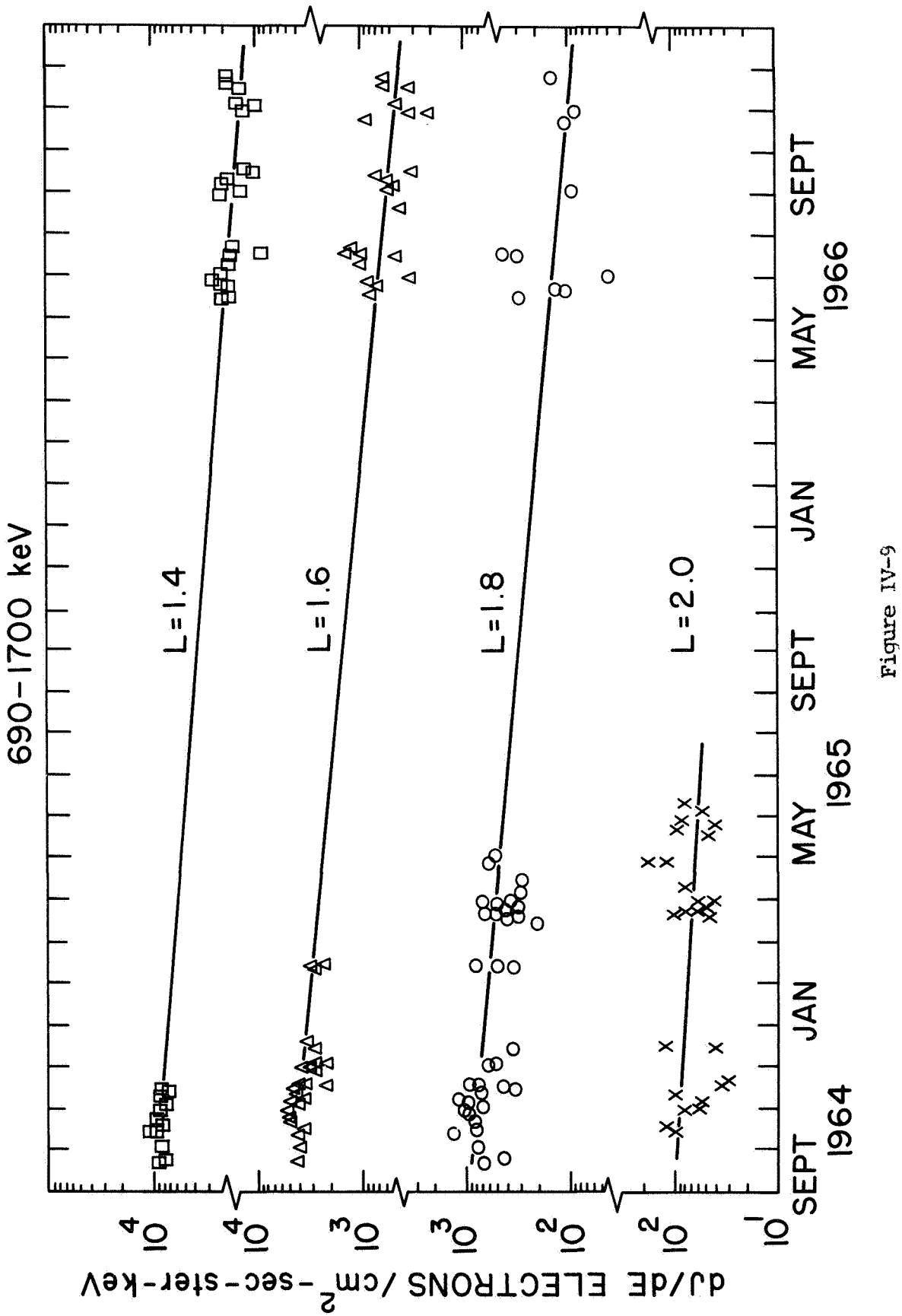
690-1700 keV
L=1.4
L=1.6
L=1.8
L=2.0
SEPT 1964
JAN
MAY 1965
SEPT
JAN
MAY 1966
SEPT
dJ/dE ELECTRONS /cm²-sec-ster-keV
10⁴
10⁴
10³
10³
10²
10²
10¹

Figure IV-9

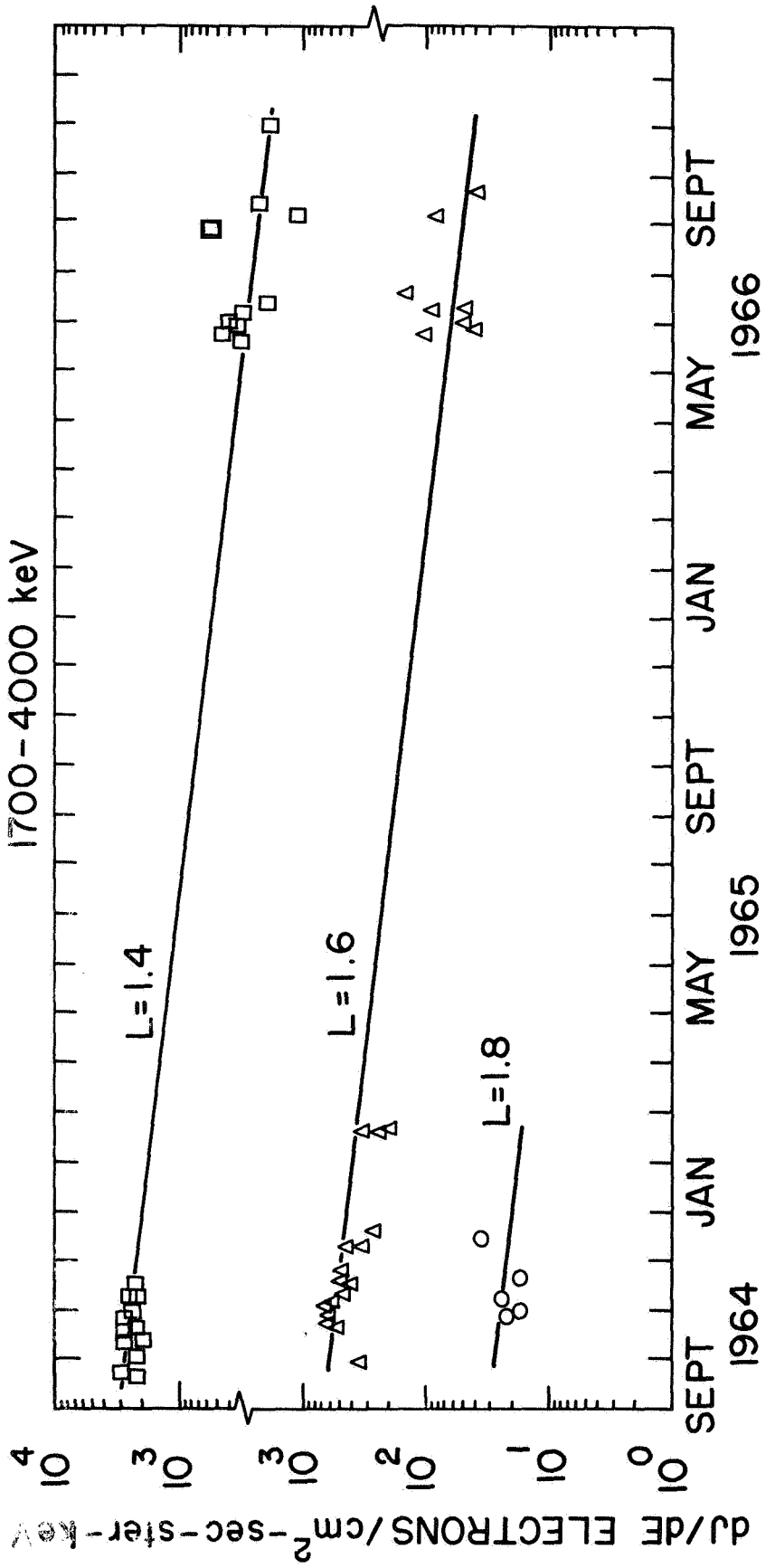
1700-4000 keV
L=1.4
L=1.6
L=1.8
SEPT
1964
JAN
MAY
SEPT
1965
JAN
MAY
SEPT
1966
dJ/dE ELECTRONS/cm²-sec-ster-kev
10⁴
10³
10³
10²
10¹
10⁰

Figure IV-10

Any change in the shape of the pitch angle function would destroy the validity of the above argument and would show up as a large scatter in the time plots. Most of the plots, however, show reasonably consistent curves over the entire two year period even during the large isolated disturbances.

The time plots (Figures IV-6 to IV-10) indicate no detectable sudden disturbances before September 2, 1966 for L's less than 2.0. Although there are several long periods when no data was obtained for $L < 2$, the time decay for $L < 2$ is sufficiently slow ($\tau > 200$ for 1/e decay) such that the effect of a large disturbance during an off period would be observable for several months. For smaller L's ($L > 1.5$) there is a data gap of over a year. We can, however, infer from measurement at larger L's where no sudden changes occurred and from measurements by Beall, et al. (1967) that only a slow monotonic change occurred during this period. We will show later that solar induced disturbances have a larger effect for larger L's.

Straight lines have been fitted through the data points indicating the long term time changes of the background levels of the various energy channels. Most of the channels indicate an exponential decay during this two year period. The time changes of the various energy channels will be discussed in the next paragraphs.

We can divide the flux of Channel i in August, 1966 by the flux of Channel i in September, 1964 and obtain a ratio R which will be a measure of the change in intensity of a given energy interval over the two year period.

$$R = \frac{dJ/dE\ (1966)}{dJ/dE\ (1964)}$$

R = 1 would indicate no change. Figure IV-11 is a plot of the ratio R as a function of L and summarizes the change in the intensity levels of the various energy intervals over the two year period.

We now examine each of the ratio curves in detail. The 50-120 Kev channel has a ratio somewhat larger than 1.0 for all L and therefore indicates that in this energy interval the electron flux has increased slightly during the past two years. The 120-290 Kev channel shows a decrease at all L with the decrease being largest at the smallest L. The 290-690 Kev channel also shows the largest decrease at L = 1.3. The ratio, R, for this energy interval is approximately 0.1 from L = 1.4 to 2.0 and then changes rapidly with increasing L such that at L = 2.6 R = 1.0. The 690-1700 and the 1700-4000 Kev channels show a ratio of approximately 0.1. There is a small peak in the ratio curve at L = 1.4 for the three highest energy channels indicating that the decay during the past two years was slower at L = 1.4 than for either smaller or larger L's. This peak in the decay ratio coincides with the peak measured

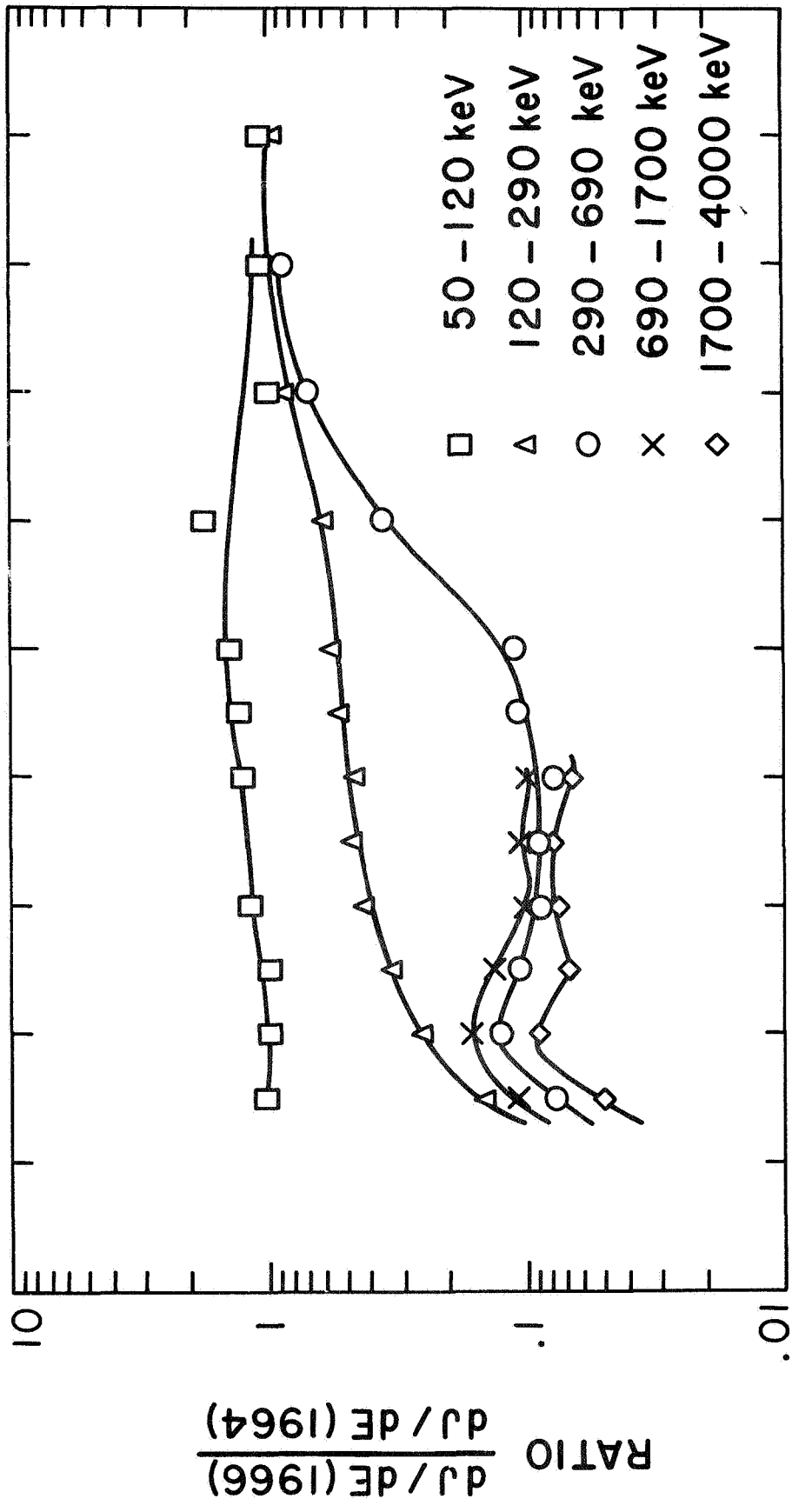
50 – 120 keV
120 – 290 keV
290 – 690 keV
690 – 1700 keV
1700 – 4000 keV
RATIO
dJ / dE (1966)
dJ / dE (1964)
10
1
.1
.01
1.0
2.0
L

Figure IV-11

by Paulikas et al. (1967). Paulikas et al. find that electrons of E > 1.6 Mev injected by the Starfish explosion decay most slowly at L = 1.4. The two highest energy channels are below threshold outside of L = 1.8.

We now compare the five ratio curves with each other. We find that the 50-120 Kev electrons exhibit the least decay, and the 1700-4000 Kev electrons have the most rapid decay. We can also note that the highest three energy channels have quite similar ratio curves. These curves show that between L = 1.3 and L = 1.8 the 690-1700 Kev electrons decay slower than the 290-690 Kev electrons which in turn decay slower than the 690-1700 Kev electrons. The steady slow decay over this long period of time may be measuring the electrons injected by the nuclear explosion Starfish on July 9, 1962. Following the nuclear explosion there were a series of measurements of these electrons (see review by Hess, 1963). The most recent measurements prior to OGO were carried out by Beall, et al. (1967). They proposed that the electrons they observed could be attributed to Starfish. The Beall, et al. measurements were made on a polar satellite and are restricted to very low L values, L < 1.4 or to equatorial pitch angles near the loss cone at higher L values. Nevertheless, since the OGO measurements include the range covered by Beall, et al. a comparison has been made.

Beall et al. using detectors on the polar satellite 1963-38C have measured the Starfish decay over a 40-month period beginning about 15 months after the Starfish explosion. They present the flux as the number of electrons-cm^{-2}-sec^{-1}-$ster^{-1}$ having energy greater than 280 Kev. The sum of our last three energy channels gives the flux above 290 Kev which is close enough for a direct comparison. Figure IV-12 gives a direct absolute comparison between the measurements of the two OGO's and the flux measured by 1963-38C. The agreement is excellent not only in the rate of decay, but also in the absolute measurement of the flux for L = 1.3, L = 1.4 and L = 1.55. This indicates that below L = 1.6 the Starfish electrons are still the dominating contribution to the flux of electrons above 290 Kev. The electron interval 120-290 Kev may also be at least in part made up of Starfish electrons. Below L = 1.4 this energy interval also exhibits a decay similar to that of the higher energy channels. All electron fluxes measured by the OGO's above 290 Kev in the inner zone for L < 1.8 before September 2, 1966 can be explained by assuming that the Starfish explosion was the entire source.

C. Injection of Natural Electrons into the Inner Zone

The OGO-I and OGO-III electron spectrometer observed the injection of electrons into the inner zone following the April 18, 1965 and the September 2, 1966 solar disturbances. These events may be observed on the steady state time plots of the last section (Figures IV-6 to IV-10). The April 18

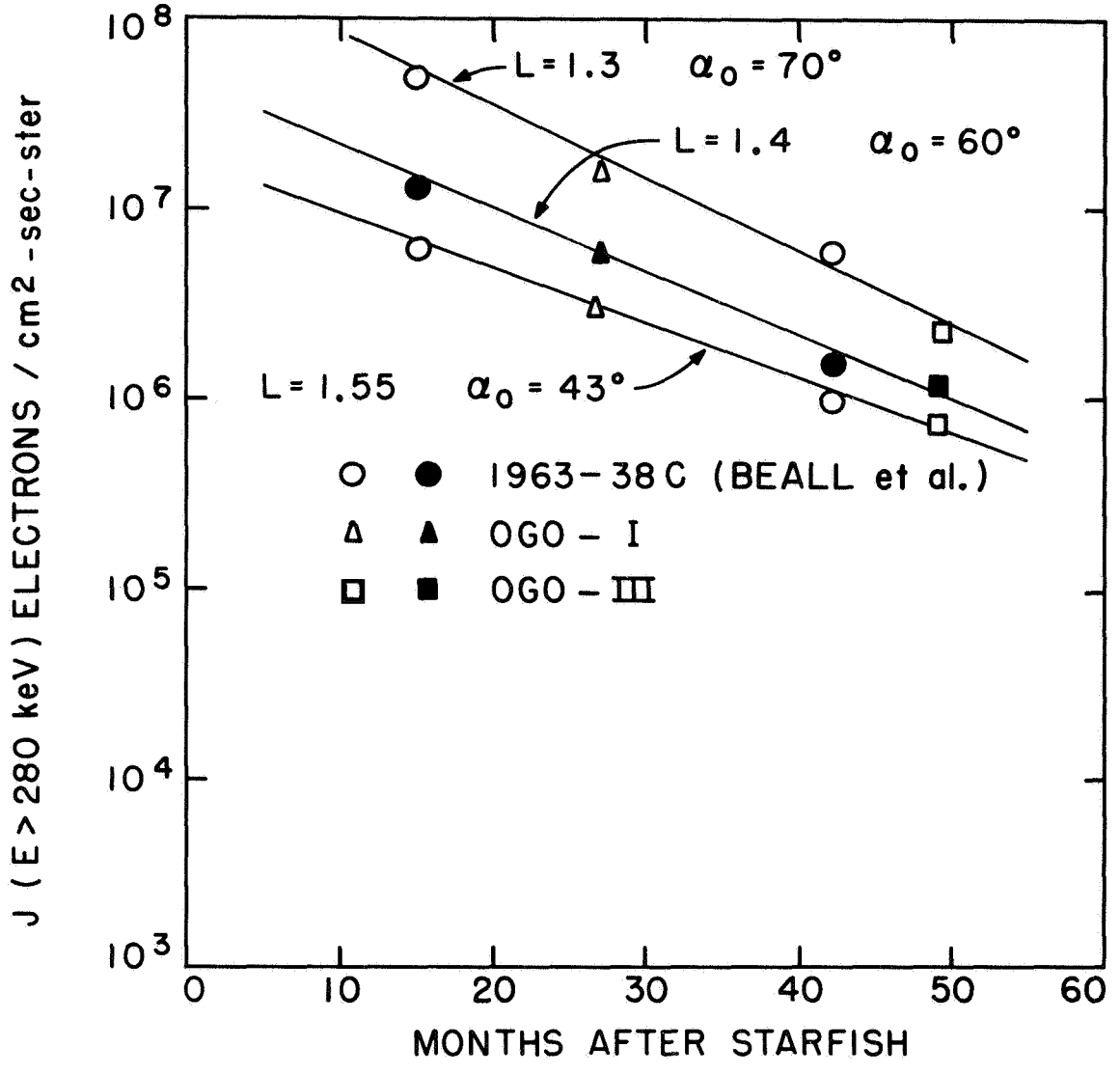
J (E > 280 keV) ELECTRONS / cm2 - sec - ster
10^8
10^7
10^6
10^5
10^4
10^3
0
10
20
30
40
50
60
MONTHS AFTER STARFISH
L = 1.3 α0 = 70°
L = 1.4 α0 = 60°
L = 1.55 α0 = 43°
1963-38C (BEALL et al.)
OGO - I
OGO - III

Figure IV-12

event affected the electron fluxes for L > 2.0; whereas the September 2 event affected the entire inner zone.

1. April 18, 1965 event.

We will first discuss the April 18, 1965 event. This event is well documented in the literature and is known to have produced a large perturbation of the radiation belts. The exact time of the injection of electrons into the outer zone is discussed by Brown et al. (1968). The injected electrons E > 300 Kev were first seen at L = 5.0 at about 0640 UT on April 18, 1968. The first pass of OGO-I through the inner zone was at 2100 UT on April 19, 1968. The OGO-I measurements during this event in the inner zone cover a wide range of pitch angles and therefore we must first establish the effect this event had on the shape of the pitch angle distribution. Figure IV-13 shows the fluxes before the onset of the event and about one month after onset of the event at L = 2.2. No detectable change in the shape of the pitch angle distribution is observed at L = 2.2 or at any other L in the inner zone. The pitch angle dependence is removed and all of the data is reduced to $\alpha_o = 90°$ by using the method of least square curve fitting described in the last section. The successful removal of the α_o dependence is indicated by the distinct flux versus time curves (Figures IV-14 through IV-16) which have a minimum of scatter even though the pitch angles vary from 30° to 80°. Since a constant normalization is

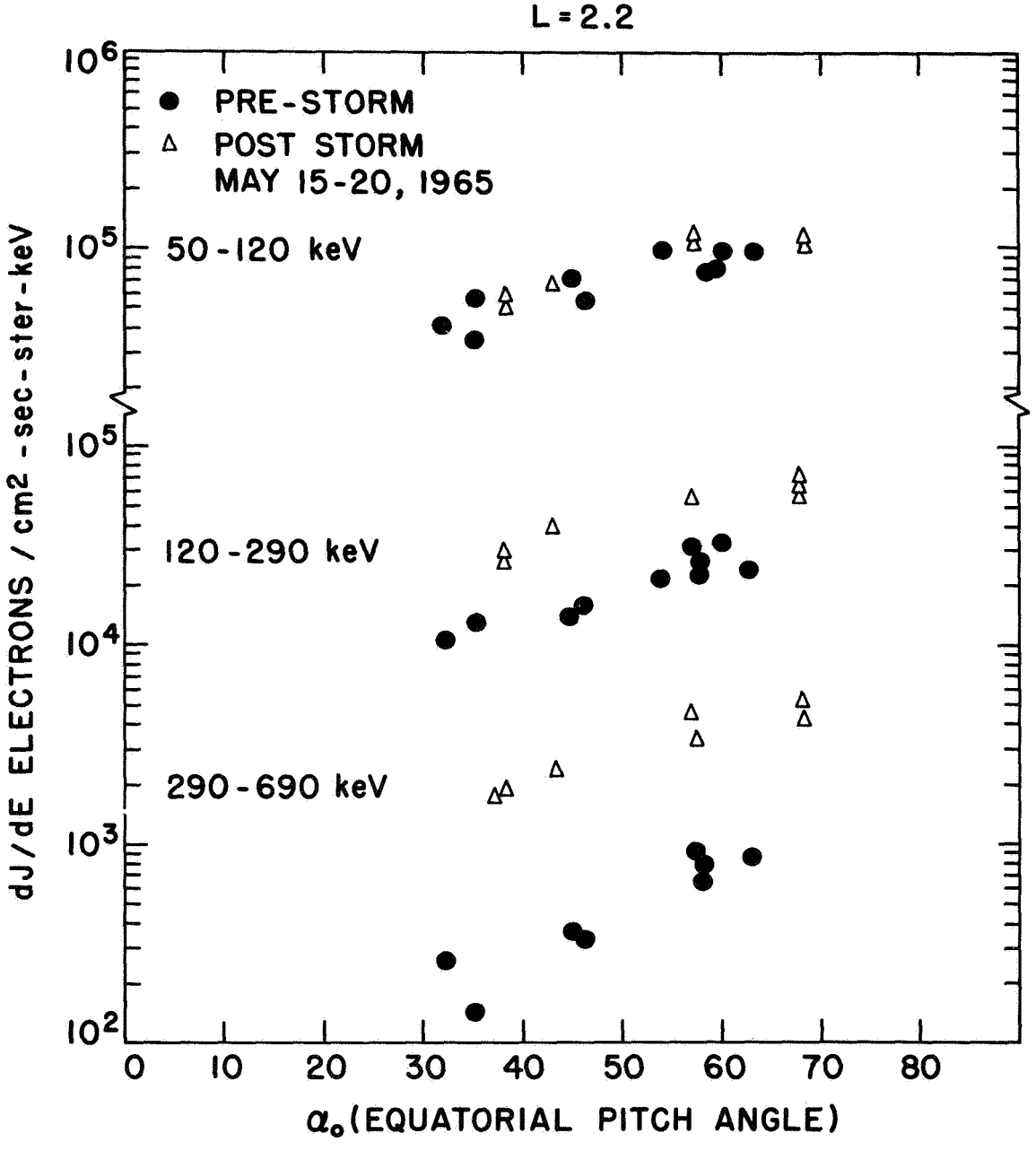
L = 2.2
PRE-STORM
POST STORM
MAY 15-20, 1965
50 - 120 keV
120 - 290 keV
290 - 690 keV
dJ/dE ELECTRONS / cm2 - sec - ster - keV
α_o (EQUATORIAL PITCH ANGLE)

Figure IV-13

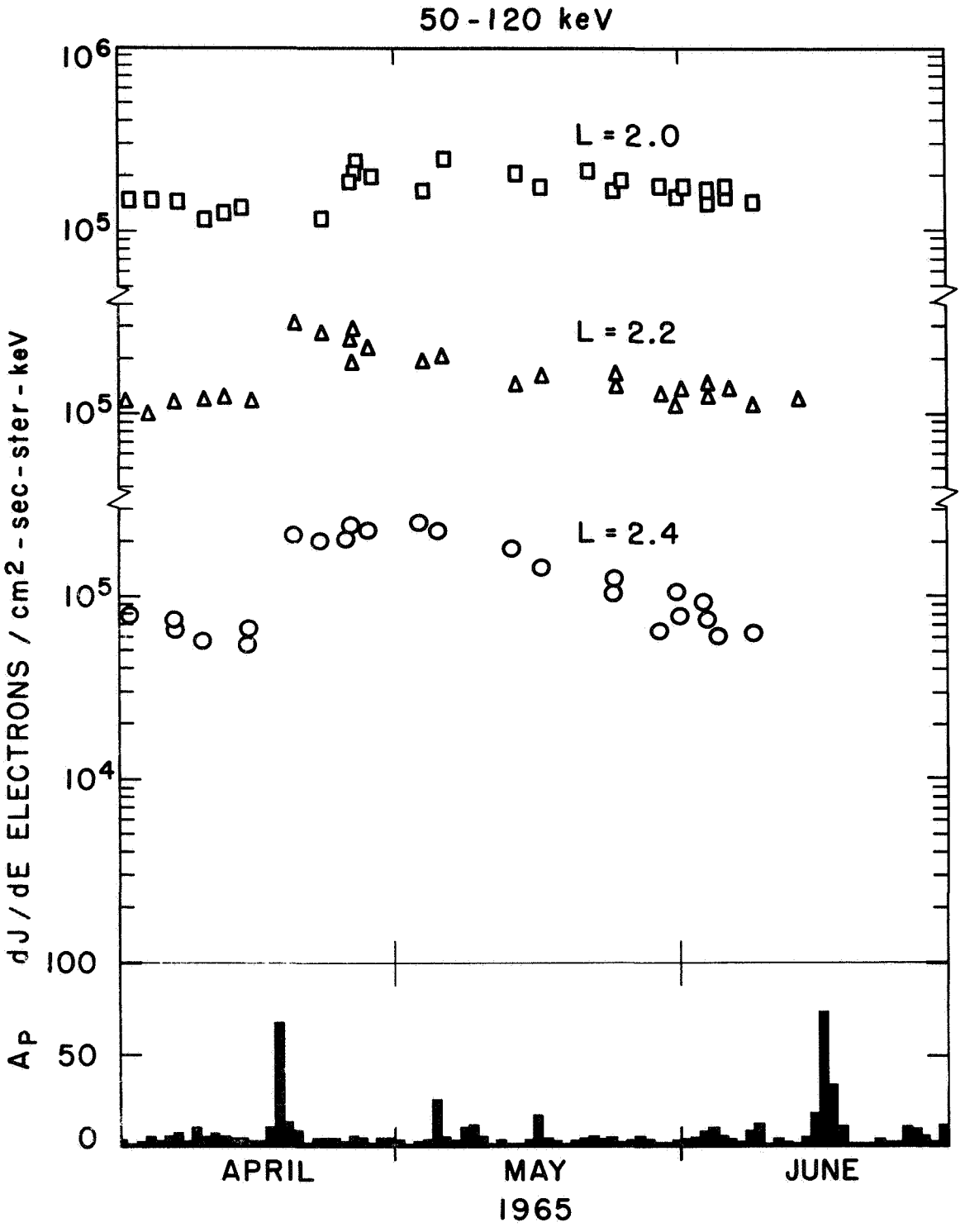
50 - 120 keV
L = 2.0
L = 2.2
L = 2.4
dJ / dE ELECTRONS / cm2 - sec - ster - keV
Ap
APRIL
MAY
JUNE
1965

Figure IV-14

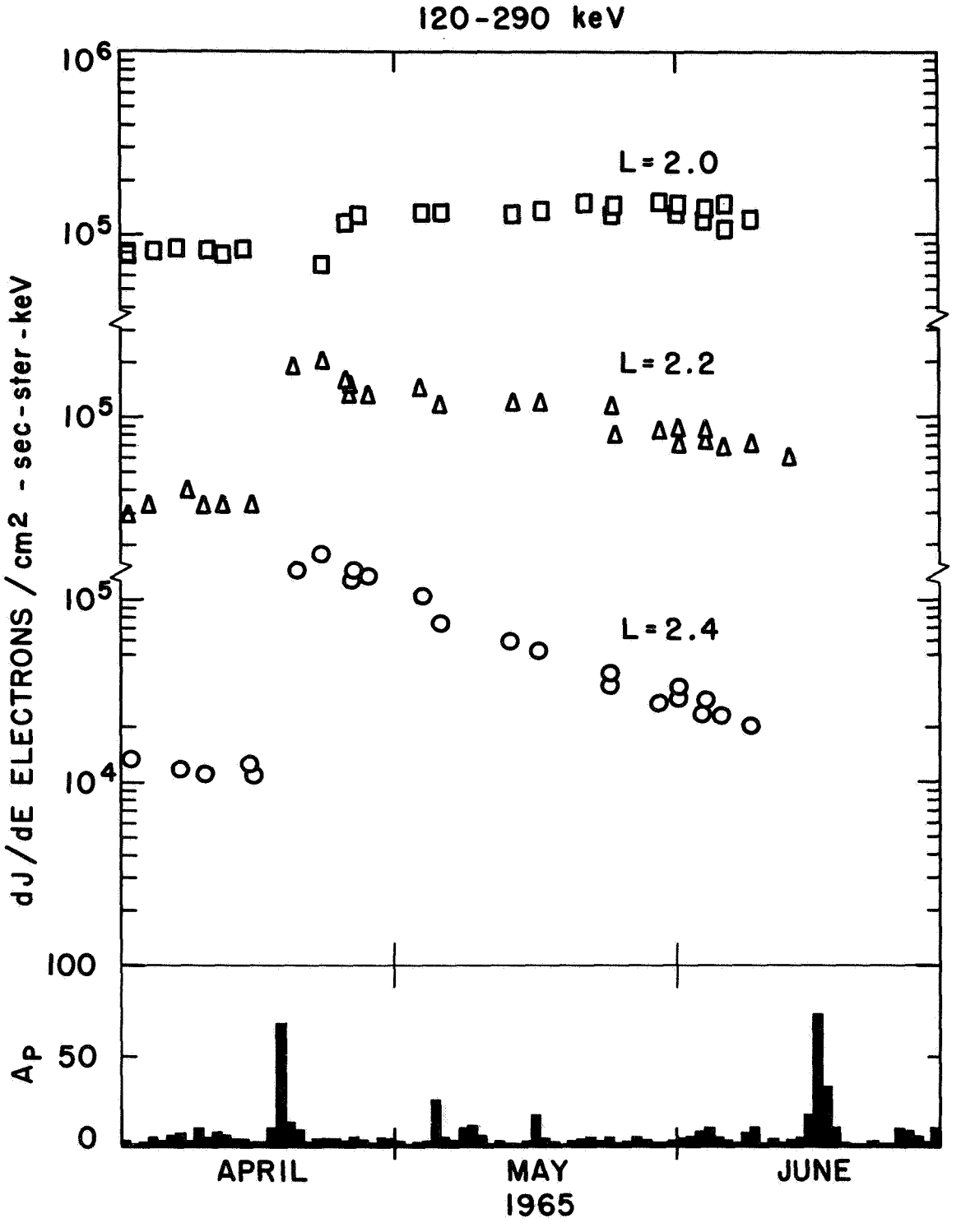
120-290 keV
L=2.0
L=2.2
L=2.4
dJ/dE ELECTRONS / cm2 - sec-ster-keV
10^6
10^5
10^5
10^5
10^4
100
A_P
50
0
APRIL
MAY
JUNE
1965

Figure IV-15

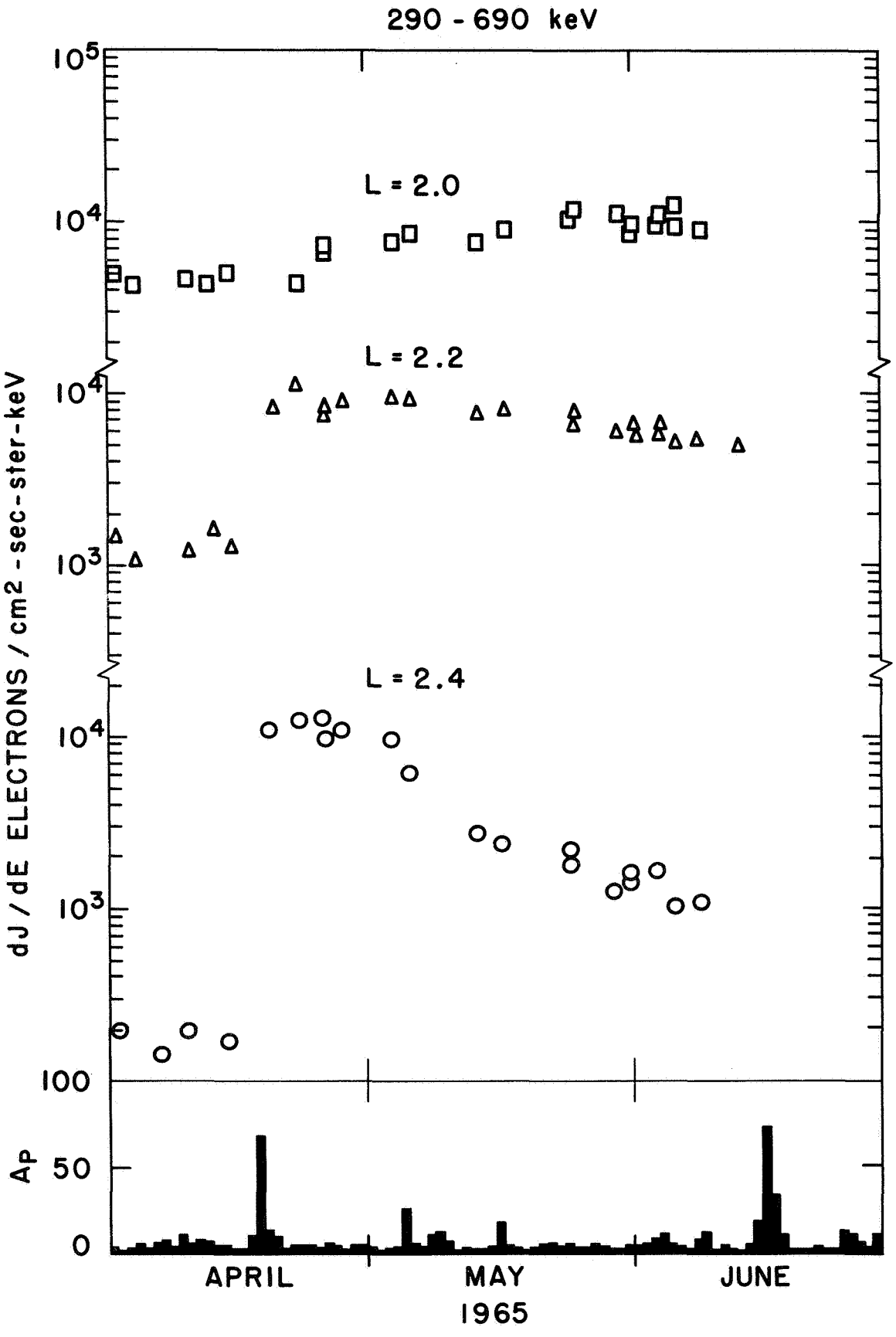
290 - 690 keV
L = 2.0
L = 2.2
L = 2.4
dJ / dE ELECTRONS / cm2 - sec - ster - keV
10^5
10^4
10^4
10^3
10^4
10^3
100
A_P
50
0
APRIL
MAY
JUNE
1965

Figure IV-16

used and since the scatter of the points is small during the entire event, the shape of the pitch angle dependence must have remained the same throughout the event. We will now discuss the behavior of electrons of different energies during and following the disturbance.

The 50-120 Kev channel shows no increase inside L = 1.8. For $L \geq 2.0$ the increase is quite pronounced. Figure IV-14 shows that the relative increase is greater for larger L's; however, the absolute flux after the increase is constant as a function of L. The onset of the storm is not well defined since only a few data points are available immediately after the onset of the event. We note, however, that at L = 2.2 and L = 2.4 the increase is first observed on the April 19th pass through the inner zone, one day after the onset. The data at L = 2.0 are missing for the April 19th pass. On the April 22nd pass through the inner zone, L = 2.0 shows no increase, whereas L's greater than 2.2 continue to show the full increase. The April 25th pass shows the full increase at L = 2.0. Therefore, we have a delay of 4-7 days before the effect of the disturbance is observed at L = 2.0. The delay for onset at L = 2.2 is, however, less than one day. After reaching a maximum the 50-120 Kev electrons decay exponentially for $L \geq 2.2$, the decay rate being more rapid for larger L's. At L = 2.0 we do not detect a decay until about one month after the onset of the event.

The 120-290 Kev channel (Figure IV-15) measures results similar to the 50-120 Kev channel. The absolute increase is constant as a function of L and the relative increase is very strongly L dependent. The relative increase at L = 2.0 is a factor of 2 and at L = 2.4 is almost an order of magnitude. Once again there is a delay of 4-7 days at L = 2.0 before the onset is observed; whereas the delay for L's greater than 2.2 is again less than a day. At L = 2.0 after the initial increase 4-7 days after the beginning of the event, the flux of electrons between 120-290 Kev continues to increase slowly for about 40 days. L's greater than 2.2 exhibit an almost immediate exponential decay which is faster for larger L's.

The 290-690 Kev electron channel (Figure IV-16) shows results closely similar to the 120-290 Kev channel. The 690-1700 Kev channel shows no increase for L = 2.0. For L's between 2.0 and 2.6 the 690-1700 Kev channel is below sensitivity threshold at all times. The first detectable increase for electrons having energies greater than 690 Kev is observed for L's greater than 2.6.

Figure IV-17 presents the energy spectrum before the event and after the onset of the event at L = 2.2. A more comprehensive picture of the event may be obtained from Figure IV-18 where the flux of the four lowest energy channels is presented as a function of L for three different time periods. The prestorm inner zone shows all energy channels monotonically decreasing as a function of L for L > 1.5.

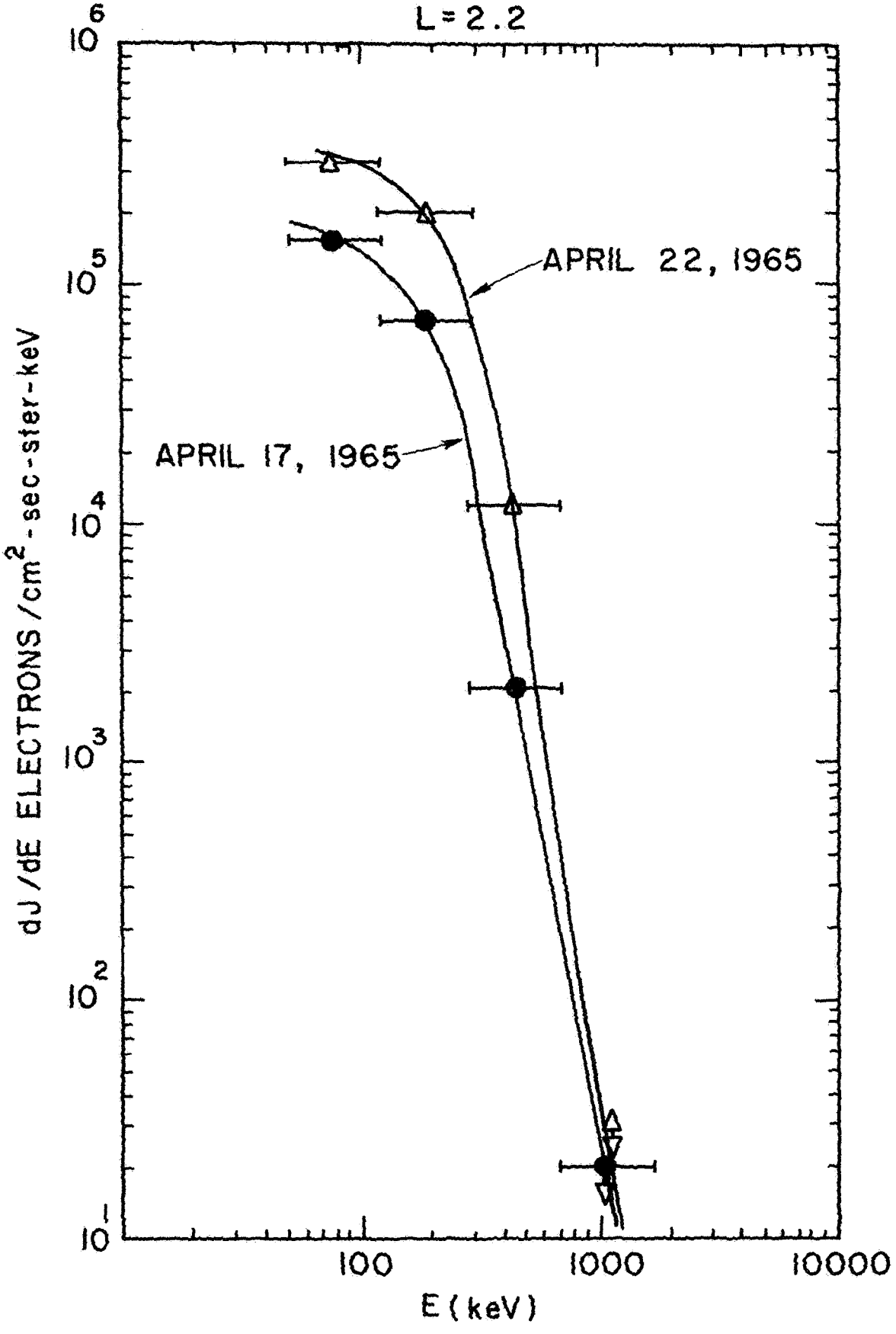
L = 2.2
APRIL 22, 1965
APRIL 17, 1965
dJ/dE ELECTRONS/cm²-sec-ster-keV
E (keV)
10⁶
10⁵
10⁴
10³
10²
10
100
1000
10000

Figure IV-17

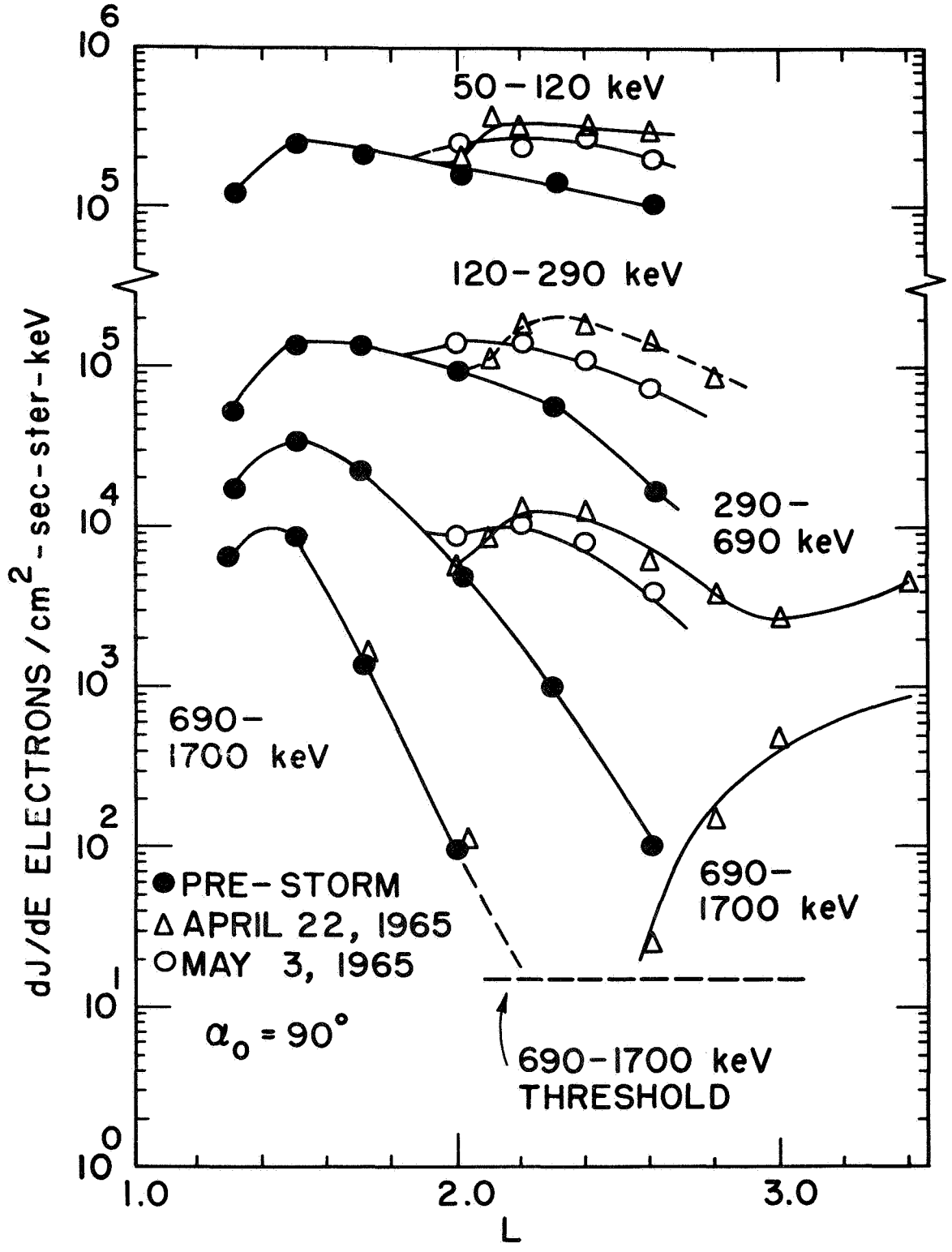
50 – 120 keV
120 – 290 keV
290 – 690 keV
690 – 1700 keV
690 – 1700 keV
PRE-STORM
APRIL 22, 1965
MAY 3, 1965
$\alpha_0 = 90°$
690 – 1700 keV THRESHOLD
dJ/dE ELECTRONS/cm^2-sec-ster-keV
L
1.0
2.0
3.0
10^6
10^5
10^5
10^4
10^3
10^2
10^1
10^0

Figure IV-18

Four days after the onset of the event we see a wave of electrons E < 690 Kev which has moved into approximately L = 2.1. Sixteen days after the event on May 3, 1965 we see the wave having penetrated to L's less than 2.0. We also note the decay of the wave for L's greater than 2.0. The 690-1700 Kev channel behaves quite unlike those with E < 690. Before the event the 690-1700 Kev channel is below threshold for L > 2.2. The wave of electrons with E > 690 penetrates to only L = 2.6 and then dissipates, and does not penetrate to L's less than 2.6 for the indicated threshold activity.

During this event we have observed the propagation inward of electrons to about L = 1.9. We do not notice any increase in the flux of electrons for L = 1.8. This is probably due to the large prestorm Starfish flux for L < 1.8 which obscures the behavior of the injection below L = 1.8.

2. September 2, 1966 event.

The September 2, 1966 event differed from the April event in a number of ways. The event was larger and was preceded by another event on August 28, 1966 which injected electrons to as low as L = 2.4. Furthermore, during the decay phase of the event the A_p indices averaged about 15 for the September event and about 5 for the April event.

Figure IV-19 presents as an example the pitch angle distributions for various times during the event for L = 1.9. Within the statistical uncertainties and within the limited

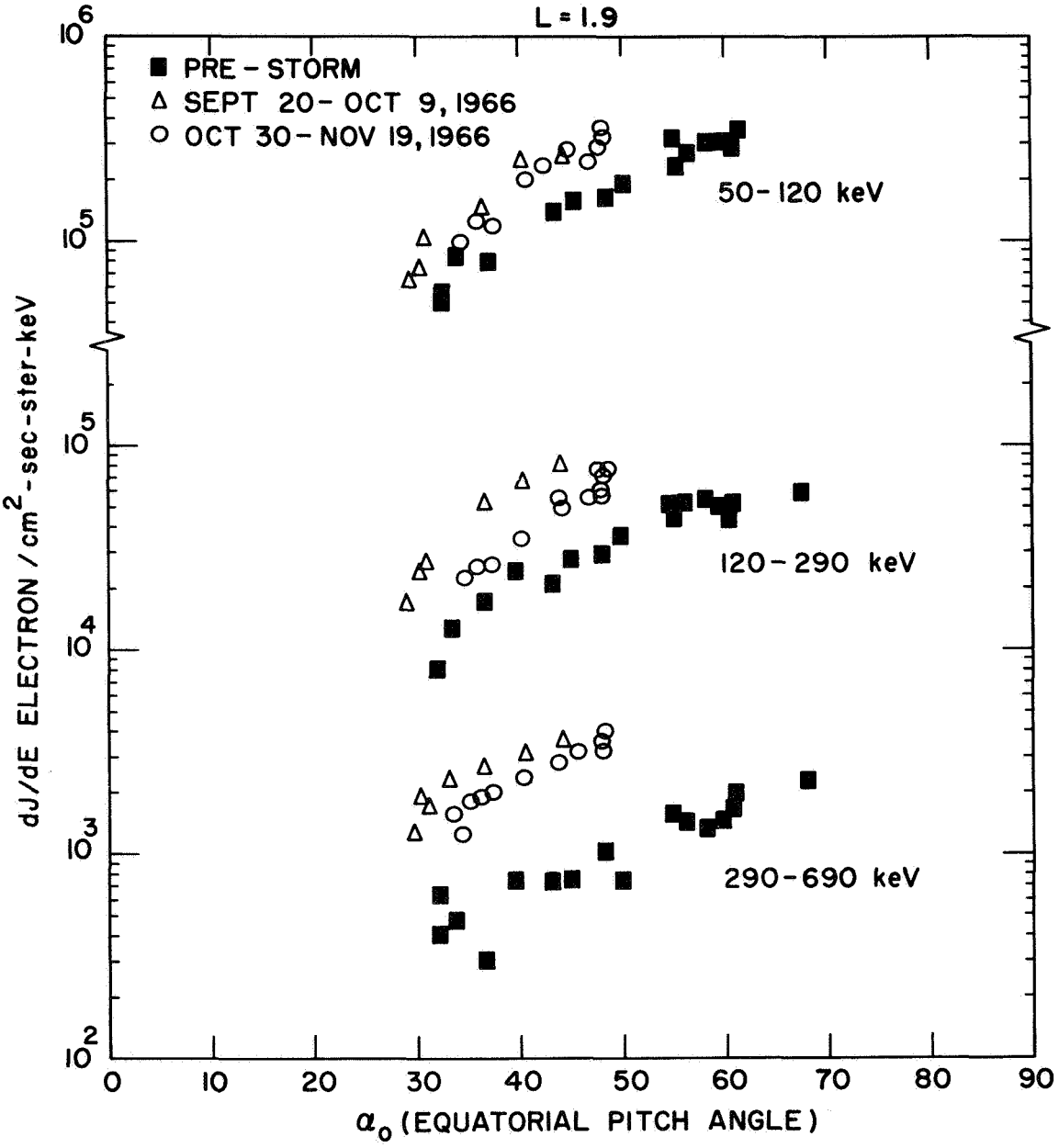
L = 1.9
PRE - STORM
SEPT 20 - OCT 9, 1966
OCT 30 - NOV 19, 1966
50 - 120 keV
120 - 290 keV
290 - 690 keV
dJ/dE ELECTRON / cm² - sec - ster - keV
α_0 (EQUATORIAL PITCH ANGLE)
10^6
10^5
10^5
10^4
10^3
10^2
0
10
20
30
40
50
60
70
80
90

Figure IV-19

range of pitch angles covered no change in the shape of the pitch angle distribution is observed in Figure IV-19. This lack of change in the shape of the pitch angle distribution is typical of all L shells in the inner zone during the September 2 event.

Once again as in the April event the pitch angle dependence is removed from the data. The normalization of the pitch angles to $\alpha_o = 90°$ is not successful for $1.3 \leq L \leq 1.8$ between September 20 - October 20. In those intervals the α_o are within a few degrees of the loss cone where the normalization curve is not accurate. Furthermore, near the loss cone the flux varies very rapidly as a function of α_o and even a small inaccuracy in the normalization curve introduces a large error. The data with α_o within 5° of the loss cone is not included in Figures IV-20 through IV-23 and results in gaps during the above time interval. Outside of this interval the removal of the α_o dependence from the data was quite successful.

The behavior of the four lowest energy channels of the spectrometer during the September event will now be discussed. Figure IV-20 represents the 50-120 Kev channel as a function of time for various L's in the inner zone. The effect of the September disturbance on this energy channel is quite small. For $L \leq 2.0$ the increase is approximately 50%. This increase persisted for over three months and showed no

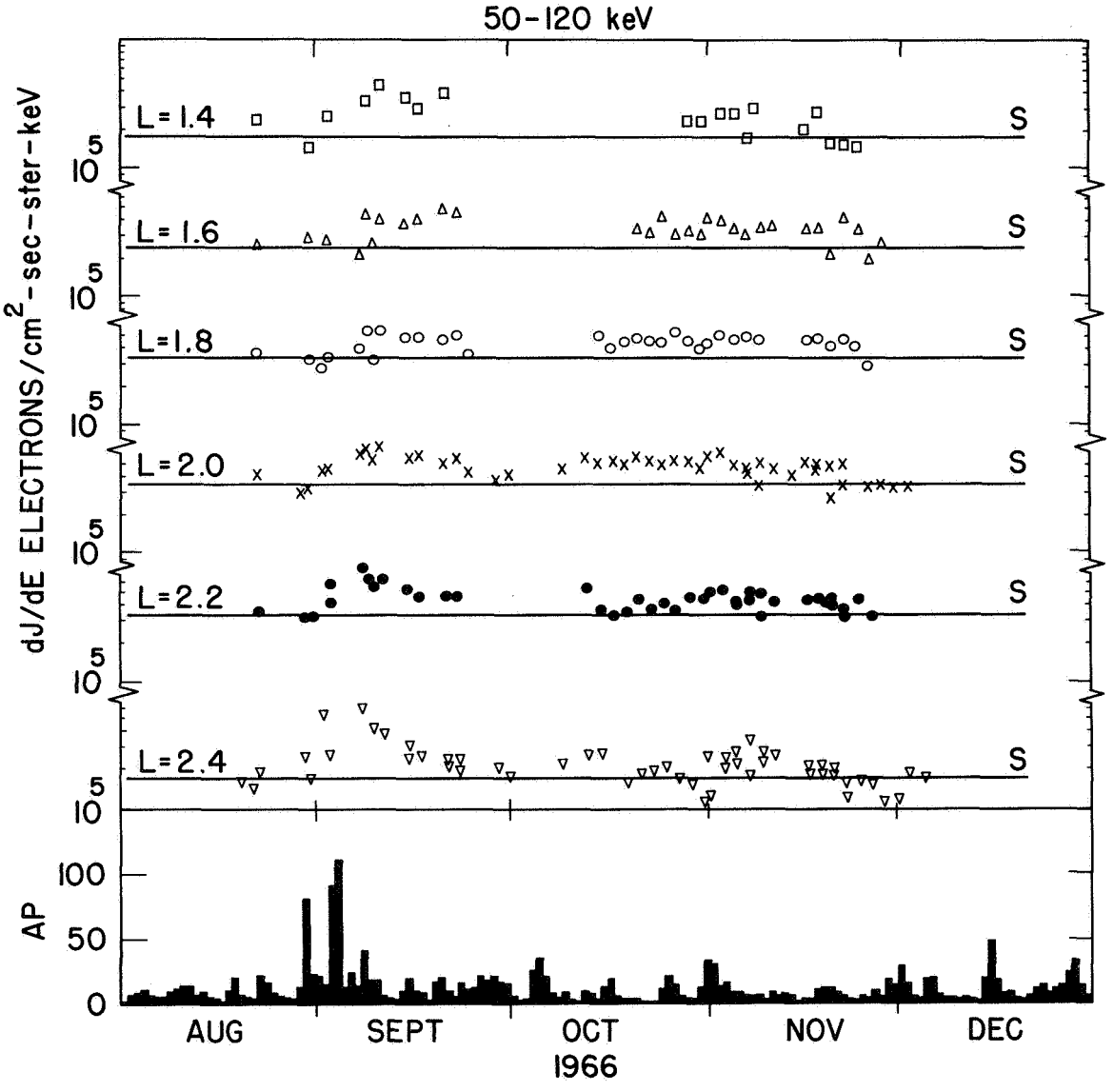
50-120 keV
dJ/dE ELECTRONS/cm²-sec-ster-keV
L=1.4
L=1.6
L=1.8
L=2.0
L=2.2
L=2.4
S
10⁵
AP
100
50
0
AUG
SEPT
OCT
NOV
DEC
1966

Figure IV-20

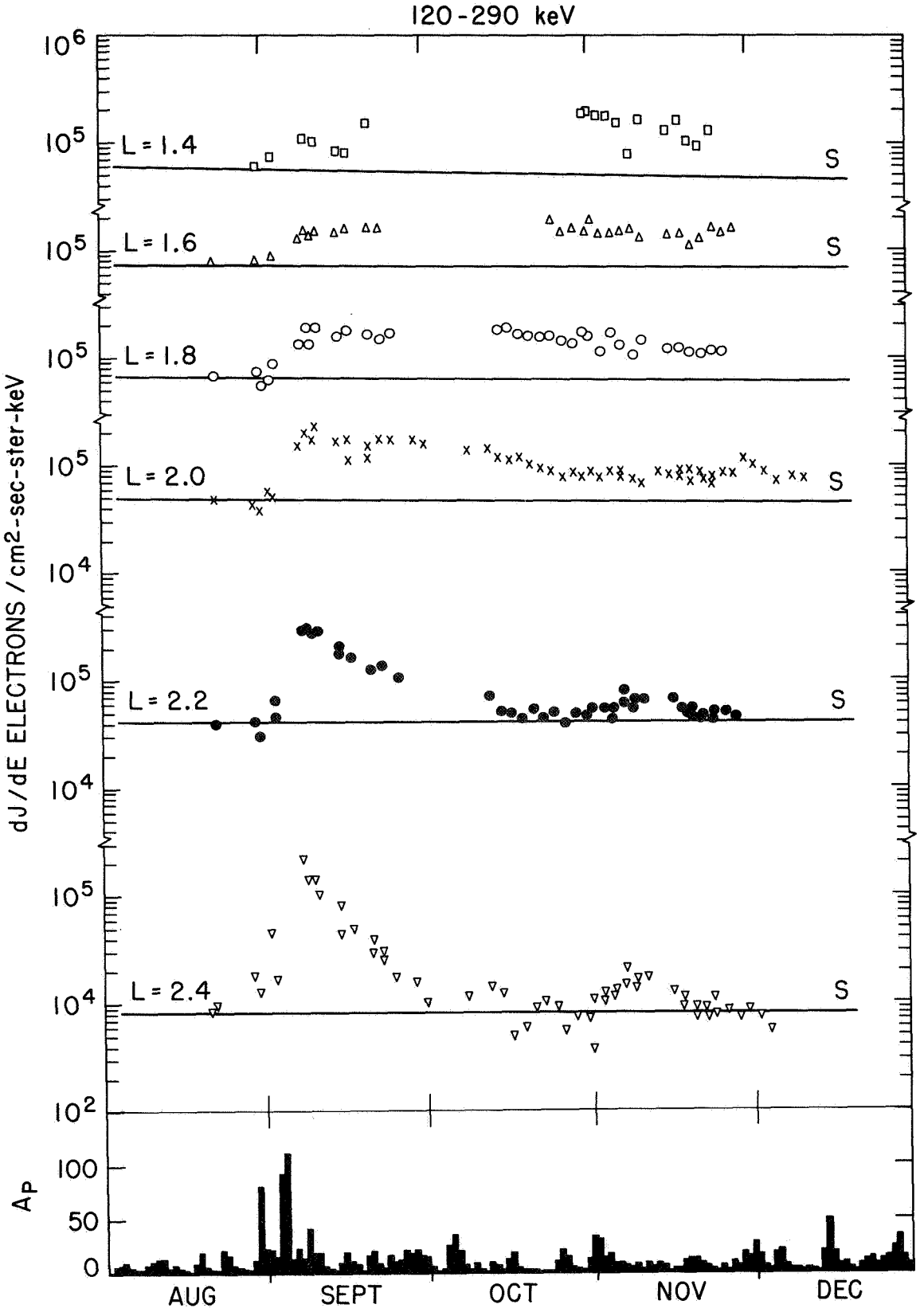
120-290 keV
dJ/dE ELECTRONS / cm2-sec-ster-keV
L = 1.4
L = 1.6
L = 1.8
L = 2.0
L = 2.2
L = 2.4
S
Ap
AUG
SEPT
OCT
NOV
DEC

Figure IV-21

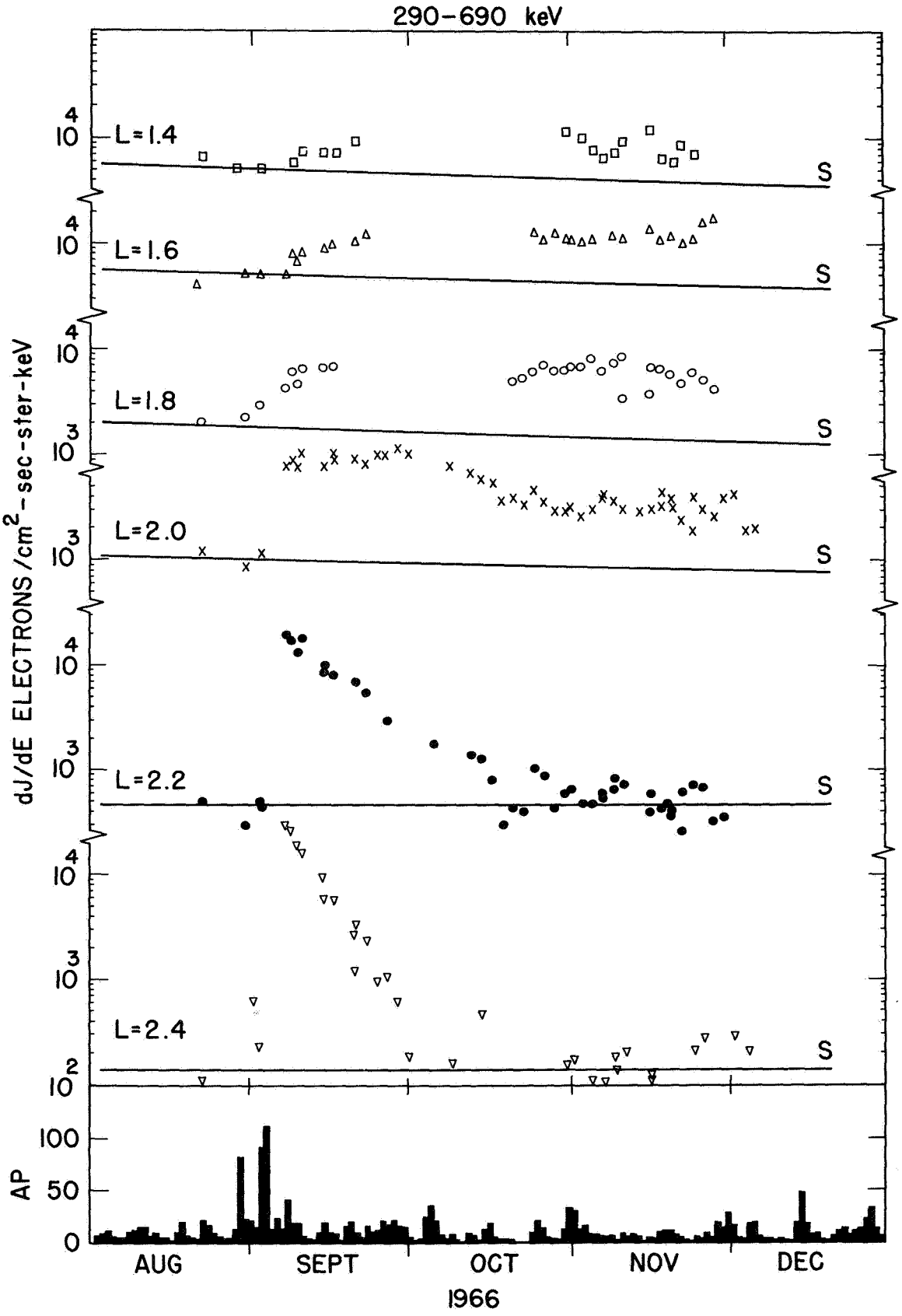
290-690 keV
L=1.4
L=1.6
L=1.8
L=2.0
L=2.2
L=2.4
S
dJ/dE ELECTRONS/cm²-sec-ster-keV
AP
100
50
0
AUG
SEPT
OCT
NOV
DEC
1966

Figure IV-22

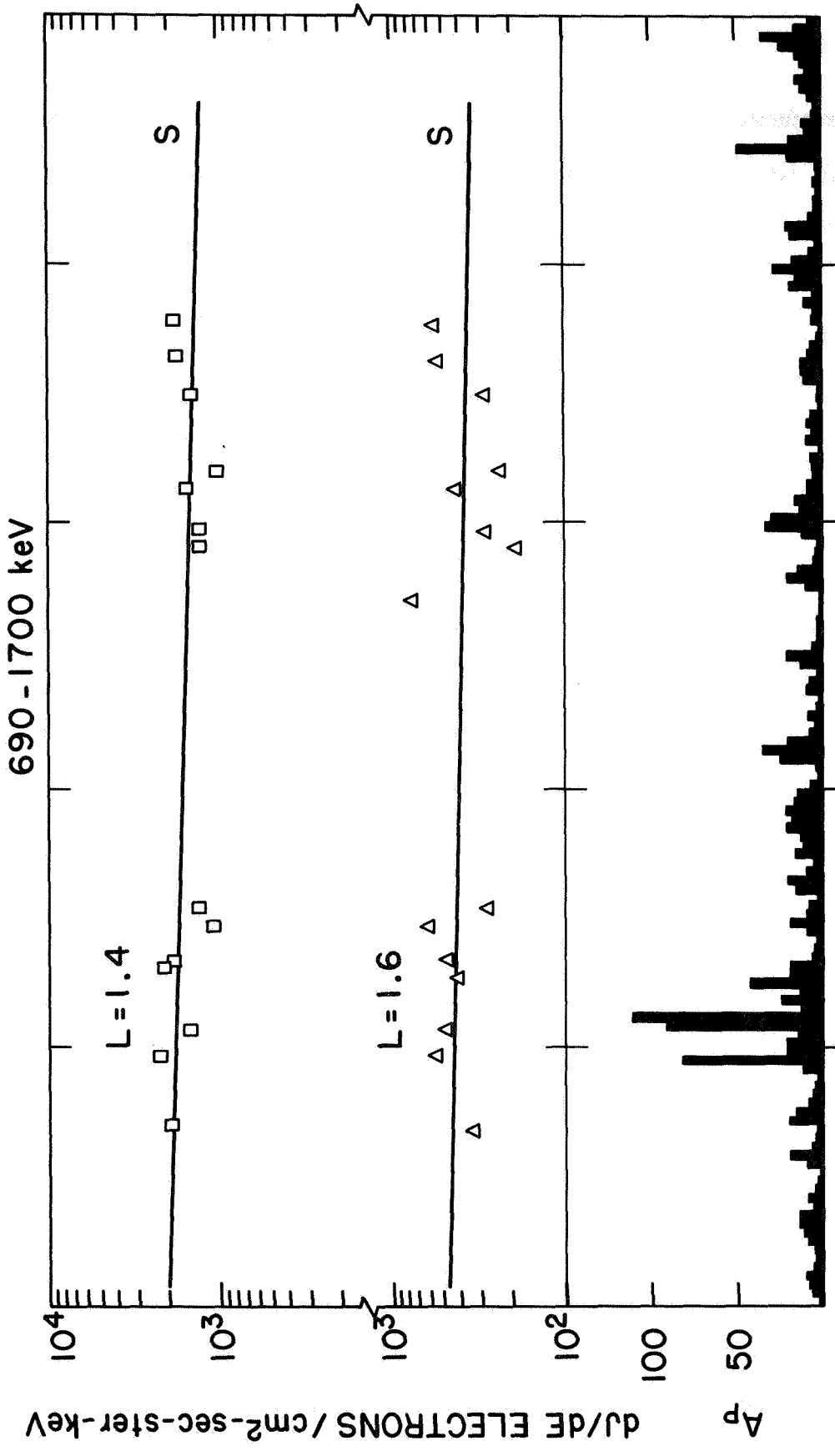
690-1700 keV
S
S
L=1.4
L=1.6
10^4
10^3
10^3
10^2
100
50
A_p
dJ/dE ELECTRONS /cm2-sec-ster-keV
AUG
SEPT
OCT
1966
NOV
DEC

Figure IV-23

evidence of decay. At L = 2.2 and L = 2.4 the increase immediately following the storm was somewhat larger. This increase, however, decayed quickly to the prestorm level.

The 120-290 Kev channel (Figure IV-21) and the 290-690 Kev channel (Figure IV-22) behaved almost identically during the September event. For $L \leq 1.8$ the rate after September 2 increased slowly over a period of 20 or more days and once the new level was reached no rapid decay was evident and the new level remained stable. At L = 2.0 the increase is more rapid reaching a peak in less than 5 days after the event begins. This level is maintained for about 30 days and then an exponential decay drops the flux to a new and apparently stable level. For $L \geq 2.2$ the increase is quite large and the exponential decay begins immediately and returns the flux levels to the prestorm level within 30-40 days after the onset of the event.

The 690-1700 Kev channel (Figure IV-23) behaves quite unlike the lower energy channels. The flux is above threshold for $L \leq 1.6$. No increase is observed inside L = 1.6 at any time after the event. Instead, the fluxes are observed to continue the Starfish decay discussed in the last section.

The entire event is summarized in Figure IV-24 which gives the prestorm fluxes, the fluxes 5 days after the event and the fluxes 18 days after the event. We see a slight increase for $L < 2$ five days after the event in the three

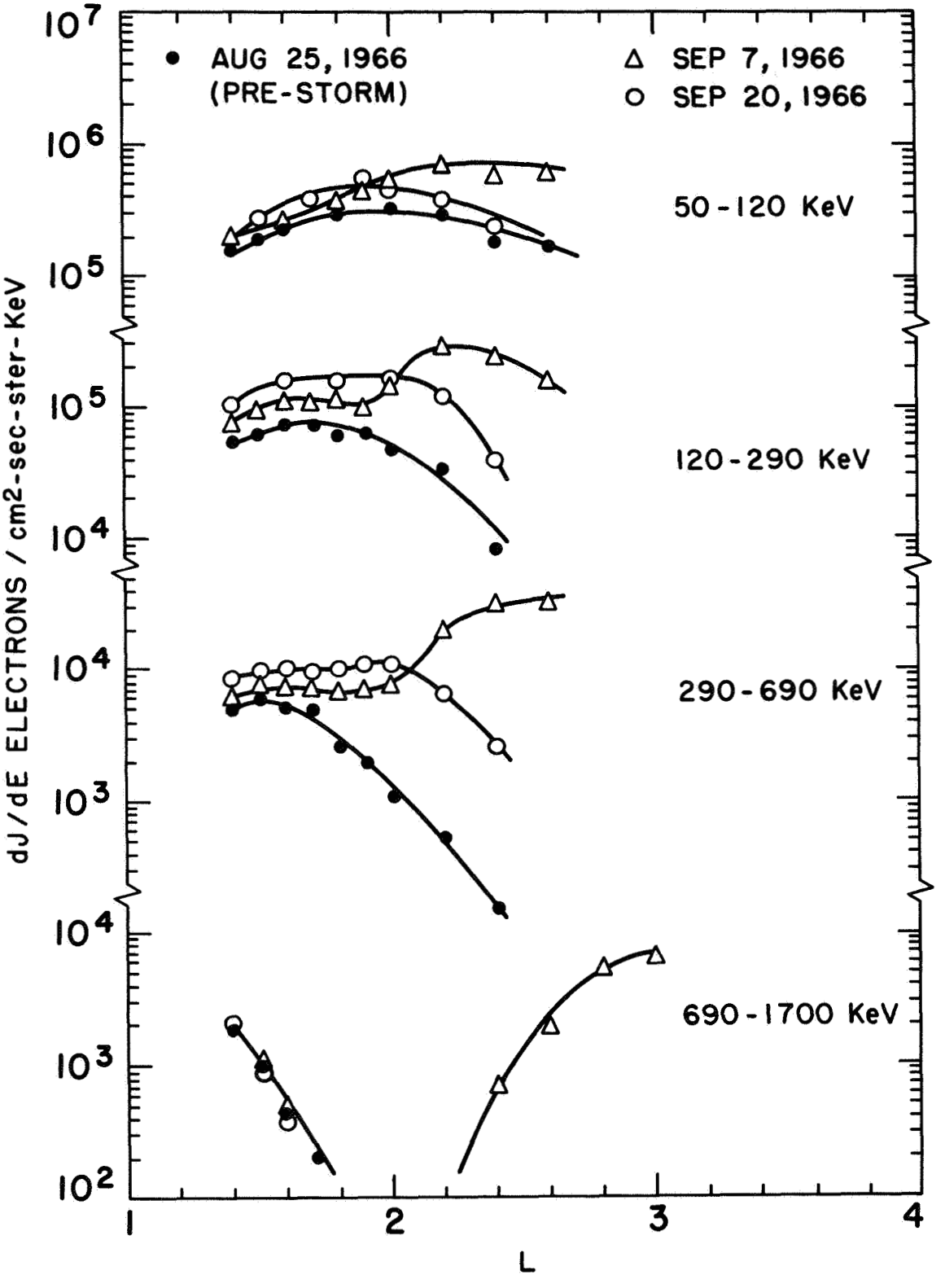
AUG 25, 1966
(PRE-STORM)
SEP 7, 1966
SEP 20, 1966
50 - 120 KeV
120 - 290 KeV
290 - 690 KeV
690 - 1700 KeV
dJ/dE ELECTRONS / cm2-sec-ster-KeV
L
10^7
10^6
10^5
10^5
10^4
10^4
10^3
10^4
10^3
10^2
1
2
3
4

Figure IV-24

lowest energy channels. For L > 2.0 the increase is much larger. Eighteen days after the event the fluxes for L > 2.0 have begun to decay; whereas, those for L < 2 have continued to increase. The 690-1700 Kev channel shows no increase below L = 2.4. Outside of L = 2.4 the flux is below threshold before the event. There is a large increase for L > 2.4 which decays below the threshold within ten days.

About 60 days after the onset of the event a new stable inner zone has been created (Figure IV-25). The fluxes for $L \geq 2.2$ have decayed to their prestorm levels and the fluxes for $L \leq 2.2$ have stopped their rapid post storm decay. We also note that for L < 2.0 there is an increase for electrons of E < 690 Kev; whereas, the electrons with E > 690 Kev show a decrease. This new stable inner zone will presumably continue the slow Starfish-like decay described in the last section.

The major observed difference between the April 18, 1965 event and the September 2, 1966 event is that the latter event affects all L's in the inner zone whereas the April event only L > 1.8. This is partly due to the lower residual fluxes in the inner zone before the September 2 event which permit smaller increases to be observed. The electron fluxes in the inner zone were almost an order of magnitude lower before the September event. Furthermore, the September event was more intense and injection of electrons into the inner zone was greater.

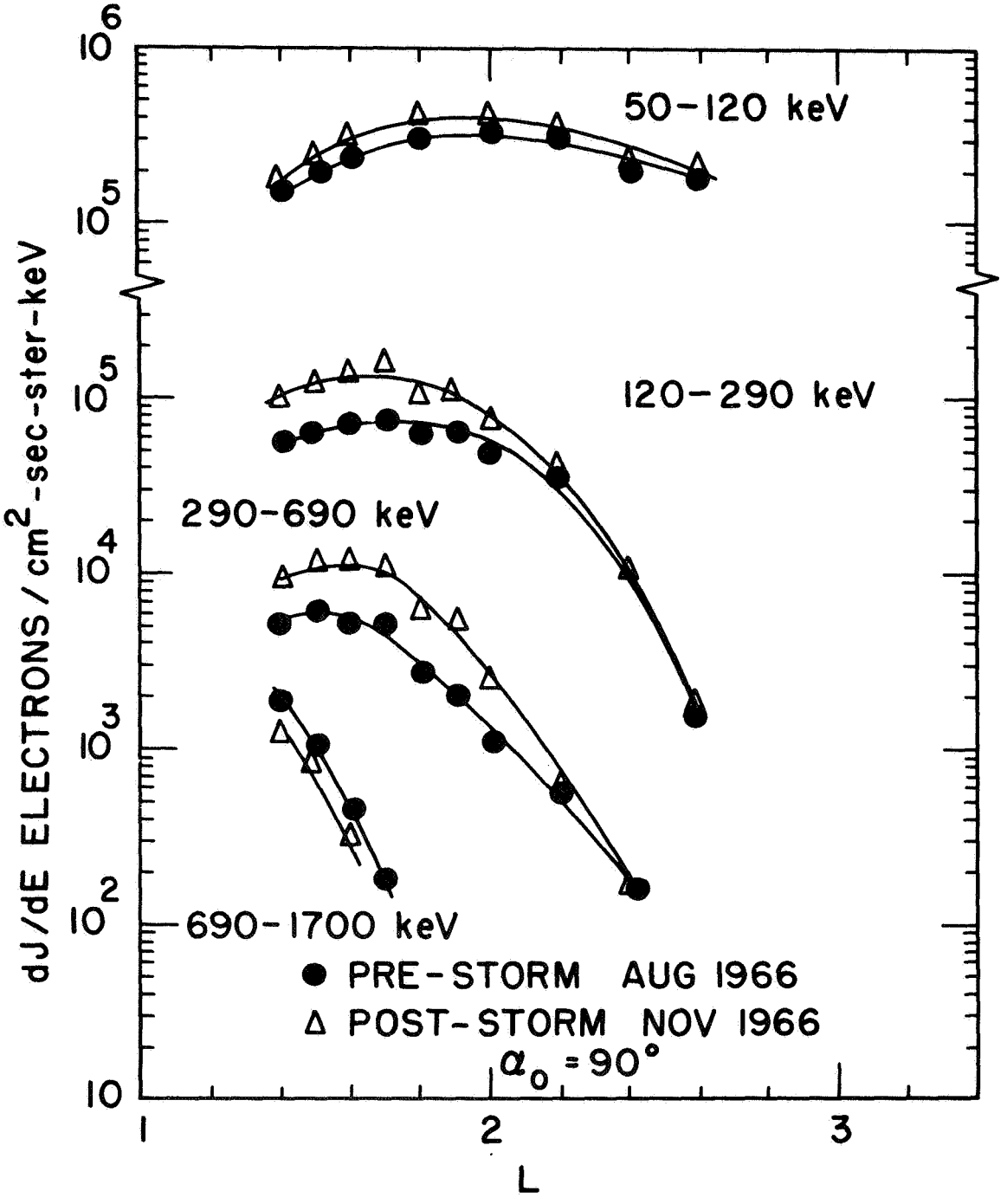
dJ/dE ELECTRONS / cm^2-sec-ster-keV
10^6
10^5
10^5
10^4
10^3
10^2
10
50-120 keV
120-290 keV
290-690 keV
690-1700 keV
PRE-STORM AUG 1966
POST-STORM NOV 1966
$\alpha_0 = 90°$
1
2
3
L

Figure IV-25

A second noticeable difference between the two events is that generally the exponential decays of the fluxes for L > 2.0 was more rapid following the September event. Figure IV-26 gives the time, τ, to decay by 1/e. We note from this figure that τ decreases with increasing L for all energies for both events, in most cases decreases with increasing energy, but lies in a completely different range in September, 1966 being more than a factor of two lower than in April, 1965. One should probably look to the geomagnetic disturbances during these time periods to explain the difference between the two events. The September event is during a period of much larger geomagnetic disturbance.

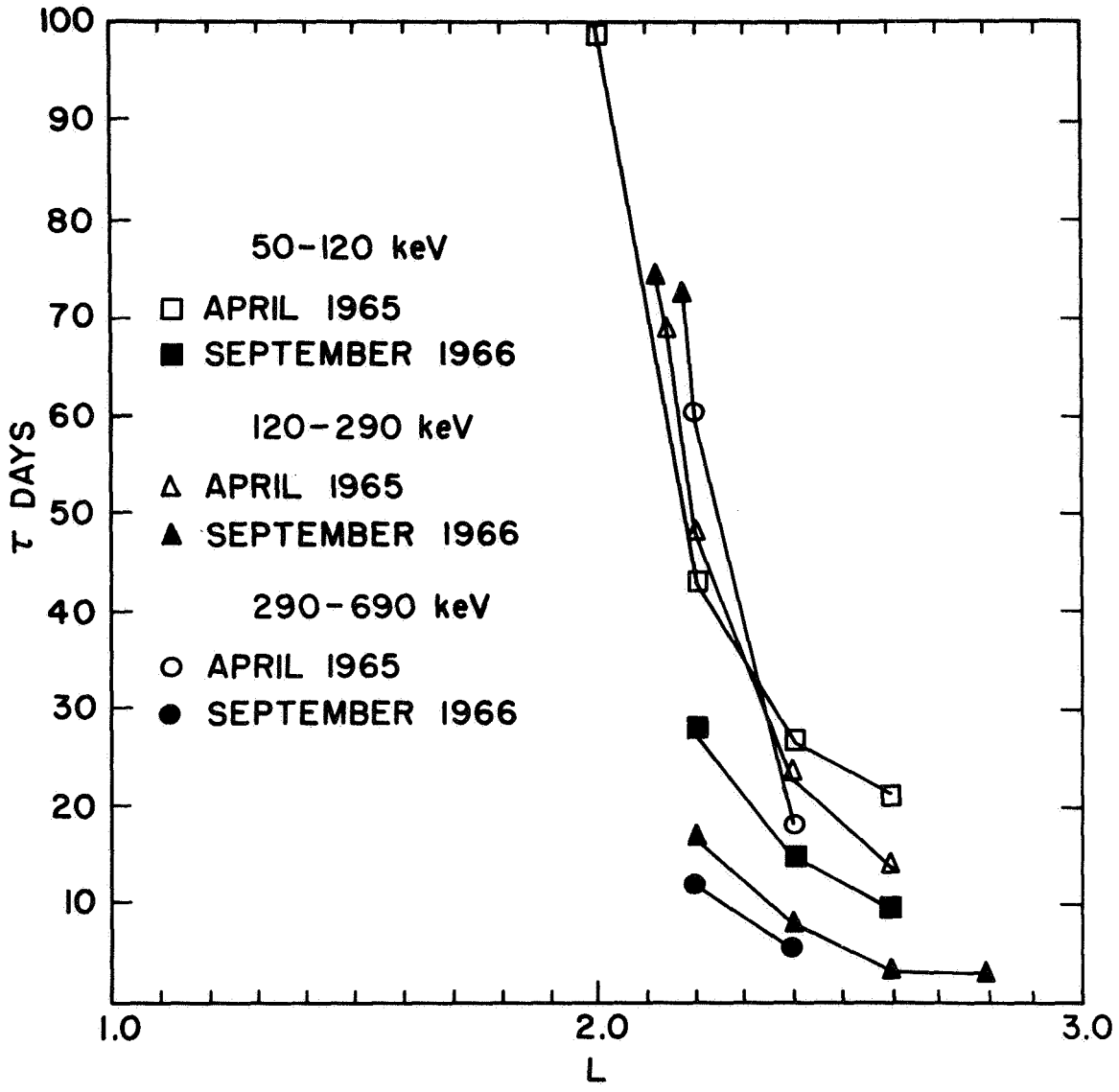
100
90
80
70
60
50
40
30
20
10
τ DAYS
50-120 keV
APRIL 1965
SEPTEMBER 1966
120-290 keV
APRIL 1965
SEPTEMBER 1966
290-690 keV
APRIL 1965
SEPTEMBER 1966
1.0
2.0
3.0
L

Figure IV-26

V. Conclusion

A. Conclusions and Summary

1. The electron spectrometers on OGO-I and OGO-III have successfully and accurately measured the electron fluxes from 50 Kev to 4 Mev throughout the entire inner zone.

2. The pitch angle and L dependences of the electron fluxes were found. The pitch angle distributions were found to be flat near $\alpha_o = 90°$ and were found to drop off rapidly near the loss cone. The storm-time pitch angle distribution of injected electrons observed at small L values ($L < 2.0$) may be obtained from the prestorm pitch angle distributions by multiplying by a function only dependent on the time and not on the pitch angle. That is, the increase at each pitch angle is proportional to the prestorm intensity already present at that pitch angle.

All energy channels exhibit a peak in the electron flux below $L = 2.0$ (Figure IV-25). The peak in the electron flux is at smaller L's for the higher energy electrons (at $L = 1.3$ for 690 to 1700 Kev electrons and at $L = 1.7$ for 120-290 Kev electrons). The rates for L values less than 1.3 drop rapidly due to the increasing importance of atmospheric scattering. For larger L values the flux also decreases with L. This is due presumably to magnetic effects. This decrease in the flux for increasing L is more rapid for the higher energy electrons.

3. A slow steady decay of the electron fluxes was observed during magnetically undisturbed times deep in the inner zone for electrons with E > 120 Kev. The 50-120 Kev channel was not observed to decay. At the outer edge of the inner zone (L > 2.0) the long term decay was very slow. (At L = 2.6 the levels in 1964 and 1966 were the same.) Following injection events the decay times for L > 2.0 became very rapid (Figure IV-26) until the prestorm levels were reached.

4. Prior to September 2, 1966 it was shown that for L < 1.8 Starfish remnants are an important part of the electron flux above 120 Kev. Following the injection event of September 2, 1966 the Starfish remnants are no longer important for E < 690 Kev. For E > 690 Kev, however, Starfish electrons are still the primary source of electrons for L < 1.6.

5. The injection of electrons (E < 690 Kev) deep into the inner zone was observed following a magnetic storm associated with the September 2, 1966 solar disturbance. The 50-120 Kev electron flux was increased by 50%, the 120-290 Kev electrons by 100% and the 290-690 Kev electrons by 200%. The maximum increase at the lowest L's (L = 1.4) was not reached for 30-40 days after onset. This increase was stable and the slow Starfish-like decays were resumed.

6. During the two year period of observation by OGO-I and III we have observed approximately a factor of 10 decay in the inner zone for L < 2.0. Therefore, any continuously

acting acceleration process such as direct injection of energetic solar electrons, cosmic ray albedo neutron decay, photoelectric processes and local acceleration of electrons from the ambient plasma are not sufficiently strong to prevent the decay of electrons having E > 120 Kev. However, the magnetic storm following the September 2, 1966 event was observed to inject electrons of E < 690 Kev to L values as low as 1.4. Because of the very slow decay (τ = 300-400 days) deep in the inner zone these newly injected electrons will decay to the prestorm levels for L < 1.8 in about one year. Therefore, only one or two events of this magnitude per year would suffice to supply the inner zone electrons (50 < E < 690 Kev) below L = 2.0.

Unlike the higher energy electrons the 50-120 Kev electrons were not observed to decay during the two year period. Therefore, one must either assume that 50-120 Kev electrons do not decay (a very unlikely assumption) or that the 50-120 Kev electrons are replenished by a continuously acting source in equilibrium with the loss rate. The observed injection of 50-120 Kev electrons following the September 2, 1966 event raised this equilibrium level by 50%. The new level created by the injection is apparently stable and more long term measurements are necessary before we can determine if the 50-120 Kev electron flux returns to the prestorm equilibrium.

We also have observed that following the onset of a strong magnetic storm a wave of electrons would fill the outer and inner zone to about L = 2.2 within hours after onset. This wave of electrons for E < 690 Kev was then observed to move inward in a diffusion-like manner over a period of 30-40 days. Electrons of E > 690 Kev which also were seen to move in to L = 2.4 in a wave-like manner were, however, not observed to diffuse inward to L values less than 2.2. All of the electrons of E > 690 Kev measured by OGO below L = 1.8 can be attributed to the Starfish explosion.

7. A comment about the much discussed "slot" at L = 3.0 is in order. The "slot" has often been described as an instrumental effect. The detectors are said to measure electrons in the outer zone and protons in the inner zone with the "slot" occurring at the cross-over point. Although the appearance of the "slot" may be enhanced by instrumental effects in some cases, there is indeed a large minimum in the electron flux in the vicinity of L = 3.0 (see Figure III-24). Following an injection event the slot is filled in with new particles, but since the 1/e lifetimes in the slot are about 3-5 days the flux of electrons at L = 3 rapidly disappears. The flux also decays rapidly for L > 3, but in the outer zone numerous small injection events supply sufficient electrons to maintain a higher flux level. These small injection events do not inject electrons to L's as low as 3.0. The

large flux in the inner zone is maintained by the very slow decay times and by the one or two large events that are intense enough to propagate into the inner zone. The presence of the "slot" as seen in the electron component can thus be understood.

B. Future Analysis

We must study other injection events which may help answer some of the following questions that have been raised by the analysis of the two injection events descussed in this thesis:

1. Why do the high energy electrons decay slowly over a long period of time whereas the 50-120 Kev electrons maintain an equilibrium level?

2. Is the diffusion influenced by the level of activity after the event?

We have observed diffusion inward to L values less than 1.8 following the September 2, 1966 event but not after the April 18, 1965 event. Presumably this is because the large Starfish background obscured any inward diffusion following the April 18, 1965 event, but the continuing strong magnetic activity following the September event may also be responsible for the strong diffusion following the September event.

3. Why are there two distinct rates of decay in the inner zone?

For $L > 2.2$ we have observed a rapid decay back to prestorm levels following both of the events. Once the prestorm

level is reached the decay rate changes dramatically from the order of 10 days to over 100 days. This change in the decay rate is not a function of flux level since the levels at which the rapid decay ends are different for the two events.

4. Why does the rapid decay rate differ so strongly between events?

The rate of the rapid decay is almost twice as fast for the September event as for the April event. Perhaps the state of agitation of the belts (as indicated by the A_p indices) may offer a clue. The A_p indices were a factor of about 3 greater during the September event. Another possible factor may be the difference in the spatial gradient of the electrons set up by the initial injection. The April event also had a much larger Starfish background deep in the inner zone than the September event.

5. What are the overall details of the diffusion process? Are they dependent on geomagnetic activity?

6. Why do some solar events cause inner zone injection, whereas others equally large (in terms of A_p and outer zone flux level increases) do not?

A large volume of spectrometer data is also available in the outer zone. This data will be studied separately. By combining the inner and outer zone data some of the above questions may be answered.

Acknowledgements

The author wishes to thank Professor John R. Winckler for his many informative and helpful discussions during the preparation of this thesis. The contributions of Dr. Sharad Kane and Dr. Roger Arnoldy during the construction and analysis are appreciated.

Special thanks go to Messrs. R. L. Howard and W. Erickson for the electronic design of the spectrometer and to Messrs. R. Thorness and J. Grund for the mechanical design of the spectrometer. The author also wishes to thank Mr. Russell Heinselman for his efficient cataloging and processing of the large volume of data, and Mr. Richard Hendrickson for his help in writing some of the computer programs necessary to process the data.

The author was a National Science Foundation Fellow and a National Aeronautics and Space Administration Trainee during part of his graduate program. The research was supported by the National Aeronautics and Space Administration under contract NAS 5-2071.

References

Alfven, H., Cosmical Electrodynamics, Clarendon Press, Oxford, 1950.

Arnoldy, R. L., R. A. Hoffman and J. R. Winckler, Observations of the Van Allen radiation regions during August and September 1959, Part 1, J. Geophys. Res., 65, 1361-1376, 1960.

Beall, D. S., C. O. Bostrom and D. S. Williams, Structure and decay of the Starfish radiation belt, October 1963 to December 1965, J. Geophys. Res., 72, 3403-3423, 1967.

Brown, W. L., L. J. Cahill, L. R. Davis, C. E. McIlwain and C. S. Roberts, Acceleration of trapped particles during a magnetic storm on April 18, 1965, J. Geophys. Res., 73, 153-162, 1968.

Cladis, J. B., L. F. Chase, W. L. Imhof and D. J. Knecht, Energy spectrum and angular distribution of electrons trapped in the geomagnetic field, J. Geophys. Res., 66, 2297-2312, 1961.

Christofilos, N. C., The Argus experiment, J. Geophys. Res., 64, 869-875, 1959.

Freden, S. C. and R. S. White, Protons in the earth's magnetic field, Phys. Rev. Let., 3, 9-10, 1959.

Gross, W. C., Two-directional focusing of charged particles with a sector-shaped, uniform magnetic field, Rev. Sci. Instr., 22, 717-722, 1951.

Hess, W. N., Collected papers on the artificial radiation belt from July 9, 1962 nuclear detonation, J. Geophys. Res., 68, 605-758, 1963.

Hess, W. N., The earth's radiation belt, Introduction to Space Science, ed. W. N. Hess, Gordon and Breach Science Publishers, New York, 165-204, 1965.

McIlwain, C. E., Coordinates for mapping the distribution of magnetically trapped particles, J. Geophys. Res., 66, 3681-3691, 1961.

O'Brien, B. J., Review of studies of trapped radiation with satellite-borne apparatus, Space Sci. Rev., 1, 415-484, 1962-1963.

O'Brien, B. J., J. A. Van Allen, C. Laughlin and L. A. Frank, Absolute electron intensities in the heart of the earth's outer radiation zone, J. Geophys. Res., 67, 397-407, 1962.

Paulikas, G. A., J. B. Blake and S. C. Freden, Inner-zone electrons in 1964 and 1965, J. Geophys. Res., 72, 2011-2020, 1967.

Pizzella, G., C. E. McIlwain and J. A. Van Allen, Time variations of intensity in the earth's inner radiation zone, October 1959 through December 1960, J. Geophys. Res., 67, 1235-1253, 1962.

Pizzella, G., C. D. Laughlin and B. J. O'Brien, Note on the electron energy spectrum in the inner Van Allen belt, J. Geophys. Res., 67, 3281-3287, 1962.

Van Allen, J. A., 1958, Special joint meeting of National Academy of Sciences and American Physical Society, Washington, D. C., May 1, 1958. Verbatim transcript of lecturers published in IGY Satellite Report No. 13, Jan., 1961, IGY World Data Center A, Rockets and Satellites - National Academy of Sciences, National Research Council, Washington, D. C.

Van Allen, J. A., The geomagnetically trapped corpuscular radiation, J. Geophys. Res., 64, 1683-1689, 1959.

Van Allen, J. A. and L. A. Frank, Radiation measurements to 658,300 km with Pioneer IV, Nature, 184, 219-224, 1959.

Van Allen, J. A., C. E. McIlwain and G. H. Ludwig, Radiation observation with satellite 1958ε , J. Geophys. Res., 64, 271-286, 1959.

Van Allen, J. A., C. E. McIlwain and G. H. Ludwig, Satellite observations of electrons injected into the geomagnetic field, J. Geophys. Res., 64, 877-891, 1959.

Winckler, J. R. and L. Peterson, Large auroral effect on cosmic-ray detectors observed at 8 g/cm^2 atmospheric depth, Phys. Rev., 108, 903-904, 1957.